The interstellar medium revealed by the [CII], CO and HI lines

Inaugural-Dissertation
zur
Erlangung des Doktorgrades
der Mathematisch-Naturwissenschaftlichen Fakultät
der Universität zu Köln

vorgelegt von

Slawa Kabanovic
aus Kirdany (Ukraine)

Köln, 2023

Berichterstatter: Prof. Dr. Jürgen Stutzki
(Gutachter) Prof. Dr. Jan Jolie

Tag der mündlichen Prüfung: 05.06.2023

Diese Arbeit ist meinen Eltern gewidmet,
Zinaida und Mikola Kabanovic

List of Publications

During my doctoral thesis, I participated in a number of publications focusing on studies of the interstellar medium. The following list gives an overview of the peer-reviewed papers, sorted by topic. I will present the publications introducing the SOFIA [C II] mapping projects in which I was involved (Orion A and FEEDBACK) in chapter 3. Chapter 5 gives details about the publications (on the sources RCW 120 and Cygnus X) where my contribution was the most significant. The content and my involvement in the remaining publications will be summarized in chapter 1.

Stellar feedback

Beuther, H., Schneider, N., Simon, R., Suri, S., Ossenkopf-Okada, V., **Kabanovic, S.**, Röllig, M., Guevara, C., Tielens, A. G. G. M., Sandell, G., Buchbender, C., Ricken, O., and Güsten, R. (2022). *FEEDBACK from the NGC 7538 H II region.* A&A, 659, A77.

Bonne, L., Schneider, N., García, P., Bij, A., Broos, P., Fissel, L., Güsten, R., Jackson, J., Simon, R., Townsley, L., Zavagno, A., Aladro, R., Buchbender, C., Guevara, C., Higgins, R., Jacob, A. M., **Kabanovic, S.**, Karim, R., Soam, A., Stutzki, J., Tiwari, M., Wyrowski, F., and Tielens, A. G. G. M. (2022). *The SOFIA FEEDBACK Legacy Survey: Dynamics and Mass Ejection in the Bipolar H II Region RCW 36.* ApJ, 935(2), 171.

Goicoechea, J. R., Pabst, C. H. M., **Kabanovic, S.**, Santa-Maria, M. G., Marcelino, N., Tielens, A. G. G. M., Hacar, A., Berné, O., Buchbender, C., Cuadrado, S., Higgins, R., Kramer, C., Stutzki, J., Suri, S., Teyssier, D., and Wolfire, M. (2020). *Molecular globules in the Veil bubble of Orion. IRAM 30 m ^{12}CO, ^{13}CO, and C^{18}O (2→1) expanded maps of Orion A.* A&A, 639, A1.

Luisi, M., Anderson, L. D., Schneider, N., Simon, R., **Kabanovic, S.**, Güsten, R., Zavagno, A., Broos, P. S., Buchbender, C., Guevara, C., Jacobs, K., Justen, M., Klein, B., Linville, D., Röllig, M., Russeil, D., Stutzki, J., Tiwari, M., Townsley, L. K., and Tielens, A. (2021). *Stellar feedback and triggered star formation in the prototypical bubble RCW 120.* Science Advances, 7(15), eabe9511. See section 5.1.

Pabst, C. H. M., Goicoechea, J. R., Hacar, A., Teyssier, D., Berné, O., Wolfire, M. G., Higgins, R. D., Chambers, E. T., **Kabanovic, S.**, Güsten, R., Stutzki, J., Kramer, C., and Tielens, A. G. G. M. (2022). *[C II] 158 μm line emission from Orion A. II. Photodissociation region physics.* A&A, 658, A98.

Pabst, C. H. M., Goicoechea, J. R., Teyssier, D., Berné, O., Higgins, R. D., Chambers, E. T., **Kabanovic, S.**, Güsten, R., Stutzki, J., and Tielens, A. G. G. M. (2020). *Expanding bubbles in Orion A: [C II] observations of M 42, M 43, and NGC 1977.* A&A, 639, A2.

Pabst, C. H. M., Hacar, A., Goicoechea, J. R., Teyssier, D., Berné, O., Wolfire, M. G., Higgins, R. D., Chambers, E. T., **Kabanovic, S.**, Güsten, R., Stutzki, J., Kramer, C., and Tielens, A. G. G. M. (2021). *[C II] 158 μm line emission from Orion A I. A template for extragalactic studies?* A&A, 651, A111.

Tiwari, M., Karim, R., Pound, M. W., Wolfire, M., Jacob, A., Buchbender, C., Güsten, R., Guevara, C., Higgins, R. D., **Kabanovic, S.**, Pabst, C., Ricken, O., Schneider, N., Simon, R., Stutzki, J., and Tielens, A. G. G. M. (2021). *SOFIA FEEDBACK Survey: Exploring the Dynamics of the Stellar Wind-Driven Shell of RCW 49.* ApJ, 914(2), 117.

Tiwari, M., Wolfire, M., Pound, M. W., Tarantino, E., Karim, R., Bonne, L., Buchbender, C., Güsten, R., Guevara, C., **Kabanovic, S.**, Kavak, Ü., Mertens, M., Schneider, N., Simon, R., Stutzki, J., and Tielens, A. G. G. M. (2022). *SOFIA FEEDBACK Survey: PDR Diagnostics of Stellar Feedback in Different Regions of RCW 49.* AJ, 164(4), 150.

Molecular cloud formation

Bonne, L., Schneider, N., Bontemps, S., Clarke, S. D., Gusdorf, A., Lehmann, A., Steinke, M., Csengeri, T., **Kabanovic, S.**, Simon, R., Buchbender, C., and Güsten, R. (2020). *Dense gas formation in the Musca filament due to the dissipation of a supersonic converging flow.* A&A, 641, A17.

Kabanovic, S., Schneider, N., Ossenkopf-Okada, V., Falasca, F., Güsten, R., Stutzki, J., Simon, R., Buchbender, C., Anderson, L., Bonne, L., Guevara, C., Higgins, R., Koribalski, B., Luisi, M., Mertens, M., Okada, Y., Röllig, M., Seifried, D., Tiwari, M., Wyrowski, F., Zavagno, A., and Tielens, A. G. G. M. (2022). *Self-absorption in [C II], ^{12}CO, and H I in RCW 120. Building up a geometrical and physical model of the region.* A&A, 659, A36. See section 5.2.

Schneider, N., Bonne, L., Bontemps, S., **Kabanovic, S.,**, Simon, R., Ossenkopf-Okada, V., Buchbender, C., Stutzki, J., Mertens, M., Ricken, O., Csengeri, T., and Tielens, A. G. G. M. (2023). *Ionized carbon as a tracer of the assembly of interstellar clouds*. Nature Astronomy in press. doi:10.1038/s41550-023-01901-5. See section 5.3.

Schneider, N., Ossenkopf-Okada, V., Clarke, S., Klessen, R. S., **Kabanovic, S.**, Veltchev, T., Bontemps, S., Dib, S., Csengeri, T., Federrath, C., Di Francesco, J., Motte, F., Andre, P., Arzoumanian, D., Beattie, J. R., Bonne, L., Didelon, P., Elia, D., Koenyves, V., Kritsuk, A., Ladjelate, B., Myers, P., Pezzuto, S., Robitaille, J. F., Roy, A., Seifried, D., Simon, R., Soler, J., and Ward- Thompson, D. (2022). *Understanding star formation in molecular clouds IV. Column density PDFs from quiescent to massive molecular clouds.* A&A, 666, A165.

SOFIA legacy - observations of spectral lines

Higgins, R., **Kabanovic, S.**, Pabst, C., Teyssier, D., Goicoechea, J. R., Berne, O., Chambers, E., Wolfire, M., Suri, S. T., Buchbender, C., Okada, Y., Mertens, M., Parikka, A., Aladro, R., Richter, H., Güsten, R., Stutzki, J., and Tielens, A. G. G. M. (2021). *Observation and calibration strategies for large-scale multi-beam velocity-resolved mapping of the [CII] emission in the Orion molecular cloud.* A&A, 652, A77. See section 3.3.

Schneider, N., Simon, R., Guevara, C., Buchbender, C., Higgins, R. D., Okada, Y., Stutzki, J., Güsten, R., Anderson, L. D., Bally, J., Beuther, H., Bonne, L., Bontemps, S., Chambers, E., Csengeri, T., Graf, U. U., Gusdorf, A., Jacobs, K., Justen, M., **Kabanovic, S.**, Karim, R., Luisi, M., Menten, K., Mertens, M., Mookerjea, B., Ossenkopf-Okada, V., Pabst, C., Pound, M. W., Richter, H., Reyes, N., Ricken, O., Röllig, M., Russeil, D., Sánchez-Monge, Á., Sandell, G., Tiwari, M., Wiesemeyer, H., Wolfire, M., Wyrowski, F., Zavagno, A., and Tielens, A. G. G. M. (2020). *FEEDBACK: a SOFIA Legacy Program to Study Stellar Feedback in Regions of Massive Star Formation.* PASP, 132(1016), 104301. See section 3.4.

Abstract

This thesis is based on observational data of the [C II] 158 μm line as an ideal tracer of molecular cloud formation and stellar feedback effects on the interstellar medium (ISM). Ionizing radiation and winds from massive stars provide stellar feedback, which can either destroy molecular clouds, the birthplaces of stars, or trigger the formation of new stars by expanding H II regions. These processes govern the star formation rate, so it is essential to quantify the various feedback processes for a better understanding of the evolution of the ISM in galaxies. The [C II] line is one of the most important cooling lines of the ISM. It originates in gas at various physical conditions, from low-density, cool, atomic gas to dense and warm photodissociation regions (PDRs). Most importantly, it traces gas kinematics at high spectral resolution, i.e., well below 1 km s^{-1}, which was possible to observe using the GREAT receiver (Guesten et al., 2003), followed by upGREAT (Risacher et al., 2018), on board the Stratospheric Observatory for Infrared Astronomy (SOFIA). [C II] data from the SOFIA C^+ Squad Orion A mapping project and the legacy program FEEDBACK are presented. I focus on results for the RCW 120 H II region and the Cygnus X massive star-forming region.

For analyzing these enormous data sets (several million spectra), various numerical tools were developed and included in an open-source python-based library named "astrokit". Machine learning algorithms such as the Gaussian mixture model were used to disentangle regions of various physical properties in the data cube. I also determined the physical properties of these regions using a two-layer multi-velocity component radiative transfer model, which separates the warm emitting background material from the cold absorbing layer. With a dendrogram-based approach, I disentangled the faint [^{13}C II] emission from the noise. A comparison of the observed [^{12}C II] to [^{13}C II] intensity indicates significant optical depth effects in Orion A and RCW 120. The two-layer multicomponent model showed that a substantial amount of C^+ (column density of 10^{18} cm^{-2}) is located in an external cold absorbing layer. A study of atomic hydrogen (H I) self-absorption (HISA) confirmed an atomic gas origin of the [C II] emission and revealed that RCW 120 is embedded in an extended H I envelope. To derive the physical conditions of the cold, dense molecular cloud associated with RCW 120, I used ^{12}CO and ^{13}CO data observed with the Atacama Pathfinder Experiment (APEX). Both isotopic lines have a high S/N that allowed to use an automated version of the

two-layer model fit on the entire spectral data cube. The derived physical properties of the warm emitting and the cold absorbing layer suggest a column density deficit towards the center of RCW 120. This implies that the parental molecular cloud is flattened along the line of sight, and the expanding H II region is breaking out into the surrounding cold atomic envelope.

Studying the dynamics of the [C II] data in Orion A and the FEEDBACK sources revealed fast, expanding [C II] shells in most of the sources, i.e., the Orion Veil, RCW 120, RCW 49, RCW 36, and NGC 7538. Energy calculations suggest that these shells are wind-driven by O-type or Wolf-Rayet stars and that they are a common feature in H II regions, undetected in previous observations of molecular line emission.

The [C II] line also serves as a tracer for the assembly of molecular clouds. In the Cygnus X region, we were able to show that [C II] reveals CO-dark molecular gas and the highly dynamic interaction between atomic envelopes of molecular clouds that lead to the formation of dense regions where massive stars form. This is the first time that this process, which was predicted by simulations, was observed in the ISM.

Contents

List of Figures

List of Tables

Thesis overview and contributions in publications

During my doctoral thesis, I was part of the SOFIA C^+ Squad (Square Degree) large mapping program of Orion A and the SOFIA Legacy program FEEDBACK. As a member of these two programs, I contributed to many publications whose topics cover the entire cycle of matter in the interstellar medium (ISM). Summarizing, I am first author or contributing author of nine peer-reviewed articles dealing with the aspects of stellar feedback, four articles presenting studies of molecular cloud formation, and two articles focusing on technical aspects of observing atomic and molecular spectral lines. In the following, I will detail my contributions to the published studies, combined with a short introduction to the physical processes governing the ISM cycle, in order to put the results into context.

Orion A is the closest massive star formation region at a distance of $414 \pm 7\,\mathrm{pc}$ (Menten et al., 2007) and, therefore, ideal for studying the effects of stellar feedback. As part of the SOFIA large program C^+ Squad (PI. A. Tielens), Orion A was observed in the fine-structure emission line of ionized carbon at $158\,\mu\mathrm{m}$ [CII] with the German REceiver for Astronomy at Terahertz Frequencies (GREAT, developed and built in a collaboration between the Max-Planck Institute for Radio Astronomy (MPIfR) and the I. Physikalisches Institut at the University of Cologne) on board the Stratospheric Observatory for Infrared Astronomy (SOFIA). The observational procedures and the optimization of the data reduction are described in Higgins et al. (2021). In this publication, I am second author and contributed to the data reduction of the [CII] map. I created a data reduction script based on GILDAS (Grenoble Image and Line Data Analysis Software/Continuum and Line Analysis Single-dish Software). The script uses the spline baseline corrected spectra (the spline method was implemented by R. Higgins) to: 1) convert the intensity scale of the spectra to main beam temperature, 2) resample the spectra to a velocity resolution of $0.3\,\mathrm{km\,s^{-1}}$, 3) subtract a polynomial baseline of order one, 4) detect and then ignore bad spectra in the data set and 5) convolve the spectra onto a grid with the final resolution of $18''$. This data reduction script was written with the objective of handling large data sets, allowing to isolate

each reduction step in order to assess the data quality after each iteration. In addition, I performed an optical depth analysis of the [C II] emission from the Orion-Bar, which is discussed in Sect. 5 in Higgins et al. (2021). The observed square degree map is the largest, high angular resolution (15″) area so far covered in [C II] (2.4 million spectra were taken during the observations resulting in $\sim$ 0.6 million spectra in the gridded spectral cube). The success of this program laid the foundation for other large mapping programs, in particular the SOFIA legacy project FEEDBACK.

In a pioneering work, Pabst et al. (2020) used velocity resolved [C II] spectra to study the kinematics of the three bubbles in Orion A: The Orion Veil (M 42), M 43, and NGC 1977, which gives Orion A its characteristic dragon-like shape. As a co-author of this publication, I contributed to the [C II] optical depth analysis, which was important for the interpretation of the data. We also showed that [C II] is a unique tracer of gas kinematics, revealing, for example, expanding shells in [C II] or high-velocity gas, which are not visible in molecular tracers such as the most abundant species carbon monoxide (CO). The velocity resolved [C II] emission allows quantifying the physical conditions of the expanding bubbles, such as the expansion velocity, its mass, and, subsequently, its kinetic energy. This enables us to determine the possible mechanism that drives the bubble expansion. The two bubbles M 43 and NGC 1977 expand with moderate velocities of $6\,\mathrm{km\,s^{-1}}$ and $1.5\,\mathrm{km\,s^{-1}}$, respectively, which can be explained by the thermal pressure of the ionized gas that also drives the expansion of the H II region. In the case of the Orion Veil, the largest bubble in Orion A located to the south, the H II bubble expands faster, with a velocity of $13\,\mathrm{km\,s^{-1}}$. In addition, we observed that the cavity inside of the compressed cooler shell is filled with hot X-ray emitting plasma, characteristic of stellar wind-blown bubbles. Thus, in contrast to the other two bubbles, M 43 and NGC 1977, the Orion Veil is driven by the stellar wind of the massive O-type star θ^1 Ori C, converting the mechanical energy of the stellar wind efficiently into the kinetic energy of the expanding shell. This remarkable discovery indicated that stellar winds probably mechanically impact the surrounding ISM more than previously thought. However, the dominant part of stellar energy is released through stellar radiation.

In order to better understand the various stellar feedback mechanisms, such as stellar winds, thermal expansion, and radiation pressure, and their impact on the surrounding ISM, the SOFIA legacy program FEEDBACK (Schneider et al., 2020) with PIs A. Tielens and N. Schneider was initiated. FEEDBACK observed 11 high-mass star formation regions that were chosen in order to cover a large parameter space of stellar content, mass, and evolutionary state. One of the best studied sources in FEEDBACK is RCW 120, which is known for its almost perfect spherically symmetric appearance with just a single O-type star located approximately at the center of the nebula. Analyzing the gas kinematics using the velocity resolved [C II] emission, we first detected a fast-expanding stellar wind-driven bubble in RCW 120 (Luisi et al., 2021).

Further observations in other H II regions also revealed expanding [C II] shells, sometimes several in one source, like in RCW 49 (Tiwari et al., 2021) and NGC 7538 (Beuther et al., 2022), and expansion features in the bipolar H II region RCW 36 (Bonne et al., 2022). These findings indicate that stellar wind-driven bubbles from massive O-type or Wolf-Rayet stars might be a common feature, which is so far exclusively traced by [C II] emission since these expanding bubbles were not seen in molecular line emission or atomic hydrogen. In RCW 120, we found that the expanding bubble further compressed the dense cores in the fragmented molecular ring around the H II region, leading to star formation on time scales much shorter than the free-fall time. This new finding was published in a Science Advances paper (Luisi et al., 2021). Moreover, the compression by the stellar winds seems effective even in a porous medium, where most of the stellar radiation would leak out (Beuther et al., 2022) and, therefore, not contribute to a thermally driven expansion. In all studies cited above, I am co-author and contributed to the discussion, analysis, and interpretation of the data. Specifically, I studied optical depth effects in the observed [C II] and CO lines that can potentially mislead the interpretation of spectral profiles. In addition, I derived the physical properties of the expanding bubble in RCW 120, such as column density, mass, and luminosity (Luisi et al., 2021), which is discussed in section 5.1. The main focus during my thesis was on studying the self-absorption effects in RCW 120 (Kabanovic et al., 2022), which will be presented in detail in sections 5.2.1-5.2.4. For that purpose, I solved a set of radiative transfer equations for [C II], CO, and H I and determined the geometry and physical conditions of the parental molecular cloud. We derived that in RCW 120 a substantial amount of C^+ is located in a cold absorbing layer, possibly originating from a cold hydrogen cloud enveloping the molecular cloud.

In all of the observed sources, we do not find a molecular counterpart of the expanding [C II] bubbles, which suggests that the stellar radiation disrupted the parental molecular cloud. However, in the Orion Veil, we detected a few cold CO globules embedded in the expanding shell (Goicoechea et al., 2020). These small, mostly spherical structures are likely remnants from the parental molecular cloud. While the mass of the globules is not large enough for sites of star formation, the position of globule #1 aligns with a known Young Stellar Object (YSO, which is a star in the early stage of its evolution), indicating that this globule was potentially more massive before the stellar feedback disrupted the surrounding molecular cloud. For this study, I contributed analyzing the [C II] data of the cold globules to quantify the carbon fractionation effects which favor the overproduction of ^{13}CO while reducing the [^{13}C II] population, see section 2.4.2.

Apart from the dynamical studies, it is also important to understand the origin of [C II] emission, i.e., its excitation mechanisms and its gas cooling efficiency. In Orion A, the prototypical star formation region, we find that the [C II] line follows a tight correlation with the far-infrared (FIR) emission from the far ultra-violet (FUV, photons

in the energy range between 6 eV to 13.6 eV) heated dust and the PAH (polycyclic aromatic hydrocarbons) emission at 8 μm (Pabst et al., 2021, 2022). The bright [C II] emission originates from the illuminated shells and PDRs. However, with the typical scaling relations used in extragalactic sources to derive the star formation rates from [C II] emission, we underestimate the star formation rate for Orion A. A possible explanation for this discrepancy is that a substantial amount of [C II] emission might arise from low surface brightness PDRs not covered in the observed area since we focused on observing the bright emitting shells. To further quantify the stellar feedback on the molecular structures such as pillars, ridges, and shells emerging from the interaction with the ionizing stars, we performed PDR studies on several regions in RCW 49 (Tiwari et al., 2022). For the PDR studies in Orion A and RCW 49, I was involved in the analysis of the [C II] optical depth effects and the discussion and interpretation of the data.

In addition to studying stellar feedback effects, I also worked on progressing our understanding of the structure and formation of molecular clouds - the birthplaces of stars. It is known that most of the stars form in dense filamentary structures. To understand the formation of those filaments, we studied the Musca filament (Bonne et al., 2020), since it is a well-isolated filament not affected by the stellar feedback of massive stars. While the self-gravity of the parental molecular cloud can enhance the density of a pre-existing clump or filament through mass accretion, it is usually a slow process compared to turbulent motions and flows. In the case of Musca, we showed that it was indeed created from an accretion shock in a colliding flow. As co-author of this work, I solved the two-layer model for the CO emission originating from the filament to disentangle optical depth effects from the kinematics.

The formation of filaments, and in a larger context of molecular clouds in general, by colliding flows of atomic gas (H I) was also the topic of a recent study of the Cygnus X region, published in Nature Astronomy (Schneider et al., 2023). In this largest [C II] map in the FEEDBACK sample, we detected low-surface brightness [C II] emission well outside of the dense molecular clouds that is not seen in molecular line tracers such as CO, but associated with atomic hydrogen. For this study, I performed a similar analysis of H I self-absorption as for RCW 120, and we could show that in Cygnus X, the molecular clouds built up very fast ($\sim 10^6$ Myr) by the interaction between H I envelopes, see section 5.3. In addition, I determined the spatial distribution of the [C II]-bright but CO-dark gas and carefully quantified the noise in the observed spectral cubes. This was essential for the interpretation because the low-surface brightness [C II] emission was just above the 3σ noise level. To further constrain the physical conditions, I derived the FUV-field from the OB-cluster in Cygnus X. Another study to better understand molecular cloud formation and evolution was published by Schneider et al. (2022), in which we investigated the shape of probability distribution functions (PDFs) of the total hydrogen column density of 29 Galactic sources. These maps were generated using

the FIR flux data from Herschel. I contributed in developing a method to produce these high angular resolution maps. We showed that PDFs have very complex shapes, with typically two log-normal distributions at low column density, that we attribute to the H I and H_2 gas phase, respectively, and one or two power-law tails at higher densities that are due to self-gravity.

Modern state-of-the-art receivers such as upGREAT on board SOFIA enable us to perform velocity-resolved large-scale spectral line observations. The observed data cubes contain thousands to millions of single spectra which makes it not feasible to analyze every single spectrum individually. Thus, numerical approaches, including machine learning, are required to utilize the amount of observed data. In the framework of this thesis, I developed the open source python-based software package astrokit[1]. This python library includes a set of tools for data reduction, analysis, and modeling.

[1] https://github.com/skabanovic/astrokit

Introduction

Molecular clouds are the birthplaces of stars that impact their environment through radiation and winds. In particular, far-ultraviolet (FUV) radiation from massive stars strongly ionizes their surrounding gas and dust and heats the interstellar medium (ISM), while stellar winds deliver mechanical energy and mass into the ISM. Massive stars, in addition, explode as supernova at the end of their lifetime and not only enrich the ISM with heavy elements but also stir up the ISM on large scales. All these stellar feedback effects govern the evolution of the ISM and subsequent star formation or the destruction of clouds. A simplified cycle of matter in the ISM is shown schematically in Fig. 2.1, which consists of the main pillars of molecular cloud formation, star formation, and stellar feedback. These three processes are among the major topics in modern astrophysics and are investigated with observations at wavelengths covering the whole electromagnetic spectrum as well as with theoretical studies and simulations. One specific observational tracer is the fine-structure line of ionized carbon [CII] that turned out to be an all-rounder in ISM studies. All three circles in Fig. 2.1 show [CII] emission from RCW 120 and Cygnus X. [CII] is one of the most important cooling lines of the ISM (Tielens and Hollenbach, 1985) and a unique tracer of the gas kinematics (Pabst et al., 2019). Since the atmosphere is mostly opaque at 158 μm, we performed the observations with the Stratospheric Observatory for Infrared Astronomy (SOFIA), a modified Boeing 747SP. SOFIA is shown in the central panel of Fig. 2.1, with the door open showing the 2.7 m diameter telescope (effective diameter 2.5 m). The velocity resolved [CII] observations were performed with the German REceiver for Astronomy at Terahertz Frequencies (GREAT), which is a high-resolution spectrometer (Risacher et al., 2018). GREAT is a PI-instrument developed and built in a collaboration between the University of Cologne and the MPIfR in Bonn. The GREAT-team supported Open Time (OT) flights for the entire astronomical community. The support included the preparation of the observation, performing the observations (on board SOFIA), and the subsequent data reduction. In return, the GREAT-team received Guaranteed Time (GT) observations. GT observations were usually used to perform more sophisticated observations, which required a deep understanding of the instrument and its possible observational modes.

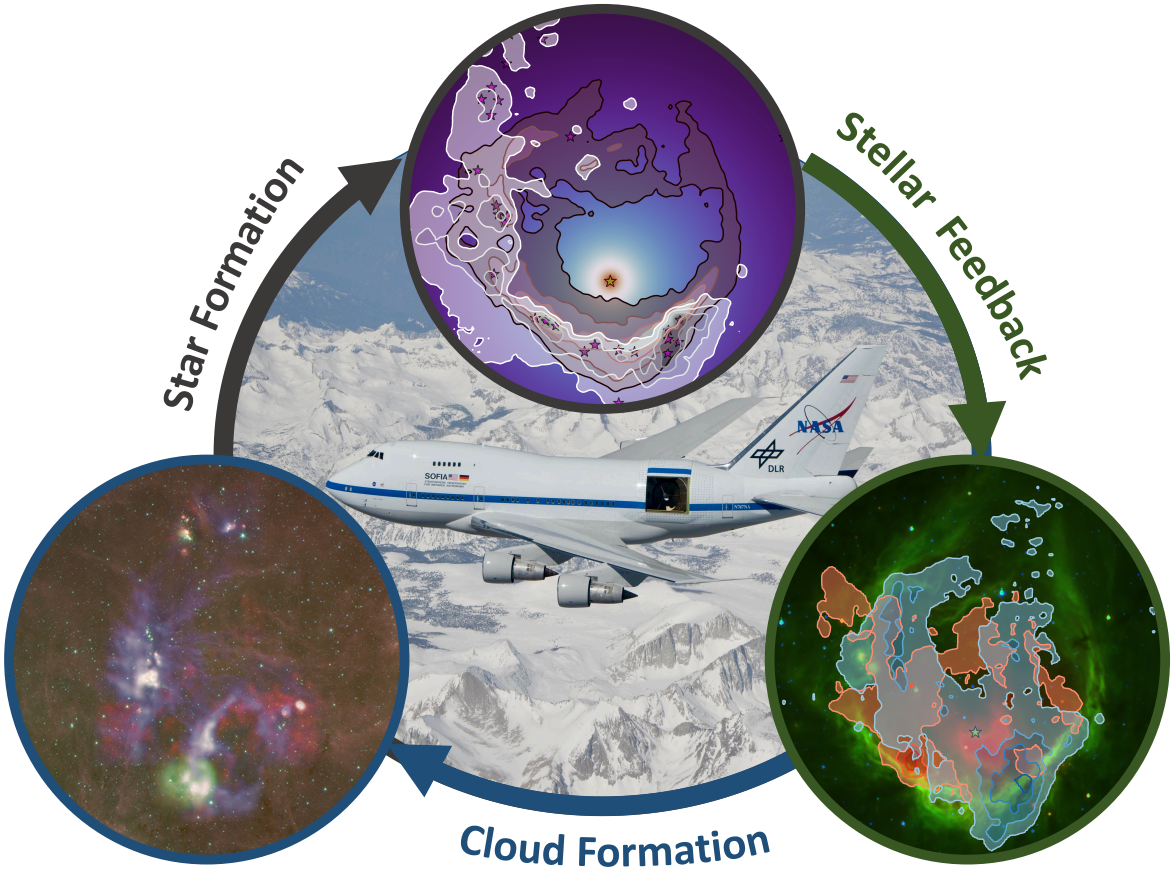

Figure 2.1: Schematic representation of the cycle of matter in the interstellar medium (ISM). Colliding atomic flows, traced by the ionized carbon [CII] line, lead to molecular cloud formation (RGB plot in the lower left panel indicating three velocity components in Cygnus X). Stars form in the densest structures in clouds, such as in RCW 120 shown in CO emission by the light grey colored contours in the top circle of the image. The background displays the FUV-field originating from a massive O-type star (yellow star symbol). Stellar feedback via radiation and winds can drive the dynamics of an HII region and can lead to expanding shells in [CII], like in the RCW 120 region (lower right circle), where the red and blue contours indicate a purely wind-driven bubble. The central image shows SOFIA over the Sierra Nevada mountains (Credit: NASA/Jim Ross). All [CII] observations shown in the image were enabled by the unique observatory.

The formation mechanism of molecular clouds and stars within these clouds is still under debate. A common idea is that the ISM is in a quasi-static equilibrium between gravity, turbulence, and magnetic fields (Krumholz and McKee, 2005). Cloud formation is then a very slow process (taking tens of millions of years), mostly governed by large-scale self-gravitating instabilities caused by spiral density waves (McKee and Ostriker, 2007). Other, more dynamic, scenarios for the formation of dense structures

are cloud-cloud collisions (Haworth et al., 2015; Bisbas et al., 2017; Fukui et al., 2021). In this case, the flows of gas are already molecular before the collision. On the other hand, Dobbs et al. (2020) showed that interactions between atomic hydrogen flows can also create massive structures suitable for subsequent star formation. The different scenarios proposed by simulations need to be investigated observationally, though it is challenging to find the best tracer. One promising way is to use combined observations of atomic hydrogen, HI, carbon monoxide, CO, and ionized carbon, [CII], in order to cover a large parameter space in density and temperature. Since the rotational energy levels of the CO molecular transitions are easily excited already at low densities and temperatures, it is an ideal tracer of molecular clouds. The HI mostly fills the interstellar medium in between the dense molecular clouds. [CII] is an all-rounder that can arise from the bright surfaces of molecular clouds or cold atomic gas flows, as shown in the lower left panel of Fig. 2.1. This three color image displays the [CII] emission for the three major velocity ranges in Cygnus X. DR21 is indicated in blue at [-10, 4] $\mathrm{km\,s^{-1}}$, which is also bright in CO, W75N is shown in green ([4, 12] $\mathrm{km\,s^{-1}}$) and the high-velocity component ([12, 20] $\mathrm{km\,s^{-1}}$) in red, which is [CII]-bright but CO-dark gas (Schneider et al., 2023). It is the first time that cloud interactions between atomic and molecular gas components are seen simultaneously, which makes [CII] an ideal tracer to answer the question of how molecular clouds assemble.

After molecular clouds have formed, it is in the densest filamentary and clumpy structures the stars are formed in. While stars of lower mass most likely arise by fragmentation of filaments (Pineda et al., 2022), massive stars form preferentially in clusters and may compete for the available gas (Bonnell and Bate, 2006). In any case, the strong far ultra-violet (FUV) radiation of OB-type stars ionizes the surrounding medium, creating an HII region, and radiation and winds evacuate the material in the immediate environment. As an example, the FUV radiation of an O-type star in RCW 120 is shown in the top panel of Fig. 2.1. The field strength can be determined from a census of the exciting star(s) if their stellar type, including luminosity and temperature, is known. Because of the supersonic expansion of an HII region into the surrounding medium, a compressed layer of gas and dust accumulates between the ionization and the shock fronts. Most of the time, this appears as ring-like structures. The compressed ring can further fragment, and the dense gas clumps can become gravitationally unstable and form new stars (Elmegreen and Lada, 1977). This scenario is usually referred to as positive stellar feedback. On the other hand, the energetic radiation and strong stellar winds might disrupt pre-existing dense structures and prevent the cloud from further collapse and subsequent star formation (Matzner, 2002; Geen et al., 2016; Kim et al., 2018), which is referred to as negative stellar feedback. Therefore, understanding the role of stellar feedback on the evolution of molecular clouds, galaxies, and, ultimately, the universe is a long-standing problem in contemporary astrophysics.

Most of the energy emitted by a star is contained in its stellar radiation, and only a fraction of it is in the stellar wind. However, Pabst et al. (2019, 2020) showed that the large Orion Veil-Bubble is driven by the stellar wind. The velocity resolved [C II] observation enabled the authors to directly detect the expanding shell and measure an expansion velocity of $\sim 13\,\mathrm{km\,s^{-1}}$. Pabst et al. (2019) concluded that the mechanical energy carried by the stellar wind is converted efficiently into the kinetic energy of the expanding bubble. These findings were made possible through the large spatial coverage of the velocity resolved [C II] data. This unique finding opened up the question about the importance and abundance of stellar wind-driven bubbles and triggered a number of recent studies in theory and simulations (Lancaster et al., 2021a,b; Pittard et al., 2021; Pittard, 2022).

The lower right panel in Fig. 2.1 shows the contours of the two expanding hemispheres (in blue towards the observer and in red away from the observer) of the H II region in RCW 120. The expanding bubble compresses the ISM in its vicinity to a ring-like structure, which is also observed in [C II], see top panel in Fig. 2.1. The [C II] ring is embedded in molecular CO, forming the characteristic layered structures known for photodissociation regions (PDRs). [C II] emission can originate from gas in a variety of physical conditions, such as the H II region or the surrounding PDR. Since the radial velocity component of the expanding shell vanishes with respect to the parental cloud parallel to the plane of the sky, it is not straightforward to disentangle the contribution of the expanding [C II] shell from the bulk emission of the molecular cloud.

Self-absorption effects add an additional difficulty in determining the various contributions to the [C II] line. In a pioneering study, Guevara et al. (2020) performed multiple deep single-point integrations in M43, Horsehead, Monoceros R2, and M17-SW. The authors observed strong optical depth effects in [C II], in contrast to the prediction of common PDR models. So far, the [C II] line was assumed most of the time to be optically thin. However, the numerous [C II] observations performed with SOFIA revealed that the [C II] line is optically thick most of the time. To separate the warm emitting [C II] layer from the cold absorbing gas, Guevara et al. (2020) introduced a two-layer multicomponent model to fit a set of radiative transfer equations to the observed [C II] spectra. The model results indicated that large amounts of ionized carbon are located in a cold absorbing layer. However, the origin of the large column densities of the cold ionized carbon remains unknown.

We usually tend to interpret the observed ring-like features of H II regions as 3D bubbles that are projected onto the plane of the sky, assuming that the parental molecular clouds are extended into all three spatial directions. However, this assumption was challenged by Beaumont and Williams (2010), who presented a survey of 43 H II regions. The authors found a CO deficit toward the interior of the ring-shaped regions suggesting that these observations hint toward flat parental molecular clouds. Thus, the compression of such a "2D" cloud (one dimension is significantly smaller than the

other two) would result in a torus-like structure rather than a bubble. However, CO emission is usually affected by self-absorption effects which might simply mimic such a deficit. Therefore, it is important to separate the warm emitting layer from the cold absorbing molecular material to disentangle self-absorption effects from the geometry of the region.

With this overview in mind, I will first lay the theoretical foundation for this thesis in the following sections. In order to achieve a clear understanding of the physical conditions of the interstellar medium, it is fundamental to understand the interaction of the photons with the material along their path. Thus, we need to first derive the radiative transfer equation as the basis of this work. In section 2.1, I discuss the interaction of particles with the interstellar radiation field.

Section 2.2 introduces the fundamental principles of observational radio astronomy. In the following section 2.3, I discuss how the physical properties of the ISM can be derived from the observed line emission. In section 2.4, the nuclear fusion reactions are discussed that lead to the observed isotope abundance ratios in the ISM. Next, in section 2.5, the photodissociation regions (PDRs) are introduced, focusing on the C^+/C/CO transition. Finally, in the last section 2.6 of the introduction, hydrogen self-absorption is explained.

2.1 Interaction of particles with radiation

To get an insight into the physical processes in the universe, we can make use of a variety of tracers such as cosmic rays, gravitational waves, or photons. The latter allows us to cover the entire electromagnetic spectrum from the cool cosmic microwave background (CMB) to blazers, which are the source of highly energetic gamma-ray photons. The observations of photons are, therefore, ideal to study the various processes found in the interstellar medium (ISM). In the following, I will therefore give an introduction to the interaction of photons with the ISM.

2.1.1 Transition energy and line profile

A molecule or atom X excited to its upper energy level u will return to its lower energy state l emitting a photon with an energy $E_{\rm ph} = h\nu$:

$$X_u \rightarrow X_l + h\nu \ . \tag{2.1}$$

The energy of the photon is equal to the energy difference between the two energy levels of the emitting particle:

$$\Delta E = E_u - E_l \ . \tag{2.2}$$

The above equation (2.2) implies that the resulting transition line, with the transition frequency $\nu_0 = (E_u - E_l)/h$, is defined by an exact energy difference of the two states. However, the finite lifetime of the upper state (Heisenberg uncertainty principle), pressure broadening due to collisions between particles, or Doppler broadening result in a finite width of the observed spectral line. The first two broadening mechanisms can be described by a Lorentzian profile:

$$\phi_L(\nu) = \frac{1}{\pi} \frac{\frac{w_L}{2}}{(\nu - \nu_0)^2 + (\frac{w_L}{2})^2} \ , \tag{2.3}$$

Doppler broadened lines naturally result in a Gaussian profile from the thermal motion of the particle. However, the dominating broadening mechanism in the ISM originates from the turbulent motions in the ISM, which on average also results in a line shape described by a Gaussian profile:

$$\phi_G(\nu) = \frac{2\sqrt{2\ln 2}}{w_G\sqrt{2\pi}} e^{-4\ln 2\left(\frac{\nu-\nu_0}{w_G}\right)^2} \ . \tag{2.4}$$

The factor $2\sqrt{2\ln 2}$ stems from the usage of the full width half maximum (FWHM) w_G instead of the standard deviation σ. The position of the line peak is determined by the transition frequency ν_0.

The emitted photon can be absorbed by an atom or molecule along its path exciting the absorbing particle to its upper energy level u, this is the reverse process shown in equation (2.1). The rate at which photons are absorbed by the ISM is proportional to the number of particles in the lower state n_l and the radiation field $\mathcal{J}_\nu$ weighted by the normalized line profile $\phi(\nu)$ and integrated over all frequencies ν:

$$\bar{\mathcal{J}}_\nu = \int_0^\infty \mathcal{J}_\nu \phi(\nu)\, \mathrm{d}\nu \ . \tag{2.5}$$

Hereby, $\mathcal{J}_\nu$ is defined as the specific intensity I_ν integrated over the source:

$$\mathcal{J}_\nu = \frac{1}{4\pi} \int I_\nu \mathrm{d}\Omega \ , \tag{2.6}$$

and the normalized line profile:

$$\int_0^\infty \phi(\nu)\, \mathrm{d}\nu = 1 \ . \tag{2.7}$$

The normalized line shape describes the relative effectiveness of absorbing or emitting a photon of frequency ν.

2.1.2 Spectral lines

This thesis focuses on the analysis of the [C II] fine structure transition line at 157.74 μm and its isotope [^{13}C II], but I also intensively used CO and H I 21 cm observations.

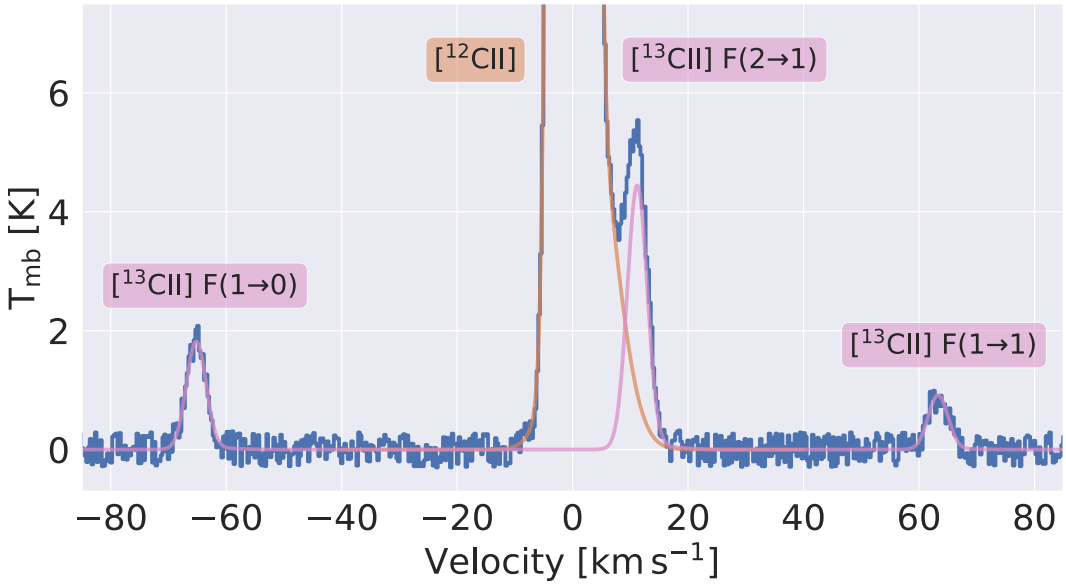

Figure 2.2: Synthetic [C II] spectrum (with randomly generated noise). The orange line indicates the [^{12}C II] fine structure transition line and the pink line shows the [^{13}C II] hyperfine transition lines.

Thus, in the following, I will give a brief overview of all these lines.

The 21 cm hyperfine transition of atomic hydrogen arises due to the energy difference between the parallel and anti-parallel alignment of the proton and electron spin, as shown in Fig. 2.3. The electron spin-flip results in the emission of a photon, though the transition is very unlikely with a mean lifetime of 11 Myr. However, hydrogen is the most abundant element in the universe which allows to observe this transition.

The outermost electron $1s^2 2s^2 2p^1$ of the singly ionized carbon $^{12}C^+$ has two fine-structure energy levels $^2P^o_{1/2}$ - $^2P^o_{3/2}$, see Fig. 2.3. The electron is usually excited through collisions with another free electron, atomic hydrogen, or molecule hydrogen in the ISM. Deexcitation results in the emission of a photon with a wavelength of 157.74 μm (a frequency of 1.9 THz).

For the $^{13}C^+$ isotope, the fine-structure energy levels split into four hyperfine-structure energy levels, resulting in three hyperfine transitions F(2→1), F(1→0), and F(1→1), due to the additional spin of the neutron, see Fig. 2.3. Fig. 2.2 illustrates a synthetic spectrum of the [^{12}C II] fine structure and the [^{13}C II] hyperfine transition lines. The top of the [^{12}C II] line is not shown in the image since its intensity is significantly larger compared to the [^{13}C II] emission lines for an abundance ratio of $\alpha \sim 67$ determined for the solar neighborhood. The strongest [^{13}C II] satellite is located close to the red-shifted wing of the [^{12}C II] line, thus for a typical line width of $\sim 5\,\mathrm{km\,s^{-1}}$, the F(2→1) satellite is often contaminated by the wing emission of the [^{12}C II] line. The contamination, if not too severe, can be corrected by a Gaussian or polynomial fit to the wing emission. Otherwise, only the two outer lines, which are sufficiently far

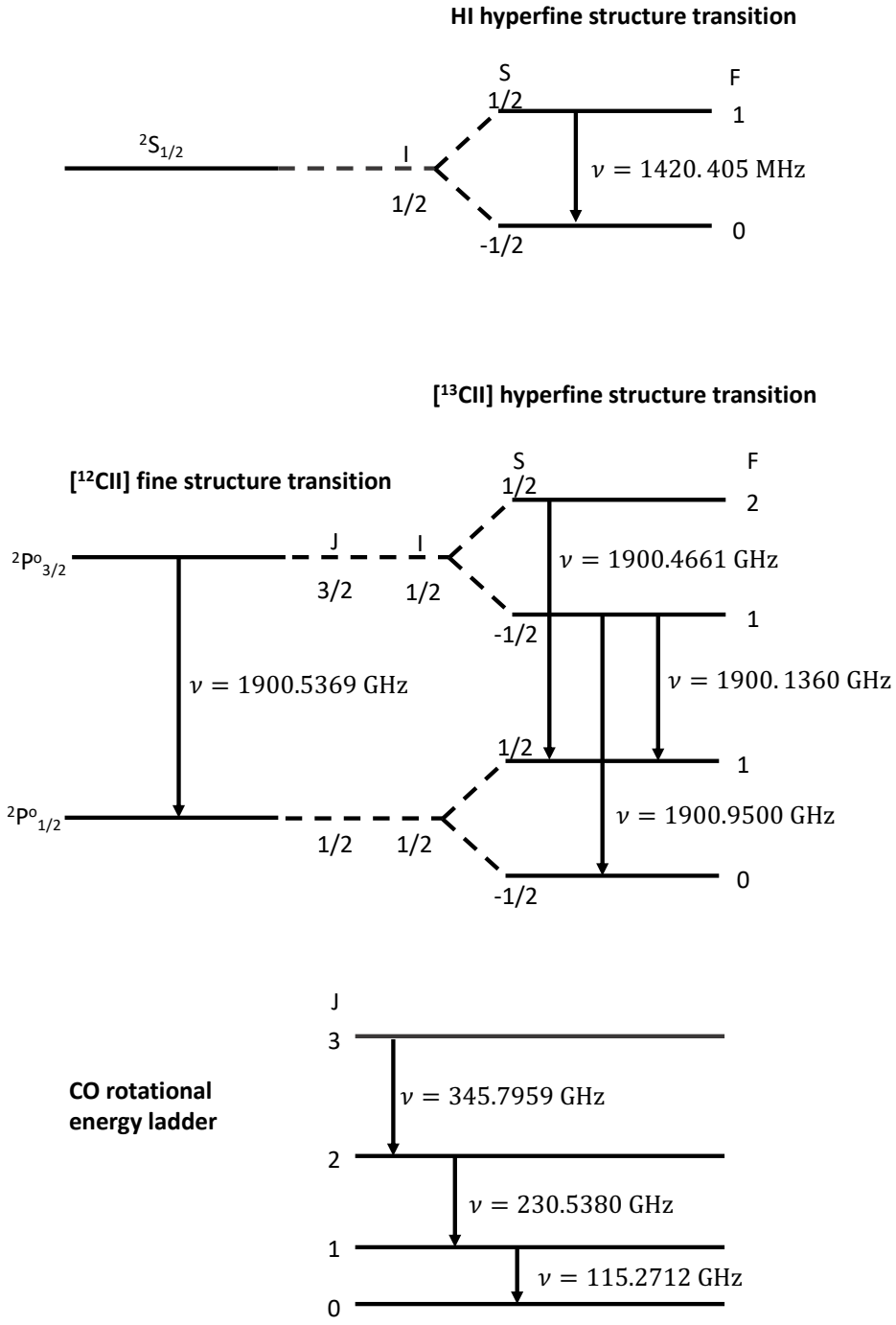

Figure 2.3: HI, [CII], and CO transitions. Top panel: HI hyperfine structure transition energy levels. Middle panel: [^{12}CII] fine structure transition (left) and [^{13}CII] hyperfine transition energy levels (right). Bottom panel: CO rotational energy ladder.

Table 2.1: [^{12}C II] fine structure and [^{13}C II] hyperfine transition parameter (Ossenkopf et al., 2013; Guevara et al., 2020).

Transition line	Weight		Freq.	Velocity offset	Relative intensity
	g_u	g_l	ν [GHz]	$\Delta v_{\mathrm{F}\to\mathrm{F}'}$ [km/s]	$s_{\mathrm{F}\to\mathrm{F}'}$
[^{12}C II] $^2\mathrm{P}_{3/2} \to ^2\mathrm{P}_{1/2}$	4	2	1900.5369	0	1
[^{13}C II] F(2 → 1)	5	3	1900.4661	+ 11.2	0.625
[^{13}C II] F(1 → 0)	3	1	1900.9500	- 65.2	0.250
[^{13}C II] F(1 → 1)	3	3	1900.1360	+ 63.2	0.125

away from the [^{12}C II] line, are accessible. However, each of the outer lines only carries a fraction of the total intensity. The relative line intensities and Doppler shifts of the [^{13}C II] from the [^{12}C II] emission line are stated in Table 2.1.

Carbon monoxide is a diatomic asymmetric molecule and therefore has a permanent electric dipole. In contrast to atoms, molecules have additional rotational and vibrational energy levels. The rotational energy levels can be approximated to (Gordy and Cook, 1984):

$$E_J = hB_0 J(J+1) \ , \tag{2.8}$$

where J is the total angular momentum and $B_0 = h/(8\pi \mathrm{I})$ is the rigid rotor rotation constant with the moment of inertia I. The rotational energy ladder for the low-J transitions, which trace the dense and cold regions in molecular clouds, is shown in Fig. 2.3.

2.1.3 Einstein coefficients

An atom or molecule is in statistical equilibrium if the transition rate which populates a given energy level is balanced by the transition rate which depopulates that energy level. Following Mangum and Shirley (2015), we can express the statistical equilibrium as:

$$n_i \sum_j R_{ij} = \sum_j n_j R_{ij} \ , \tag{2.9}$$

with the transition rates R_{ij} and R_{ji} between energy levels i and j and the particle number density n_i and n_j of each state. Writing the transition rates in terms of Einstein coefficients and the probability of excitation and deexcitation of the energy

levels through collisions, we can now express the above equation (2.9) as follows:

$$n_i \left[\sum_j \left(nC_{ij} + B_{ij}\bar{\mathcal{J}}_\nu \right) + \sum_{j<i} A_{ij} \right] = \sum_j n_j \left(nC_{ji} + B_{ji}\bar{\mathcal{J}}_\nu \right) + \sum_{j>i} nA_{ji} \ . \tag{2.10}$$

In the following, we can derive the Einstein relations for a two-level system without the loss of generality assuming detailed balance. We define i as the lower energy state l and j as the upper energy state u, thus the term $\sum_{u<l} A_{lu} = 0$ vanishes. A constant probability for spontaneous emission excitation is described by the Einstein A coefficient. The A_{ul} coefficient can be best understood by imagining an isolated particle in an excited state u. Following the principle of minimum energy, the particle will eventually transition from its excited energy state into a lower or ground state l by emitting its excess energy in the form of a photon, see eq. (2.1). This process is independent of the surrounding radiation field, thus the emission rate is only defined by the number density of particles in the upper state n_u and A_{ul}, the constant probability for emitting a photon per unit time.

The Einstein B coefficients describe the probability for stimulated radiative excitation and deexcitation. Both B_{lu} and B_{ul} coefficients take the interaction of particles with the surrounding radiation field into account. Thus, the B_{lu} coefficient gives the probability for a particle in a lower state l to get excited to an upper state u by absorbing a photon, this is the reverse process described by eq. (2.1). An already excited particle can be stimulated by an additional photon to go from the upper state u to its lower energy level l:

$$X_u + h\nu \rightarrow X_l + 2h\nu \ . \tag{2.11}$$

The probability for the stimulated emission is determined by the B_{lu} coefficient.

The probability C describes the probability for excitation and deexcitation of the energy levels through collisions. This takes the interaction of particles with each other into account. To derive the relation between the Einstein coefficients, in the following we consider only radiative excitation, thus $C_{lu} = C_{ul} = 0$. This simplifies equation (2.10) to:

$$n_l B_{lu} \bar{\mathcal{J}}_\nu = n_u (A_{ul} + B_{ul} \bar{\mathcal{J}}_\nu \ ) \ . \tag{2.12}$$

We now have three coefficients A_{ul}, B_{ul}, and B_{lu}, which characterize the transition between the lower and upper state. However, we will show subsequently that these quantities are not independent of each other. Thus, we will first derive the relation between each of the coefficients and solve the above equation (2.12) for $\bar{\mathcal{J}}_\nu$:

$$\bar{\mathcal{J}}_\nu = \frac{\frac{A_{ul}}{B_{ul}}}{\frac{n_l}{n_u}\frac{B_{lu}}{B_{ul}} - 1} \ . \tag{2.13}$$

In thermal equilibrium (LTE), the relative population of both states follows the Boltzmann distribution:

$$\begin{aligned}\frac{n_l}{n_u} &= \frac{g_l \mathrm{e}^{-\frac{E_l}{k_\mathrm{B}T}}}{g_u \mathrm{e}^{-\frac{E_u}{k_\mathrm{B}T}}} \\ &= \frac{g_l}{g_u} \mathrm{e}^{\frac{h\nu_0}{kT}} \ ,\end{aligned} \tag{2.14}$$

with the statistical weights g_l and g_u of the transition energy levels. Independent of the LTE case, the above relation, eq (2.14), can be used to define the excitation temperature:

$$T_\mathrm{ex} = \frac{\frac{h\nu}{k_\mathrm{B}}}{\ln\left(\frac{n_l g_u}{n_u g_l}\right)} \ . \tag{2.15}$$

For the [C II] fine structure transition, the weights are $g_l = 2$ and $g_u = 4$. In case of the H I 21 cm hyperfine transition, the statistical weights are $g_l = 1$ and $g_u = 3$. For rotational linear molecules, such as CO, the statistical weights are given by $g = 2J + 1$ with the angular momentum quantum number J. Using equation (2.14), we can write:

$$\bar{\mathcal{J}}_\nu = \frac{\frac{A_{ul}}{B_{ul}}}{\frac{g_l}{g_u}\frac{B_{lu}}{B_{ul}} \mathrm{e}^{\frac{h\nu_0}{k_\mathrm{B}T}} - 1} \ . \tag{2.16}$$

For a medium in thermal equilibrium, the radiation field $\mathcal{J}_\nu$ is determined by the Planck function:

$$B_\nu(T) = \frac{2h\nu^3}{c^2} \frac{1}{\mathrm{e}^{h\nu/k_\mathrm{B}T} - 1} \ . \tag{2.17}$$

The Planck function is visualized for various temperatures, such as the CMB $T = 2.7\,\mathrm{K}$, the cold neutral interstellar medium CNM $T = 80\,\mathrm{K}$, our Sun $T = 5778\,\mathrm{K}$, and an O-type star $T = 37500\,\mathrm{K}$ in Fig. 2.5. Leveraging the fact that B_ν varies little on the scale of the line width $\Delta\nu$, we can set $\bar{\mathcal{J}}_\nu = B_\nu$. Comparing both expressions in equation (2.16) and (2.17) results in the Einstein relations:

$$g_l B_{lu} = g_u B_{ul} \ , \tag{2.18}$$

$$A_{ul} = \frac{2h\nu^3}{c^2} B_{ul} \ . \tag{2.19}$$

These two Einstein relations connect the three Einstein coefficients with each other. Thus, it is sufficient to determine only one of the coefficients to get all three. The Einstein relations are an example of what is known as detailed balance relation connecting a microscopic process to its inverse process, here emission and absorption. We note that the energy density u_ν is often used instead of $\mathcal{J}_\nu$ to define the Einstein B-coefficients. This leads to a difference between the definitions by a factor of $c/(4\pi)$.

2.1.4 Radiative transfer

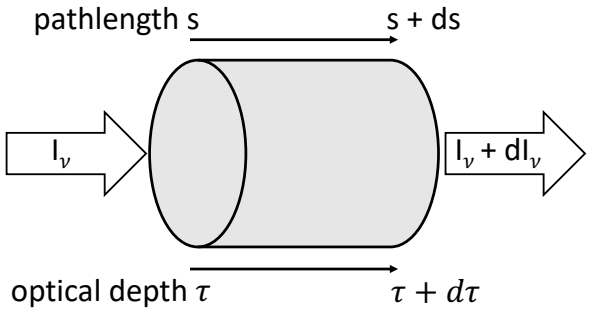

Figure 2.4: Sketch of the radiative transfer properties.

The frequency dependent intensity I_ν of a beam of light propagating through interstellar material will be affected by absorption and emission of photons along the path s, see Fig. 2.4. The changes in intensity $\mathrm{d}I_\nu$ are described by the equation of radiative transfer:

$$\mathrm{d}I_\nu = -I_\nu \kappa_\nu \mathrm{d}s + \epsilon_\nu \mathrm{d}s \ , \tag{2.20}$$

with the "absorption coefficient" κ_ν and the "emissivity" ϵ_ν at the frequency ν. Both quantities can be expressed in terms of Einstein coefficients and the number density of particles in the corresponding state (Mangum and Shirley, 2015):

$$\begin{aligned} \kappa_\nu &= \frac{h\nu}{4\pi} \left(n_l B_{lu} - n_u B_{ul}\right) \phi_\nu \\ &= \frac{c^2}{8\pi\nu^2} \frac{g_u}{g_l} n_l A_{ul} \left(1 - \frac{g_l n_u}{g_u n_l}\right) \phi_\nu \ , \end{aligned} \tag{2.21}$$

and

$$\epsilon_\nu = \frac{h\nu}{4\pi} A_{ul} n_u \ . \tag{2.22}$$

The first term $-I_\nu \kappa_\nu \mathrm{d}s$ on the right-hand side of equation (2.20) describes the change in I_ν due to absorption and stimulated emission, while the second term $\epsilon_\nu \mathrm{d}s$ of the equation takes spontaneous emission into account.

We can simplify the radiative transfer equation (2.20) by introducing the optical depth τ_ν:

$$\mathrm{d}\tau_\nu = \kappa_\nu \mathrm{d}s \ . \tag{2.23}$$

In the framework of radiative transfer, the optical depth is a more useful quantity than the path length s. The medium is called opaque or optically thick for the observed

emission if the integral of $\mathrm{d}\tau_\nu$ along the path is $\tau_\nu > 1$ close to the transition frequency ν_0 of the observed line. Accordingly, the medium is called optically thin or transparent for the observed line if $\tau_\nu < 1$ at every frequency.

We can now rewrite equation (2.20) for the radiation transfer to:

$$\mathrm{d}I_\nu = -I_\nu \mathrm{d}\tau_\nu + S_\nu \mathrm{d}\tau_\nu \ , \tag{2.24}$$

with the "source function":

$$S_\nu = \frac{j_\nu}{\kappa_\nu} = \frac{2h\nu^3}{c^2}\left(\frac{g_u n_l}{g_l n_u} - 1\right)^{-1} \ . \tag{2.25}$$

To formulate the radiative transfer equation (2.24) in its integral form, we first multiply both sides of the equation with e^{τ_ν} and rearrange the equation, such that we get:

$$\begin{aligned} \mathrm{e}^{\tau_\nu}(\mathrm{d}I_\nu + I_\nu \mathrm{d}\tau_\nu) &= \mathrm{e}^{\tau_\nu} S_\nu \mathrm{d}\tau_\nu \\ \mathrm{d}\left(\mathrm{e}^{\tau_\nu} I_\nu\right) &= \mathrm{e}^{\tau_\nu} S_\nu \mathrm{d}\tau_\nu \ . \end{aligned} \tag{2.26}$$

We can now integrate both sides of the above equation:

$$\mathrm{e}^{\tau_\nu} I_\nu - I_{\nu,0} = \int_0^{\tau_\nu} \mathrm{e}^{\tau'} S_\nu \, \mathrm{d}\tau' \ , \tag{2.27}$$

with the initial intensity $I_{\nu,0} = I_\nu(\tau_\nu = 0)$. Rewriting and multiplying the equation with $\mathrm{e}^{-\tau_\nu}$ results in the radiative transfer equation in the integral form:

$$I_\nu(\tau_\nu) = I_{\nu,0}\mathrm{e}^{-\tau_\nu} + \int_0^{\tau_\nu} \mathrm{e}^{-(\tau_\nu - \tau')} S_\nu \, \mathrm{d}\tau' \ . \tag{2.28}$$

Equation (2.28) is the formal solution of the radiative transfer equation (2.20). The intensity $I_\nu(\tau_\nu)$ given by the above solution can be read as the initial intensity $I_{\nu,0}$ attenuated by the material along the path by a factor of $\mathrm{e}^{-\tau_\nu}$ plus the emission from the cloud $S_\nu \, \mathrm{d}\tau$ attenuated by $\mathrm{e}^{-(\tau_\nu - \tau')}$ due to material along the column between the observer and the point of emission.

For a medium in local thermal equilibrium (LTE) the energy level population corresponds to a single excitation temperature T_ex. In this case, we express the source function S_ν by the Planck function $B_\nu(T_\mathrm{ex})$. This assumption allows us to integrate equation (2.28) analytically, which leads to:

$$I_\nu = I_{\nu,0}\mathrm{e}^{-\tau_\nu} + B_\nu(T_\mathrm{ex})\left(1 - \mathrm{e}^{-\tau_\nu}\right) \ . \tag{2.29}$$

The above equation (2.29) can be interpreted considering the two extreme cases. In the limit of $\tau \to 0$, the equation simplifies to $I_\nu = I_{\nu,0}$, thus the radiation originating from the background and moving through an optically thin medium does not change

its initial intensity. In the optically thick limit, $\tau \to \infty$, the equation simplifies to $I_\nu = B_\nu(T_{\rm ex})$, which tells us that the radiation gets absorbed by the ISM and we only detect the emission from the surface of the interstellar cloud.

In spectral line measurements, we are usually only interested in the emission coming from the observed source itself, therefore we subtract the background continuum intensity $I_{\nu,0}$ (the $\tau \to 0$ limit) from the observed intensity I_ν:

$$\begin{aligned}\Delta I_\nu &= I_\nu - I_{\nu,0} \\ &= I_{\nu,0}\mathrm{e}^{-\tau_\nu} + B_\nu(T_{\rm ex})\left(1-\mathrm{e}^{-\tau_\nu}\right) - I_{\nu,0} \\ &= \left(B_\nu(T_{\rm ex}) - B_\nu(T_{\rm bg})\right)\left(1-\mathrm{e}^{-\tau_\nu}\right) \ . \end{aligned} \tag{2.30}$$

The lower limit for the background temperature $T_{\rm bg} = 2.7\,\mathrm{K}$ is determined by the cosmic microwave background radiation.

2.1.5 Brightness temperature

For short wavelengths, we can show that the brightness follows a linear relation, see Fig. 2.5. For $h\nu \ll k_{\rm B}T$, the exponential term in the Planck function can be approximated by:

$$\mathrm{e}^{\frac{h\nu}{k_{\rm B}T}} \approx 1 + \frac{h\nu}{k_{\rm B}T} + \frac{1}{2}\left(\frac{h\nu}{k_{\rm B}T}\right)^2 \ , \tag{2.31}$$

which leads to:

$$\begin{aligned} B_\nu(T) &\approx \frac{2h\nu^3}{c^2}\frac{1}{\left(1+\frac{h\nu}{k_{\rm B}T}+\frac{1}{2}\left(\frac{h\nu}{k_{\rm B}T}\right)^2\right)-1} \\ &= \frac{2\nu^2 k_{\rm B}T}{c^2}\frac{1}{1+\frac{1}{2}\frac{h\nu}{k_{\rm B}T}} \\ &\approx \frac{2\nu^2 k_{\rm B}T}{c^2}\left(1-\frac{1}{2}\frac{h\nu}{k_{\rm B}T}\right) \\ &= \frac{2\nu^2 k_{\rm B}}{c^2}\left(T-\frac{h\nu}{2k_{\rm B}}\right) \ . \end{aligned} \tag{2.32}$$

Only the first term of equation (2.32) is temperature-dependent, which results in a linear relation between brightness and temperature:

$$B_\nu(T) \approx \frac{2\nu^2}{c^2}k_{\rm B}T \ . \tag{2.33}$$

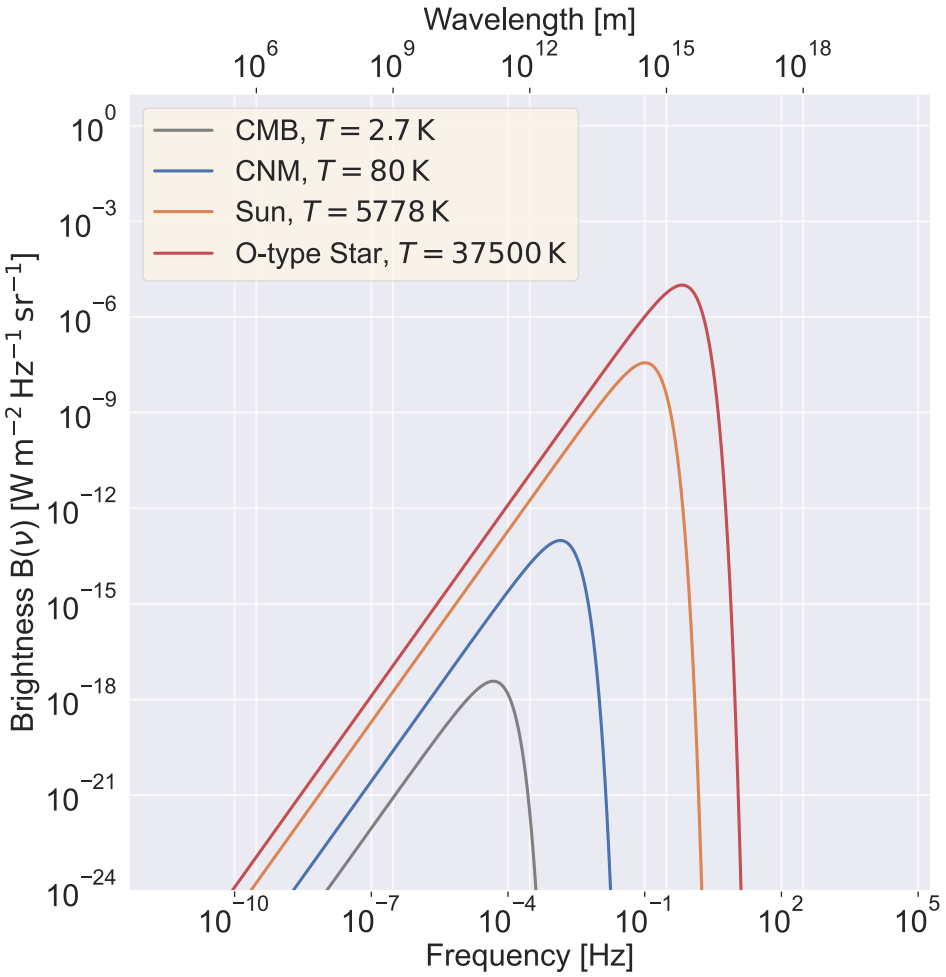

Figure 2.5: Planck's radiation law. The black body radiation spectrum of the cosmic microwave background (CMB, $T = 2.7\,\mathrm{K}$) in gray, the cold neutral interstellar medium (CNM, $T = 80\,\mathrm{K}$) in blue, the Sun ($T = 5778\,\mathrm{K}$) in orange, and an O-type star ($T = 37500\,\mathrm{K}$) as one can find in RCW 120 in red.

This approximation is known as the "Rayleigh-Jeans law". With this approximation, we can define the equivalent brightness temperature of a black body emission at a temperature T_{ex}:

$$\mathcal{J}_\nu(T_{\mathrm{ex}}) = \frac{c^2}{2\nu^2 k_{\mathrm{B}}} B_\nu(T_{\mathrm{ex}}) = \frac{T_0}{e^{\frac{T_0}{T_{\mathrm{ex}}}} - 1}\,, \tag{2.34}$$

with the equivalent temperature of the transition $T_0 = h\nu/k_{\mathrm{B}}$. The above relation is in general valid for frequencies:

$$\frac{\nu}{\mathrm{GHz}} \ll 20.84 \left(\frac{T}{\mathrm{K}}\right)\,. \tag{2.35}$$

We can now use equations (2.33) and (2.34) to express the observed intensity in

terms of brightness temperature:

$$T_\mathrm{b} = \frac{c^2}{2k_\mathrm{B}\nu^2}\Delta I_\nu \ . \tag{2.36}$$

The above relation allows us to determine the corresponding temperature T_b for an observed intensity, which is always valid. However, the relation is especially useful in the Rayleigh-Jeans limit since in this case, the derived temperature is equal to the excitation temperature of the observed transition line.

2.2 Observational radio astronomy

2.2.1 Antenna temperature and efficiencies

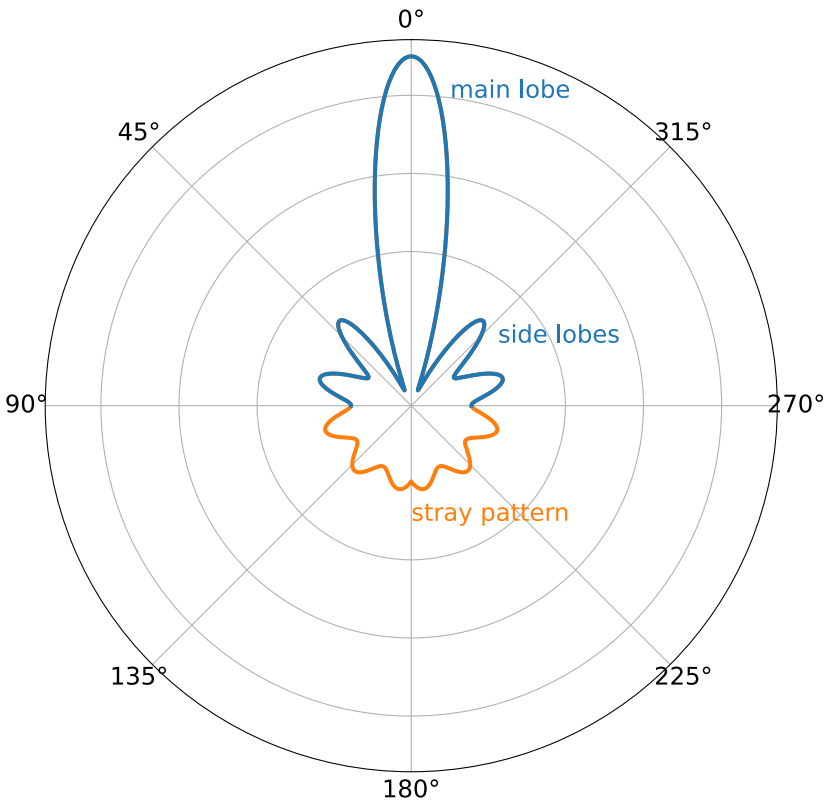

Figure 2.6: Schematic antenna pattern in polar coordinates. The blue part indicates the sensitivity of the forward half including the main beam and the side lobes. The orange part shows the sensitivity of the rear side including the stray pattern.

In the previous sect. 2.1.5, we derived a simple linear relation (2.36) between the intensity originating from an astronomical source and the corresponding brightness temperature T_b. However, the fundamental nature of any observation makes it impossible for us to detect a photon without interacting with it. Thus, the observed intensity

is convolved with the antenna pattern $P(\theta, \phi)$ of the telescope. If the telescope is not located in space, the observed signal is additionally affected by atmospheric attenuation. The relation between the brightness temperature of the emitting source and the observed antenna temperature is (Kutner and Ulich, 1981):

$$T_{\mathrm{A}} = T_{\mathrm{b}} \left(\frac{\iint_{\Omega_s} P_n(\theta - \theta', \phi - \phi') \psi(\theta', \phi') \, \mathrm{d}\Omega'}{\iint_{4\pi} P_n(\theta, \phi) \, \mathrm{d}\Omega} \right) e^{-\tau_a A} \, , \tag{2.37}$$

with the normalized antenna pattern $P_n(\theta, \phi)$:

$$P_n(\theta, \phi) = \frac{P(\theta, \phi)}{P_{\max}} \, , \tag{2.38}$$

the normalized source brightness distribution $\psi(\theta, \phi)$ (which is defined between zero and one), the solid angle Ω_s subtended by the source, the optical depth of the atmosphere τ_a, and the airmass $A \sim 1/\sin(\varepsilon)$, which is a function of elevation ε.

Equation (2.37) implies that in order to determine the brightness temperature of the emitting source from the observed antenna temperature, we need detailed knowledge of the source structure and the antenna pattern. Therefore, it is more convenient to rewrite the equation in terms of parameters that can be accessed by direct measurements. To do so, we first divide the telescope pattern, which is shown schematically in Fig. 2.6, into two regimes: (i) The forward part of the antenna pattern, which includes the main beam and side lobes of the antenna, (ii) the rear side which contains the stray pattern.

If we define the solid angle Ω_{mb} such that it covers the main lobe of the diffraction pattern, then we can determine the coupling efficiency η_c, which describes the coupling of the antenna to the source (covering the solid angle Ω_s):

$$\eta_c = \frac{\iint_{\Omega_s} P_n(\theta - \theta', \phi - \phi') \psi(\theta', \phi') \, \mathrm{d}\Omega'}{\iint_{\Omega_{\mathrm{mb}}} P_n(\theta, \phi) \, \mathrm{d}\Omega} \, . \tag{2.39}$$

If the source is smaller than the main beam, we need to take into account that the source is unresolved and the observed intensity is smaller, therefore only a part of the observed radiation is originating from the source itself. With this in mind, we can define the corrected source intensity, known as the main beam temperature:

$$T_{\mathrm{mb}} = \eta_c T_{\mathrm{b}} \, . \tag{2.40}$$

Without the knowledge of the source structure, T_{mb} is as close as one can get to the "true" brightness temperature of the emitting source. We can now write the relation between the source-corrected intensity and the antenna temperature corrected for atmospheric attenuation:

$$T'_{\mathrm{A}} = T_{\mathrm{A}} e^{\tau_a A} \, , \tag{2.41}$$

by combining equations (2.37), (2.39), and (2.40):

$$T'_{\mathrm{A}} = T_{\mathrm{mb}} \left(\frac{\iint_{\Omega_{\mathrm{mb}}} P_n(\theta,\phi)\,\mathrm{d}\Omega}{\iint_{4\pi} P_n(\theta,\phi)\,\mathrm{d}\Omega} \right) . \tag{2.42}$$

The term inside the brackets can be expressed as the main beam efficiency:

$$\eta_{\mathrm{mb}} = \frac{\iint_{\Omega_{\mathrm{mb}}} P_n(\theta,\phi)\,\mathrm{d}\Omega}{\iint_{4\pi} P_n(\theta,\phi)\,\mathrm{d}\Omega} , \tag{2.43}$$

which determines the fraction of power detected in the main lobe compared to the total power detected. Thus, the relation between the main beam temperature and the antenna temperature as shown in equation (2.42) can now be written in its compact form:

$$T_{\mathrm{mb}} = \frac{T'_{\mathrm{A}}}{\eta_{\mathrm{mb}}} . \tag{2.44}$$

In the mm/sub-mm range, a common calibration procedure is the chopper wheel method (Wilson et al., 2009) which gives access to the forward beam brightness temperature:

$$T^*_{\mathrm{A}} = \frac{T'_{\mathrm{A}}}{\eta_{\mathrm{f}}} , \tag{2.45}$$

with the forward efficiency:

$$\eta_f = \frac{\iint_{2\pi} P_n(\theta,\phi)\,\mathrm{d}\Omega}{\iint_{4\pi} P_n(\theta,\phi)\,\mathrm{d}\Omega} , \tag{2.46}$$

which determines the power fraction in the forward-facing half sphere in comparison to the total power detected. The forward beam brightness temperature T^*_{A} is commonly referred to as the corrected antenna temperature and can be related to the main beam temperature by:

$$T^*_{\mathrm{A}} \eta_{\mathrm{f}} = T_{\mathrm{mb}} \eta_{\mathrm{mb}} . \tag{2.47}$$

We can subsequently rewrite the radiative transfer equation (2.30) in terms of main beam temperature, which is commonly used in radio astronomy:

$$T_{\mathrm{mb}} = \eta_c \left(\mathcal{J}_\nu(T_{\mathrm{ex}}) - \mathcal{J}_\nu(T_{\mathrm{bg}}) \right) \left(1 - \mathrm{e}^{-\tau_\nu} \right) . \tag{2.48}$$

In addition, we have included here the coupling efficiency η_c (eq. 2.39), which is also often called the filling factor f in the literature. The filling factor has values between 0 and 1 and gives the fraction of the area filled by the emitting source with respect to the main beam of the telescope. However, extended sources much larger than the beam size, such as molecular clouds, can still have a filling factor below one due to

their clumpy nature. Note, if observing an extended source and a significant fraction of the power is located in the side lobes, see Fig. 2.6, this can lead to an unwanted pickup in the measurements.

2.2.2 Receiver calibration and radiometer equation

The noise temperature σ_{rms} of our measured signal is given by the radiometer equation (Dicke, 1946), which follows from Gaussian statistics (a rigorous derivation can be done from quantum field theory):

Radiometer equation

$$\sigma_{\mathrm{rms}} = \frac{T_{\mathrm{sys}}}{\sqrt{t_{\mathrm{int}}\Delta\nu}} \ , \tag{2.49}$$

with the integration time t_{int} and the receiver bandwidth $\Delta\nu$. The system temperature is the sum of the receiver noise temperature T_{rec} and the antenna temperature of the sky $T_{\mathrm{A,sky}}$:

$$T_{\mathrm{sys}} = T_{\mathrm{A,sky}} + T_{\mathrm{rec}} \ . \tag{2.50}$$

The receiver output is given as system power P_{sys}. The system temperature is connected to the measured system power via the gain factor g:

$$P_{\mathrm{sys}} = gT_{\mathrm{sys}} = P_{\mathrm{A}} + P_{\mathrm{rec}} = g(T_{\mathrm{A,sky}} + T_{\mathrm{rec}}) \ , \tag{2.51}$$

Therefore the system power is the sum of the power received from the atmospheric emission P_{A} and the power from the receiver noise P_{rec}. To determine the two unknown parameters, the receiver temperature and gain factor, we need to measure the system power of two radiation sources with different known temperatures:

$$\begin{aligned} P_{\mathrm{hot}} &= g(T_{\mathrm{hot}} + T_{\mathrm{rec}}) \ , \\ P_{\mathrm{cold}} &= g(T_{\mathrm{cold}} + T_{\mathrm{rec}}) \ . \end{aligned} \tag{2.52}$$

This measurement method is known as “Hot-Cold-Load”. To stay in the dynamic range of the receiver, we use the ambient temperature T_{amb} for the “Hot-Load”. Thus, T_{hot} can be simply measured by putting an absorber in the radiation path to the detector. For T_{cold}, we can use a source that is substantially colder than the ambient temperature, such as liquid nitrogen. We can now write the gain factor g as a function of measured power and temperature:

$$g = \frac{P_{\mathrm{hot}} - P_{\mathrm{cold}}}{T_{\mathrm{hot}} - T_{\mathrm{cold}}} \ , \tag{2.53}$$

and the receiver temperature can be expressed as:

$$T_{\mathrm{rec}} = \frac{T_{\mathrm{hot}} - Y T_{\mathrm{cold}}}{Y - 1} \ , \tag{2.54}$$

with the Y-factor, which is the ratio between the two measured power values:

$$Y = \frac{P_{\mathrm{hot}}}{P_{\mathrm{cold}}} \ . \tag{2.55}$$

We note that the antenna temperature of the sky is a function of the atmospheric temperature. Reducing the atmospheric contribution by placing the observatory at a high altitude can substantially reduce the noise of the measurement. The radiometer equation (2.49) states that the noise is proportional to the integration time by $\sim 1/\sqrt{t_{\mathrm{int}}}$ for a given bandwidth $\Delta\nu$. Thus, doubling the integration time reduces the noise by $1/\sqrt{2}$.

2.3 Physical properties of the interstellar medium

2.3.1 Column densities

A useful physical quantity is the column number density N, given by the integral of the number of particles n per unit length s along the line-of-sight (LOS):

$$N = \int n \, \mathrm{d}s \ . \tag{2.56}$$

Since neither the path length nor the number density is directly observable, we rather make use of the optical depth and the attenuation coefficient. These are determined by intrinsic properties of the particles, such as the Einstein coefficients, and the energy level population of the interstellar particles, which is confined by the temperature of the gas:

$$\begin{aligned}
\tau_\nu &= \int \kappa_\nu \, \mathrm{d}s \\
&= \frac{c^2}{8\pi\nu^2} \frac{g_u}{g_l} \phi_\nu A_{ul} \int n_l \left(1 - \frac{g_l n_u}{g_u n_l}\right) \mathrm{d}s \\
&= \frac{c^2}{8\pi\nu^2} \frac{g_u}{g_l} \phi_\nu A_{ul} N_l \left(1 - \frac{g_l N_u}{g_u N_l}\right) \\
&= \frac{c^2}{8\pi\nu^2} \left(\mathrm{e}^{\frac{T_0}{T_{\mathrm{ex}}}} - 1\right) A_{ul} \phi_\nu N_u \ .
\end{aligned} \tag{2.57}$$

This equation relates the optical depth to the the total number of particles along the line of sight either in the lower or upper state. Assuming LTE conditions, we can relate

the column density of the particles in state i to the total column density N for a given excitation temperature:

$$\frac{N}{N_i} = \frac{Q}{g_i} \mathrm{e}^{\frac{E_i}{k_\mathrm{B} T_\mathrm{ex}}} \ . \tag{2.58}$$

The partition function Q can be determined by demanding that the sum over the column density N_i of all possible states i is the total column number density:

$$N = \sum_i N_i \ . \tag{2.59}$$

Combining equation (2.58) and (2.59), we can write the partition function as:

$$Q = \sum_i g_i \mathrm{e}^{-\frac{E_i}{k_\mathrm{B} T_\mathrm{ex}}} \ . \tag{2.60}$$

The energy levels of the ionized carbon line and hydrogen line can be expressed as a two-level system. The corresponding partition function reads:

$$Q_{\uparrow\downarrow} = g_l \mathrm{e}^{-\frac{E_l}{k_\mathrm{B} T_\mathrm{ex}}} + g_u \mathrm{e}^{-\frac{E_u}{k_\mathrm{B} T_\mathrm{ex}}} \ . \tag{2.61}$$

Inserting equations (2.61) and (2.58) into (2.57), we find the temperature-dependent conversion factor between the optical depth and the column number density for a two-level atomic system:

$$\tau_{\nu,\uparrow\downarrow} = N_{\uparrow\downarrow} \frac{c^2}{8\pi\nu^2} \frac{g_u}{g_l} A_{ul} \phi_\nu \frac{1 - \mathrm{e}^{-\frac{T_0}{T_\mathrm{ex}}}}{1 + \frac{g_u}{g_l} \mathrm{e}^{-\frac{T_0}{T_\mathrm{ex}}}} \ . \tag{2.62}$$

In order to eliminate the line profile in eq. (2.62), we need to integrate both sides. While we could simply stay in frequency space, it is more convenient to work in velocity space. The transformation is given by the Doppler shift $\mathrm{d}\nu = (\nu/c)\,\mathrm{d}v$, which results in the following expression for the column number density:

Column density - two level system transition

$$N_{\uparrow\downarrow} = \frac{8\pi\nu^3}{c^3} \frac{g_l}{g_u} \frac{1}{A_{ul}} \frac{1 + \frac{g_u}{g_l} \mathrm{e}^{-\frac{T_0}{T_\mathrm{ex}}}}{1 - \mathrm{e}^{-\frac{T_0}{T_\mathrm{ex}}}} \int \tau_{\uparrow\downarrow}(v)\,\mathrm{d}v \ . \tag{2.63}$$

We note that the integral over the normalized line shape is simply one. In the optically thin case, the radiative transfer equation (2.48) becomes:

$$T_\mathrm{mb} = f\left(\mathcal{J}_\nu(T_\mathrm{ex}) - \mathcal{J}_\nu(T_\mathrm{bg})\right)\tau \ . \tag{2.64}$$

This allows us to write eq. (2.63) in the more convenient form:

$$N_{\uparrow\downarrow} = \frac{8\pi\nu^3}{c^3}\frac{g_l}{g_u}\frac{1}{A_{ul}}\frac{1+\frac{g_u}{g_l}\mathrm{e}^{-\frac{T_0}{T_{\mathrm{ex}}}}}{1-\mathrm{e}^{-\frac{T_0}{T_{\mathrm{ex}}}}}\frac{\int T_{\mathrm{mb}}\,\mathrm{d}v}{f\left(\mathcal{J}_\nu(T_{\mathrm{ex}})-\mathcal{J}_\nu(T_{\mathrm{bg}})\right)}\ . \tag{2.65}$$

Under the assumption of an optically thin line and for a given T_{ex}, we obtain the column density of the integrated spectral line. This is a very useful equation that allows determining the column number density directly from the measured temperature. However, the derived column density needs to be interpreted as a lower limit, since any correction for the neglected optical depth will increase the value.

We now have derived an expression for the atomic two-level transition lines. In the following, I will repeat the exercise for the rotational transitions of the CO molecule. Similar to the previous derivation, we can start with equation (2.57) and subsequently need to find the conversion factor from the column density of the excited state population N_u to the total column density of the rotational transitions N_{rot}. The molecular partition function can be approximated for diatomic linear molecules to (Mangum and Shirley, 2015):

$$Q_{\mathrm{rot}} = \sum_{J=0}^{\infty}(2J+1)\,\mathrm{e}^{-\frac{E_J}{k_{\mathrm{B}}T}} \approx \frac{k_{\mathrm{B}}T}{hB_0}+\frac{1}{3}\ . \tag{2.66}$$

This gives us the relation between the optical depth and the total molecular column density:

$$\tau_{\nu,\mathrm{rot}} = N_{\mathrm{rot}}g_u A_{ul}\frac{c^2}{8\pi\nu^2}\frac{\mathrm{e}^{-\frac{E_u}{k_{\mathrm{B}}T_{\mathrm{ex}}}}}{\left(\frac{k_{\mathrm{B}}T_{\mathrm{ex}}}{hB_0}+\frac{1}{3}\right)}\left(\mathrm{e}^{\frac{T_0}{T_{\mathrm{ex}}}-1}\right)\phi_\nu\ . \tag{2.67}$$

For a dipole transition, the Einstein coefficient A_{ul} for spontaneous emission can be written as a function of the electric dipole moment μ_{lu} (Wilson et al., 2009):

$$A_{ul} = \frac{64\pi^4\nu^3}{3hc^3}|\mu_{ul}|^2\ , \tag{2.68}$$

with the dipole matrix element $|\mu_{ul}|^2$ (Mangum and Shirley, 2015):

$$|\mu_{ul}|^2 = \mu^2 S = \frac{J_u}{2J_u+1}\ , \tag{2.69}$$

The line strength $S = J/(2J+1)$ is valid for linear molecular transitions $J \rightarrow J-1$. The rotation degeneracy g_u for rotational molecular transitions is the product of the rotational degeneracy, g_J and g_K, and the spin degeneracy g_s. However, for linear molecules, the K degeneracy g_K and the spin degeneracy g_S are equal to one. Thus only the rotational degeneracy g_J remains, which can be expressed as:

$$g_J = 2J_u+1\ . \tag{2.70}$$

This leads us to the following expression of the molecular optical depth:

$$\tau_{\nu,\mathrm{rot}} = N_{\mathrm{rot}} \frac{8\pi^3 J_u \mu^2 \nu}{3hc} \frac{\mathrm{e}^{-\frac{T_u}{T_{\mathrm{ex}}}}}{\left(\frac{k_{\mathrm{B}} T_{\mathrm{ex}}}{hB_0} + \frac{1}{3}\right)} \left(\mathrm{e}^{\frac{T_0}{T_{\mathrm{ex}}}} - 1\right) \phi_\nu \ , \tag{2.71}$$

with the equivalent temperature of the upper energy state $T_u = E_u/k_{\mathrm{B}}$. Rearranging the above equation to N_{rot}, transforming from frequency space to velocity space, and integrating on both sides yield the following expression (Mangum and Shirley, 2015):

Column density - rotational molecular transition

$$N_{\mathrm{rot}} = \frac{3h}{8\pi^3 \mu^2 J_u} \left(\frac{k_{\mathrm{B}} T}{hB_0} + \frac{1}{3}\right) \mathrm{e}^{\frac{T_u}{T_{\mathrm{ex}}}} \left(\mathrm{e}^{\frac{T_0}{T_{\mathrm{ex}}}} - 1\right) \int \tau_{\mathrm{rot}}(v)\, \mathrm{d}v \ . \tag{2.72}$$

In the optically thin case, the equation simplifies to:

$$N_{\mathrm{rot}} = \frac{3h}{8\pi^3 \mu^2 J_u} \left(\frac{k_{\mathrm{B}} T}{hB_0} + \frac{1}{3}\right) \mathrm{e}^{\frac{T_u}{T_{\mathrm{ex}}}} \left(\mathrm{e}^{\frac{T_0}{T_{\mathrm{ex}}}} - 1\right) \frac{\int T_{\mathrm{mb}}\, \mathrm{d}v}{f\left(\mathcal{J}_\nu(T_{\mathrm{ex}}) - \mathcal{J}_\nu(T_{\mathrm{bg}})\right)} \ . \tag{2.73}$$

With the above equations, we are now well-equipped to determine the column density of the atomic and molecular ISM. Combining this information with the observed angular size of the source and its distance to the observer, we can derive the mass of the observed atomic or molecular cloud.

2.3.2 Optical depth

In the previous section, we derived the optical depth as a function of excitation temperature and column number density. These parameters are, in general, not easily accessible. However, under the assumption of a homogeneous medium, we can determine the optical depth from the intensity ratio between two isotopes (Ossenkopf et al., 2013):

Optical depth

$$\begin{aligned} \frac{T_{\mathrm{mb},^{12}\mathrm{C}}(v)}{T_{\mathrm{mb},^{13}\mathrm{C}}(v)} &= \frac{\mathcal{J}_{^{12}\mathrm{C}}(T_{\mathrm{ex}})}{\mathcal{J}_{^{13}\mathrm{C}}(T_{\mathrm{ex}})} \left(\frac{1 - e^{-\tau(v)}}{1 - e^{-\frac{\tau(v)}{\alpha}}}\right) \\ &\approx \frac{1 - e^{-\tau(v)}}{1 - \left(1 - \frac{\tau(v)}{\alpha}\right)} \\ &= \frac{1 - e^{-\tau(v)}}{\tau(v)} \alpha \ . \end{aligned} \tag{2.74}$$

With the corresponding error (Kabanovic et al., 2022):

$$\Delta\tau = \left|\frac{\tau^2}{(1+\tau)e^{-\tau}-1}\right| \sqrt{\frac{\alpha^2 T_{^{13}\mathrm{C}}^2 \sigma_{\mathrm{rms},^{12}\mathrm{C}}^2 + \alpha^2 T_{^{12}\mathrm{C}}^2 \sigma_{\mathrm{rms},^{13}\mathrm{C}}^2 + \Delta\alpha^2 T_{^{13}\mathrm{C}}^2 T_{^{12}\mathrm{C}}^2}{\alpha^4 T_{^{13}\mathrm{C}}^4}} \,. \tag{2.75}$$

Knowing the local carbon abundance ratio $\alpha = {}^{12}\mathrm{C}/{}^{13}\mathrm{C}$, we can derive with eq. (2.74) the velocity resolved optical depth for C^+ and CO if both isotopes are observed. To take into account that the [^{13}C II] emission splits into three lines, as shown in Fig. 2.2, we can average the lines weighted by their relative line intensity (Guevara et al., 2020):

$$T_{[^{13}\mathrm{C\,II}]}(v) = \frac{\sum_{\mathrm{F}\to\mathrm{F}'} \left(\frac{s_{\mathrm{F}\to\mathrm{F}'}}{\sigma_{\mathrm{rms}}}\right)^2 \frac{T_{[^{13}\mathrm{C\,II}]_{\mathrm{F}\to\mathrm{F}'}}(v-\Delta v_{\mathrm{F}\to\mathrm{F}'})}{s_{\mathrm{F}\to\mathrm{F}'}}}{\sum_{\mathrm{F}\to\mathrm{F}'} \left(\frac{s_{\mathrm{F}\to\mathrm{F}'}}{\sigma_{\mathrm{rms}}}\right)^2} \,. \tag{2.76}$$

The rms of the scaled and averaged hyperfine lines can be determined by:

$$\sigma_{\mathrm{rms},[^{13}\mathrm{C\,II}]} = \frac{\sigma_{\mathrm{rms}}}{\sqrt{\sum_{\mathrm{F}\to\mathrm{F}'} s_{\mathrm{F}\to\mathrm{F}'}^2}} \sim 1.46\,\sigma_{\mathrm{rms}} \,. \tag{2.77}$$

It might seem counter-intuitive that the averaged rms is increasing. However, the increase of the rms is a result of the scaling by the relative line intensity of each satellite.

2.4 Isotope ratios

As discussed in the previous section 2.3.2, the intensity ratio between two carbon isotopes gives access to the optical depth (eq. (2.74) assuming that both isotopes have the same excitation temperature, since both have the same collision partners) of the observed atom or molecule when compared to the local isotope abundance ratio α. In this section, I give an introduction into the nuclear fusion reaction leading to the observed isotope abundance ratio in the ISM.

In the framework of the standard big bang model, the production of some light elements such as hydrogen, deuterium, helium, and lithium can be explained (Boesgaard and Steigman, 1985). Heavier elements are produced in the sequential nuclear burning, which takes place in the hot central cores of stars. This burning sequence follows the order: H, He, C, Ne, O, and Si and stops with the formation of iron in the stellar core. Heavier elements can be formed during a supernova explosion of massive stars.

The primary carbon isotope ^{12}C is produced in the triple-alpha process:

$$\begin{aligned} {}^4_2\mathrm{He} + {}^4_2\mathrm{He} &\to {}^8_4\mathrm{Be} \,, \\ {}^8_4\mathrm{Be} + {}^4_2\mathrm{He} &\to {}^{12}_6\mathrm{C} + 2\gamma \,. \end{aligned} \tag{2.78}$$

The interaction of the produced carbon with an alpha particle will lead to the formation of oxygen:

$$^{12}_{6}\mathrm{C} + ^{4}_{2}\mathrm{He} \rightarrow ^{16}_{8}\mathrm{O} + \gamma \ . \tag{2.79}$$

These primary elements are synthesized directly from H or He in stellar cores in the first generation of stars. Secondary products of nucleosynthesis, on the other hand, need heavier elements that can only be produced in the later generations of stars. These secondary elements lag behind the primary product during the evolution of the universe. However, they are expected to increase in abundance with increasing time.

Moreover, the abundance of an element is not only determined by whether it is a primary or secondary product, but its formation and propagation back into the interstellar medium are constrained by the stellar type and its evolution (Wilson and Matteucci, 1992; Wilson, 1999). For this work, the carbon abundance ratio is relevant. ^{12}C is produced and ejected into the ISM by stellar winds of low- to intermediate-mass stars (mass $1 - 8\,\mathrm{M}_{\odot}$) or the ejection from planetary nebulae. Massive stars can eject carbon through supernovae explosions, Wolf-Rayet stars by their extreme stellar winds. On the other hand, ^{16}O is only ejected back into the ISM by massive stars with a mass $> 8M_{\odot}$ through SN explosions.

The secondary carbon isotope ^{13}C is produced through the CNO (carbon, nitrogen, oxygen) burning cycle in stellar envelopes. The ^{13}C isotope is formed by an incomplete proton burning of the primary isotope ^{12}C inside the envelopes of red-giant stars (Wilson, 1999):

$$\begin{aligned} ^{12}\mathrm{C} + \mathrm{H} &\rightarrow ^{13}\mathrm{N} + \gamma \ , \\ ^{13}\mathrm{N} &\rightarrow ^{13}\mathrm{C} + \mathrm{e}^{+} \ . \end{aligned} \tag{2.80}$$

A subsequent reaction of ^{13}C with a proton would produce ^{14}N, however, this reaction is not completed. Instead, ^{13}C is mixed by convection in the outer parts of the stellar envelope and ejected into the ISM by stellar winds.

2.4.1 Spatial distribution of the carbon isotope ratio in the Milky Way

Since secondary products, such as ^{13}C, are produced from their primary isotope ^{12}C, we can expect the $^{12}\mathrm{C}/^{13}\mathrm{C}$ ratio to decrease with time or in regions with an enhanced stellar density. In our galaxy, the Milky Way, we have the highest concentration of stars toward the galactic center, the galactic plane in general, and in the spiral arms. Star counts decrease outwards of the galactic plane. Accordingly, we would expect a carbon ratio gradient as a function of distance from the galactic center, increasing from the center outwards to the edge of the galaxy.

The carbon ratio along the galaxy was determined using CN, CO, and H_2CO observations. Milam et al. (2005) applied a linear least-square fit to the combination of all measurements. The linear function resulting from the fit that describes the carbon isotopic ratio as a function of galactocentric distance $D_{\rm GC}$ is (Milam et al., 2005):

Galactic carbon isotope ratio

$$^{12}\mathrm{C}/^{13}\mathrm{C} = 6.21(\pm1.0)D_{\rm GC} + 18.71(\pm7.37)\ . \tag{2.81}$$

We usually have access to the heliocentric distance $D_{\rm HC}$, for example, through trigonometric parallax measurements. The conversion to the galactocentric distance is given by:

$$D_{\rm GC} = \sqrt{(D'_{\rm HC}\cos(l) - R_{\rm GC})^2 + D'^2_{\rm HC}\sin^2(l)}\ , \tag{2.82}$$

with the distance to the galactic center $R_{\rm GC} = 8178 \pm 13_{stat.} \pm 22_{\rm sys}$ (Gravity Collaboration et al., 2019), the heliocentric distance projected onto the galactic plane $D'_{\rm HC} = D_{\rm HC}\cos(b)$ and the galactic longitude l and latitude b. If not otherwise stated, we use the above equation (2.81) to derive the local abundance ratio in this work.

2.4.2 Carbon fractionation

While on galactic scales, the carbon isotopic ratio follows a linear gradient (eq. 2.81), the isotopic ratio can locally be affected by fractionation effects. The most important carbon fractionation reaction is (Ossenkopf et al., 2013):

$$^{13}\mathrm{C}^+ + {}^{12}\mathrm{CO} \rightleftharpoons {}^{12}\mathrm{C}^+ + {}^{13}\mathrm{CO} + \Delta E\ . \tag{2.83}$$

At high temperatures, significantly above $\Delta E = 35\,\mathrm{K}$ (Woods and Willacy, 2009), the above reaction eq. (2.83) is equally probable in both directions. However, at low temperatures, the forward reaction becomes favorable. Thus, $^{13}C^+$ is bound into its molecular form ^{13}CO, while additional C^+ is produced. This reaction increases the abundance ratio for the ionized carbon α^+ compared to the elemental carbon ratio α, thus $\alpha^+ > \alpha$.

The enrichment of $^{12}C^+$ at low temperatures is counteracted by the self-shielding of the carbon molecule ^{12}CO against the photo-dissociating radiation. Because of the lower column density of the ^{13}CO, it requires a larger cloud depth to become optically thick. This results in a larger fraction of ^{12}C bound in the molecular form, which decreases the ionized abundance ratio compared to the elemental abundance ratio, thus $\alpha^+ < \alpha$.

To quantify the two competing processes against each other Röllig and Ossenkopf (2013) performed model simulations of photodissociation regions using the KOSMA-τ

model. The authors predicted that the ionized carbon abundance ratio is found to be higher or equal to the elemental abundance ratio. The fractionation ratio is equal to the elemental ratio at low visual extinctions A_v, but increases with increasing A_v. The visual extinction can be related to the hydrogen column density by $N_{\mathrm{H}} = 1.9 \cdot 10^{21}\,\mathrm{cm}^{-2} A_v$ (Bohlin et al., 1978).

2.5 Photodissociation regions

Photodissociation regions (PDRs) are a direct result of the interaction of stellar FUV radiation with the surrounding atomic and molecular gas. They are found around OB-type stars, emitting a sufficient amount of energetic photons between 6 and 13.6 eV, such that the chemistry of the cloud is dominated by the FUV radiation (Tielens and Hollenbach, 1985). PDRs are therefore often referred to as photon-dominated regions (Sternberg and Dalgarno, 1995).

Higher energy photons above 13.6 eV will ionize the surrounding hydrogen, creating an H II region around the star embedded in the ISM. The PDR is located between the hot, $T \sim 10^4\,\mathrm{K}$, ionized region and the molecular phase. It is characterized by its layered structure in contrast to the sharp transition of an H II region, as shown schematically in Fig. 2.7. Absorption of all photons at energies $\geqslant 13.6\,\mathrm{eV}$ leaves all atoms with ionization potentials higher than that of hydrogen, such as oxygen or nitrogen, in a neutral state. However, these hot ionized H II regions have low visual extinctions of $A_v < 0.1$.

The hydrogen gas near the surface of the PDR region will be heated to $100 - 1000\,\mathrm{K}$ through photoelectric heating (P.E). Electrons ejected from grains and PAHs (Tielens and Hollenbach, 1985) carry the excess energy from the ionization process into the surrounding medium. The heating is mainly balanced by cooling through fine-structure line emission of [C II] 158 μm, [O I] 63 μm, and the high-J rotational transitions of the CO molecule, thus the C^+/C/CO transition is fundamentally important to determine the energy balance and the line intensities of PDRs. Ionized carbon C^+ is mainly formed by photoionization of carbon:

$$\mathrm{C} + h\nu \rightarrow \mathrm{C}^+ + \mathrm{e}^- \ , \tag{2.84}$$

forming the outer ionized layer. At the edge of the cloud, neutral carbon is mainly produced by radiative recombination

$$\mathrm{C}^+ + \mathrm{e}^- \rightarrow \mathrm{C} + h\nu \ . \tag{2.85}$$

Further into the cloud, the FUV intensity decreases and therefore also the photodissociation of molecules forming a molecular layer. At $A_v \sim 0.1 - 0.8$ (see Schneider et al. (2022) and references therein) we find the H I to H_2 transition region. Deeper into the

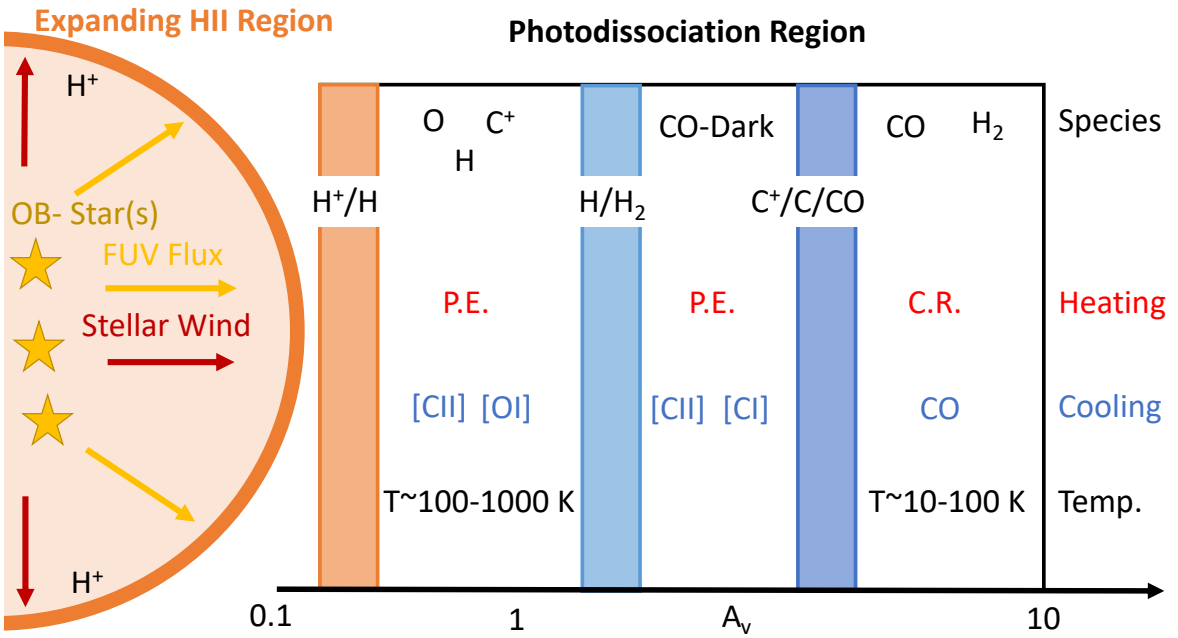

Figure 2.7: Schematic illustration of the layered characteristics of a PDR. The main heating mechanisms are indicated in red. At the surface of the PDR, photoelectric heating (P.E.) is dominant, while deeper into the cloud, cosmic-ray ionization (C.R.) takes over. The main cooling lines for each PDR layer are shown in blue. Note that the exact A_v values depend on the ratio of the radiation field and density, G_0/n, thus a lower G_0/n, or a simply lower UV field moves the hydrogen and carbon transitions to lower A_v. The image is adapted from Wolfire et al. (2022).

cloud at $A_v \sim 2-4$, neutral carbon, C, and CO are formed by a series of ion-neutral reactions. Note that the exact A_v values depend on the ratio of radiation field and density, G_0/n, thus a lower G_0/n, or a simply lower UV field, moves the hydrogen and carbon transitions to lower A_v (Wolfire et al., 2022). The region where hydrogen is already in the molecular form, but CO is not yet readily detectable, is known as CO-dark molecular gas (Grenier et al., 2005; Wolfire et al., 2010). Even deeper into the cloud, the temperatures drop down to $T \sim 10\,\mathrm{K}$. The gas is mainly heated by cosmic-ray ionization (CR) while the cooling is dominated by the low-J rotational transitions of the CO molecules.

2.6 HISA

In section 2.3.2, we discussed how to calculate the optical depth from the measured line intensity difference between two isotopes. In the case of hydrogen, it is difficult to access the deuterium isotope due to its weak emission and contamination by the

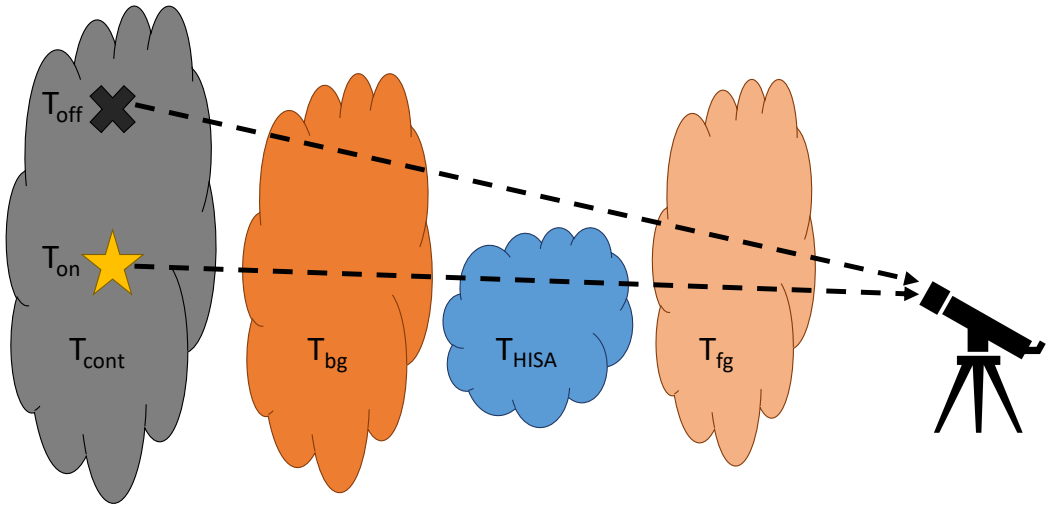

Figure 2.8: Schematic representation of the HISA analysis. The grey cloud indicates the origin of the continuum emission $T_{\rm cont}$. The dark orange cloud indicates the source emission $T_{\rm bg}$. The blue cloud indicates the cold absorbing hydrogen cloud with the temperature $T_{\rm HISA}$. The light orange cloud indicates a possible emitting foreground cloud located between the observed source and the observer. $T_{\rm on}$ indicates the intensity observed along the line of sight towards the source. $T_{\rm off}$ shows the intensity measured along the line of sight toward the off-position with no absorption. The image is adapted from Wang et al. (2020).

widespread hydrogen emission. However, we can make use of the abundance and homogeneity of the hydrogen emission to determine the optical depth of cold-absorbing hydrogen. To quantify the hydrogen self-absorption (HISA), we determine the intensity difference between hydrogen emission affected by self-absorption $T_{\rm on}$ to a position free of absorption effects $T_{\rm off}$, see Fig. 2.8. Similar to Guevara et al. (2020), we use a multi-layer approach following Wang et al. (2020). The observed intensity toward the source $T_{\rm on}$ consists of the source emission $T_{\rm bg}$, the absorption by cold hydrogen $T_{\rm HISA}$, and additional emission by a possible warm emitting foreground cloud, see Fig. 2.8. Subtracting the continuum emission from the observed spectrum, we can write the resulting intensity as:

$$\begin{aligned} T_{\rm on}(v) = & \, T_{\rm fg}\left(1 - e^{-\tau_{\rm fg}(v)}\right) \\ & + T_{\rm HISA}\left(1 - e^{\tau_{\rm HISA}(v)}\right) e^{-\tau_{\rm fg}(v)} \\ & + T_{\rm bg}\left(1 - e^{-\tau_{\rm bg}(v)}\right) e^{-[\tau_{\rm fg}(v)+\tau_{\rm HISA}(v)]} \\ & - T_{\rm cont}\left(e^{-[\tau_{\rm fg}(v)+\tau_{\rm HISA}(v)+\tau_{\rm bg}(v)]} - 1\right) \ . \end{aligned} \tag{2.86}$$

The "off"-position can be determined by moving spatially away from the "on"-position until the absorption dip, visible in the spectrum, disappear. Thus, the off-spectrum is free of HISA.

$$\begin{aligned} T_{\rm off}(v) = & \, T_{\rm fg}\left(1 - e^{-\tau_{\rm fg}(v)}\right) \\ & + T_{\rm bg}\left(1 - e^{-\tau_{\rm bg}(v)}\right) e^{-\tau_{\rm fg}(v)} \\ & - T_{\rm cont}\left(e^{-[\tau_{\rm fg}(v)+\tau_{\rm bg}(v)]} - 1\right) \ . \end{aligned} \tag{2.87}$$

The observed difference between the on- and the off-spectrum $T_{\rm on-off} = T_{\rm on} - T_{\rm off}$ can be expressed as (Wang et al., 2020):

$$T_{\rm on-off}(v) = \left(T_{\rm HISA} - T_{\rm bg}\left(1 - e^{-\tau_{\rm bg}(v)}\right) - T_{\rm cont} e^{-\tau_{\rm bg}(v)}\right)\left(1 - e^{-\tau_{\rm HISA}(v)}\right) e^{-\tau_{\rm fg}(v)} \ , \tag{2.88}$$

with the temperature of the cold absorbing hydrogen cloud $T_{\rm HISA}$, the continuum emission $T_{\rm cont}$, and the intensity from the off position $T_{\rm off}$, which is free of absorption. Assuming that the background and foreground components are optically thin, $\tau_{\rm fg}, \tau_{\rm bg} \ll 1$, we can simplify the above equation (2.88) to:

$$T_{\rm on-off}(v) = \left(T_{\rm HISA} - pT_{\rm off}(v) - T_{\rm cont}\right) \cdot \left(1 - e^{-\tau_{\rm HISA}(v)}\right) \ . \tag{2.89}$$

The dimensionless parameter p is defined as:

$$p(v) = \frac{T_{\rm bg}\left(1 - e^{-\tau_{\rm bg}(v)}\right)}{T_{\rm off}(v)} \ , \tag{2.90}$$

thus, p can take a value between 0 and 1. For $p = 1$, there is no foreground emission and for $p = 0$, there is no background emission from the observed source. If not otherwise stated, we assume no foreground cloud, thus $p = 1$ reduces the equation to a two-layer model. This gives an expression for the HISA optical depth (Kabanovic et al., 2022):

HISA optical depth

$$\tau_{\rm HISA}(v) = -\ln\left(1 - \frac{T_{\rm on-off}(v)}{T_{\rm HISA} - T_{\rm off}(v) - T_{\rm cont}}\right) \ . \tag{2.91}$$

The HISA temperature is the only parameter in eq. (2.91), which is not directly measured. However, we can utilize the absorption dip intensity $T_{\rm on,min}$ to derive an upper limit for the HISA temperature:

$$T_{\rm HISA,max} = T_{\rm on,min} + T_{\rm cont} \ . \tag{2.92}$$

Simulations of molecular clouds performed by Seifried et al. (2022) showed that the amount of cold-absorbing hydrogen is underestimated due to the assumption of a

single temperature. Thus, using the upper limit for equation (2.91) leads to results closest to the actual hydrogen column density.

Knowing the velocity resolved optical depth and temperature of the cold hydrogen cloud, we can derive the hydrogen column number density. Taking into account that for any possible excitation temperature $T_{\rm ex} \gg T_0$, we can simplify equation (2.63) to:

$$\begin{aligned} N_{\rm H} &= \frac{8\pi\nu^3}{c^3}\frac{1}{A_{ul}}\frac{T_{\rm ex}}{T_0}\left(\frac{g_l}{g_u}+1\right)\int \tau(v)\,dv \\ &= 1.823\cdot 10^{18}\,[\mathrm{cm}^{-2}]\frac{T_{\rm ex}}{[\mathrm{K}]}\int \frac{\tau(v)\,dv}{[\mathrm{km\,s}^{-1}]}\ . \end{aligned} \tag{2.93}$$

Knowing in addition the distance to the hydrogen cloud, we can determine its mass:

$$M_{\rm H} = m_{\rm H} N_{\rm H} A_{\rm obs}\ , \tag{2.94}$$

with the hydrogen mass $m_{\rm H}$ and $A_{\rm obs}$ the observed angular area scaled by the squared heliocentric distance.

SOFIA legacy

As part of the GREAT-team (PIs J. Stutzki and R. Güsten) I had the unique opportunity to participate in more than 50 flights with the Stratospheric Observatory for Infrared Astronomy (SOFIA). I was responsible for setting up the computer systems and performing the observations. These consisted of service observing for projects accepted from the astronomical community, my own PI projects from accepted SOFIA proposals, and observations for two large programs: the large scale [CII] mapping of Orion A (C^+ Squad) and the FEEDBACK SOFIA legacy program, of which I am a member. In the following section 3.1, I will briefly introduce SOFIA, followed by an overview of the GREAT-instrument in section 3.2. In section 3.3, I will introduce the Orion A C^+ Squad, the first large-scale mapping project with the GREAT-instrument. These pioneering observations covered a square-degree map of Orion A in [CII] (Higgins et al., 2021). The success of the large mapping project laid the foundation of the SOFIA legacy program FEEDBACK, introduced in section 3.4.

3.1 SOFIA

The Stratospheric Observatory for Infrared Astronomy (SOFIA) is a modified Boeing 747SP that carries a 2.7 m large telescope (which has an effective diameter of 2.5 m) as shown in Fig. 3.1. The airborne observatory is a joint German-American (DLR-NASA) project to explore the universe from infrared to sub-millimeter wavelengths. These wavelengths are mostly not accessible by ground-based telescopes because of the poor transmission of the atmosphere. SOFIA operates in the stratosphere at 38,000-45,000 feet (11.6 - 13.7 km), above most of the absorbing atmosphere. This allows to observe lines such as [CII] at 158 μm and [OI] at 63 μm and 145 μm, which are the most important cooling lines of the ISM. The advantage of an Aircraft over a Spacecraft is that instruments can be swapped between flights, maintained, and upgraded. Thus, multiple receivers were used on board SOFIA over its lifetime, such as FORCAST (Faint Object Infrared Camera for the SOFIA Telescope), EXES (Echelon-Cross-Echelle Spectrometer), HAWC+ (High-resolution Airborne Wideband Camera Plus), FIFI-LS (Far Infrared Field-Imaging Line Spectrometer) and GREAT (German REceiver for Astron-

Figure 3.1: The Stratospheric Observatory for Infrared Astronomy (SOFIA) at the Armstrong Flight Research Center in Palmdale, CA, USA, before an observation flight. Credit: S. Kabanovic.

omy at Terahertz Frequencies). In addition, the SOFIA instruments could be tuned during the observations because they are located in the cabin with the science team. The unique mobility of an airborne observatory enables observation not accessible from the ground or spacecraft, such as planetary occultations.

3.2 GREAT

The German REceiver for Astronomy at Terahertz Frequencies (GREAT) is a multi-pixel spectrometer (Risacher et al., 2018) mounted on board SOFIA, which is shown in Fig. 3.2. The GREAT instrument was developed in a consortium between the Max Planck Institute for Radio Astronomy (MPIfR) and the I. Physikalisches Institut at the University of Cologne (KOSMA) in cooperation with the Max Planck Institute for Solar System Research and the DLR Institute of Planetary Research. GREAT is a PI instrument, but supports Open Time observations in collaborative mode.

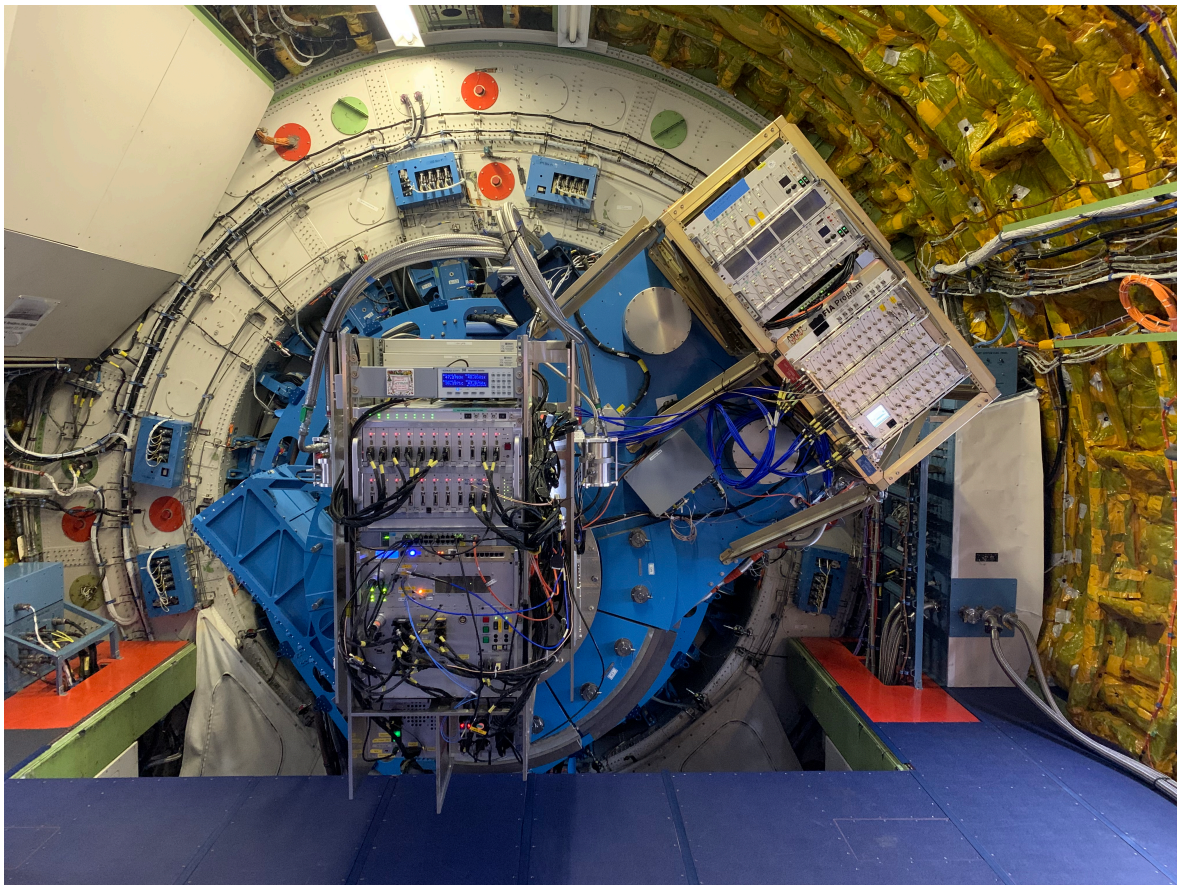

Figure 3.2: German REceiver for Astronomy at Terahertz Frequencies (GREAT) mounted on board SOFIA. Credit: S. Kabanovic.

The GREAT-instrument was used in two different configurations: 4GREAT and upGREAT. The upGREAT configuration employed two channels, the low-frequency array (LFA) and the high-frequency array (HFA). The LFA consists of two hexagonal arrays, each having 7 pixels per polarization, and covers a frequency range of $1.83 - 2.07$ THz. This allows to observe [C II] and [O I] 145 μm. Both lines can also be observed in parallel (one line in each polarization). The beam size of each pixel at the [C II] frequency is 14.1″. The HFA is also equipped with a 7-pixel hexagonal array but in single-polarization. It gives access to the [O I] 63 μm line with a beam size of 6.3″. LFA and HFA can observe in parallel, covering up to six of the most important cooling lines of the ISM at once. The array geometry is visualized in Fig. 3.3.

The 4GREAT configuration has a single pixel with four channels, covering the frequencies 91–635, 890–1090, 1240–1525, and 2490–2590 GHz (Duran et al., 2021). The covered frequency range allowed access to the high-J rotational lines of CO.

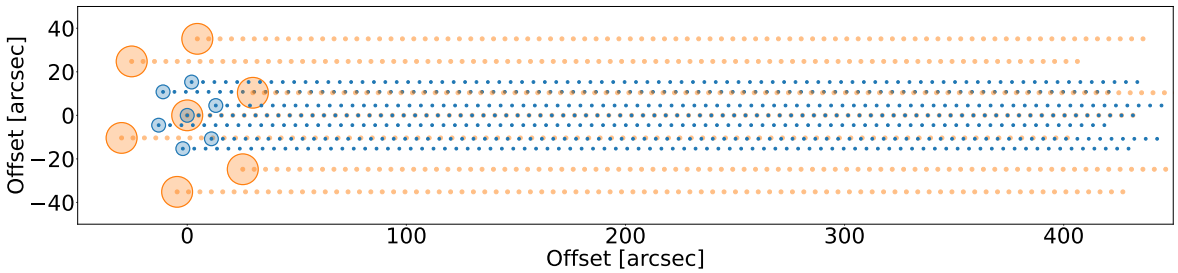

Figure 3.3: GREAT pixel geometry. The GREAT LFA is shown in orange and HFA in blue. The orange and blue dots indicate the 84 dumps every 5.2″ during a single scan. The array is rotated by −19.1° relative to the scanning direction. LFA produces in a single scan a 72.6″ wide stripe and the HFA a 27.2″ wide stripe.

3.3 C^+ Squad: Large scale [CII] emission from Orion A

In a pilot project during open time (OT), a 1.15 square degree velocity resolved map of Orion A was covered in the [CII] line (PI A. Tielens, ID 04_0066). With ∼ 2.4 million spectra observed (and ∼ 0.6 million spectra inside the gridded spectral cube), this is the largest high angular resolution [CII] spectral data cube so far observed. The project was observed over 13 flights during two flight series in November 2016 and February 2017. To cover this large area in a reasonable time, the on-the-fly (OTF) array mapping approach was chosen, which utilizes the hexagonal geometry of the GREAT-pixel array. This observing method allows us to observe a 72.6″ wide stripe with just two scans separated by 5.2″ (each pixel has a beam size of 14.1″), see Fig. 3.3. In contrast to the classical OTF scan, where each position in the map is covered with every pixel of the array (besides the map edge), like in a single-pixel observation mode, we lose S/N and pixel redundancy but gain significant mapping speed. To compensate for this loss, the map is observed twice, with the second coverage perpendicular to the first scanning direction. Each position on the sky is then covered by at least 4 pixels. The large size of Orion required to split the target area into 78 square tiles (Higgins et al., 2021) with a side length of 435.6″. The size of a tile is determined by the stability of the system, thus the amount of time one can spend on target until an off-position measurement becomes necessary due to drifts in the system. For the GREAT instrument, an appropriate time on target was approximately $\lesssim 30$ s. To achieve a map sampled every 5.2″, the spectrometers integrated for 0.3 s while the telescope moved across the target tile at a constant speed, resulting in 84 spectra per scan and array pixel.

The observations can be affected by standing waves due to back-reflections on parallel mirror surfaces in the radiation path, such as the secondary mirror or between the amplifier chain. The baseline of the spectra can thus show features that need to be corrected. A common procedure is a polynomial fit to the spectral baseline struc-

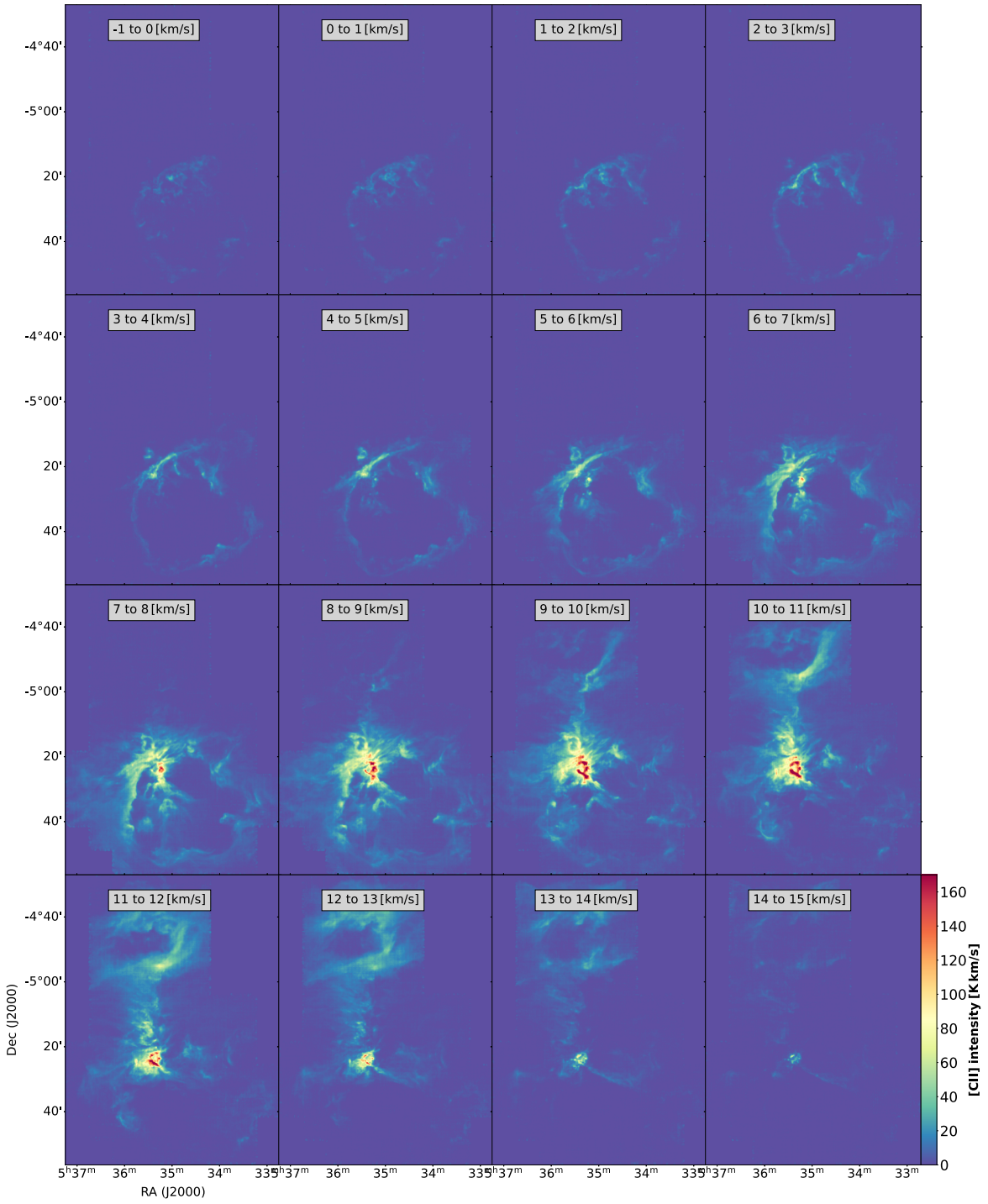

Figure 3.4: Channel maps [CII] emission from Orion A between -1 to 15 km s^{-1}. At blueshifted velocities, the Orion Veil is visible toward the south. At the systemic velocity of $\sim$ 10 km s^{-1}, M 43 and the Huygens Region which includes the characteristic PDR Orion Bar are visible at the center of the map. Toward redshifted velocities, NGC 1977 becomes visible to the north.

ture, assuming that these baseline features are slowly changing and, therefore, can be interpolated below the emission line. However, this assumption is not always valid. While choosing a suitable polynomial order for a single spectrum is straightforward, it is not feasible to do so for millions of spectra. In such cases, a simple polynomial order 3 fit is used to correct the baseline for low-order effects such as an offset or a linear slope, which usually leaves baseline artifacts in the resulting map. To correct the remaining higher-order artifacts, Higgins et al. (2021) fitted the observed off-spectra with a spline profile generating a spline catalog for the observed data. Each baseline of the on-spectra is then compared to the spline catalog. Each spline is scaled on the baseline, and the minimum chi-square of the subsequent fit determines the best match.

The resulting channel maps of the [C II] emission in Orion A is shown in Fig. 3.4. The spectral cube is convolved with a Gaussian kernel to a resulting resolution of 18″. The strongest [C II] emission arises from the bright PDRs in the center of the map at the systemic velocity $\sim 10\,\mathrm{km\,s^{-1}}$, illuminated by the star θ^1-Ori C. Lower-surface brightness [C II] emission is found everywhere in the map and correlates well with IR emission seen by the Spitzer telescope. In channel maps (see Fig. 3.4) and position-velocity maps, shown in Higgins et al. (2021) and Pabst et al. (2020), the three expanding bubbles were identified: NGC 1977 (to the north at redshifted velocities), M 43 (toward the center at the systemic velocity), and the Orion Veil (toward the south at blueshifted velocities), which give Orion A its characteristic dragon-like shape.

A first analysis of the velocity resolved spectra revealed that [C II] is a direct tracer of the gas kinematics. Pabst et al. (2019, 2020) showed that the Orion Veil bubble, located to the south of the Orion A complex, is expanding fast with a velocity of $13\,\mathrm{km\,s^{-1}}$, compressing the surrounding medium to a thin shell. It was determined that the bubble is stellar wind-driven, where mechanical energy is efficiently converted into the kinetic energy of the expanding shell. These remarkable results showed that the effects of the stellar wind on the energy balance of the ISM had been underestimated so far.

3.4 SOFIA legacy program FEEDBACK

The SOFIA legacy program FEEDBACK was initiated after the Orion A large-scale mapping pilot project. In this open time program, the [C II] 158 μm line and the [O I] 63 μm line were observed in parallel. PIs are A. Tielens from the University of Maryland and N. Schneider from the University of Cologne. A team of ∼30 experts from world-wide institutes constitutes the consortium. The program was granted ∼100 hours of observing time and started in 2019 (Program number 07_0077). It was finished at 77% of the proposed area observed when the SOFIA program was terminated in September 2022. The overall goal of this project is to investigate how stellar feedback by massive stars impacts the surrounding interstellar medium. More specifically, FEEDBACK

Table 3.1: FEEDBACK sources overview (Schneider et al., 2020).

Region	RA (1)	Dec (2)	D_{HD} (3)	FUV (4)	Spectral type (5)
Cygnus X	20:38:20.22	42:24:18.29	1.4[a]	290	∼ 50 O, 3 WR
M 16	18:18:35.69	-13:43:30.98	1.74[b]	300	1 O4, ∼ 10 late O
M 17	18:20:43.16	-16:06:14.87	1.98[c]	1295	2 O4, ∼ 10 late O
NGC 6334	17:20:14.07	-35:55:05.18	1.3[d]	580	5 O5–8, 8 B
NGC 7538	23:13:46.41	61:31:42.01	2.65[e]	904	1 O3
RCW 49	10:24:11.57	-57:46:42.50	4.21[f]	555	2 WR, 12 early O
RCW 79	13:40:05.86	-61:42:36.94	4.2[g]	140	2 O4, ∼ 10 late O
RCW 120	17:12:22.82	-38:26:51.61	1.68[b]	375	1 O8
RCW 36	08:59:26.81	-43:44:14.06	0.95[h]	413	1 O8, B-cluster
W 40	18:31:28.58	-02:07:35.39	0.26[i]	237	1 O, 2 B
W 43	18:48:01.04	-01:58:22.27	5.49[j]	741	OB, WR cluster

(1, 2) Coordinates of the central position of the observed [C II] maps.
(3) Distance to the sources in kpc. [a]Rygl et al. (2012), [b]Kuhn et al. (2019), [c]Wu et al. (2019), [d]Chibueze et al. (2014), [e]Moscadelli et al. (2009), [f]Cantat-Gaudin et al. (2018), [g]Russeil et al. (1998), [h]Massi et al. (2019), [i]Ortiz-León et al. (2017), [j]Zhang et al. (2014)
(4) Spatially averaged FUV-field in Habing units [G_0], determined from the 70 μm and 160 μm Herschel FIR-flux maps (Schneider et al., 2016).
(5) Dominant stars and their spectral types.

helps to determine the radiative coupling of PDR gas to FUV photons, quantify the energy injection into the ISM by winds and radiation, and determine radiative heating efficiencies. The great value of FEEDBACK is that it observes 11 galactic high mass star formation regions in [C II] and [O I] 63 μm and thus allows to compare the properties of regions with different physical conditions and to obtain a larger sample that can also be used to compare to extragalactic studies.

Table 3.1 lists the observed sources with their central coordinates, distance, average FUV field, and associated stellar cluster. All these star formation regions were chosen so that a large variety of physical conditions is covered. For example, RCW 120 has only a single O-type star approximately at the center of the spherical H II region (sect. 3.4.1), while Cygnus X contains a massive OB-type cluster with more than 160 OB stars with a complex spatial distribution (sect. 3.4.2).

To cover the 11 targets, we profited from the high observing speed of the OTF array mapping. Since the HFA array beam size is much smaller than that of the LFA, see Fig. 3.3, it is generally the leading array to achieve fully sampled maps for both observed lines. However, the small array size of the HFA would require a substantial amount of time to cover the entire target areas in the "classical" observing mode.

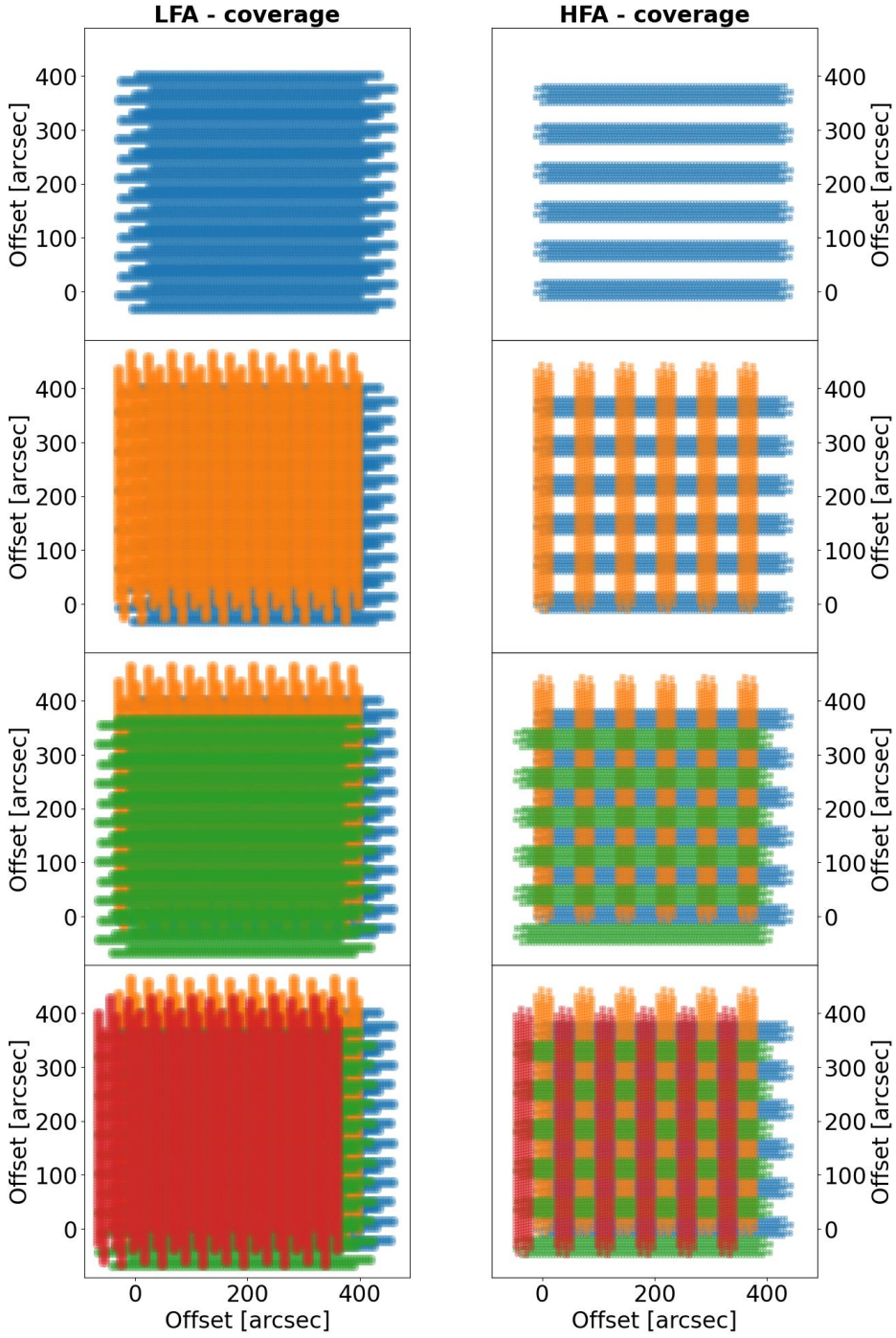

Figure 3.5: FEEDBACK mapping scheme to optimize the observations of [CII] and [OI] that were carried out in parallel. Left panel: The four coverages with the LFA ([CII] observations). Right panel: the resulting pattern for the coverage with HFA ([OI] observations). The first coverage is shown by the blue data at the top. The second coverage, which the scanning direction perpendicular to the first coverage, is shown below in orange. Then, both arrays are shifted by (-36″, -36″). The following two panels show the third coverage in green (scanning direction parallel to the first coverage) and the fourth coverage in red (scanning direction parallel to the second coverage).

Thus, an alternative approach was used to optimize the mapping speed, as shown in Fig. 3.5. Each tile is covered four times in the OTF array mapping mode using LFA as the leading array. First, two coverages with perpendicular scanning directions to each other are performed as described in section 3.3, see also Fig. 3.5. This produces a fully sampled [CII] map with enough pixel redundancy. To cover the missing positions in the [OI] map, we observe two additional coverages shifting the array by (-36″, -36″). With this method, the S/N of the [CII] map was increased, which gives access to the weak [^{13}CII] lines, and a continuous, approximately beam sampled [OI] map could be achieved.

As discussed in section 3.3 the spectral baseline might be affected by instabilities in the atmosphere or the instrument. The standard baseline reduction method of subtracting a polynomial fit from the baseline might not be sufficient for some spectra. In order to ensure the best possible data quality, we employ a more sophisticated method that is based on methods of the principle components analysis (PCA). In short, PCA determines the "eigenspectra" of the observations, which trace most of the variability of the emission-free off-spectrum (Buchbender in prep.). Subsequently, these components are subtracted, which removes the systemic variations from the on-spectra resulting in a flat baseline. A more detailed description of PCA is found in Tiwari et al. (2021); Schneider et al. (2023).

One of the objectives for the FEEDBACK observations of the 11 high-mass star formation regions (Table 3.1) was to quantify the different feedback processes from stellar winds and stellar radiation. While the energy carried by the stellar wind is only a fraction compared to stellar radiation, Luisi et al. (2021); Bonne et al. (2022) showed that the energy from stellar winds can be converted efficiently into the kinetic energy of the expanding bubble.

In the following, I will give an overview of the two regions that were studied within this thesis, RCW 120 and Cygnus X.

3.4.1 RCW 120, the perfect bubble?

The HII region RCW 120 and its associated molecular cloud is located at a distance of $\sim 1.7\,\mathrm{kpc}$ (Kuhn et al., 2019). Figure 3.6 shows an IR image of this region, nicely illustrating how hot ionized gas fills a bubble-like cavity surrounded by a ring of denser and cooler gas associated with a bright PDR. For that reason, RCW 120 is often referred to as the perfect bubble (Deharveng et al., 2009). RCW 120 is excited by a single ionizing O6-8/III type star located slightly south of the center of the HII region. The region was studied at many wavelengths (see Kabanovic et al. (2022) and references therein), but never in the [CII] line and in higher-J CO lines. This was done within FEEDBACK and the line integrated [CII], ^{12}CO and ^{13}CO ($3 \rightarrow 2$) maps between -20 to $10\,\mathrm{kms}^{-1}$ are shown in Fig. 3.7. The [CII] emission, as shown in Fig. 3.7a, displays the characteristic ring-like shape of RCW 120 since the emission from the ionized

Figure 3.6: Infrared image of the Galactic H II bubble RCW 120, seen with the Spitzer telescope. The H II region is visible in red at 24 μm emission and indicates ionized gas mixed with hot dust inside the bubble. Cooler dust and gas is seen as a ring-like feature at 5.8 and 8 μm emission in blue/green. In particular, the UV illuminated edge of the ring shows up as bright PDR in grey/white. The ring is broken in the north, where ionized gas can escape into the interstellar medium. Credit: Spitzer Space Telescope, IRAC, MIPS.

carbon traces the warm surrounding PDR surfaces. However, low-surface brightness [C II] emission is also visible from the projected center of the H II region.

CO emission is shown in Fig. 3.7b and Fig. 3.7c for ^{12}CO and ^{13}CO ($3 \rightarrow 2$) respectively. The data were observed with the Atacama Pathfinder Experiment (APEX), supplementing the [C II] SOFIA observation. The molecular emission does not show the spherical geometry of RCW 120 as clearly, but rather traces the cold clumpy material found deeper in the surrounding cloud. The molecular layer encloses the ionized layer, forming the characteristic PDR layering in a U-shaped geometry with an opening to the north. In addition, two lanes, visible in ^{13}CO (Fig. 3.7c), span diagonally across the H II bubble. These two lanes are clearly visible in Hα absorption and thus are located in front of the H II region (Zavagno et al., 2007). In the dense molecular cloud,

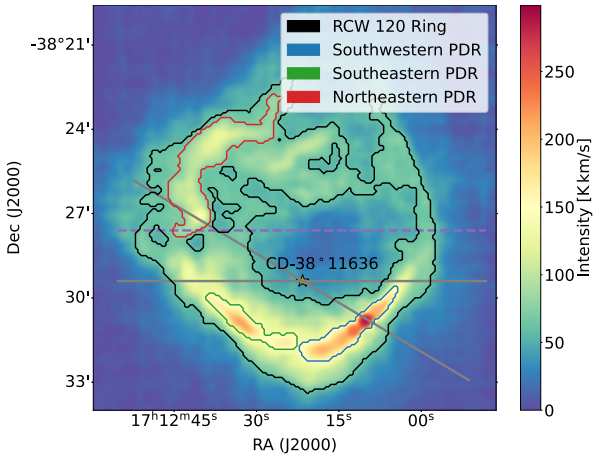

(a) [C II] emission.

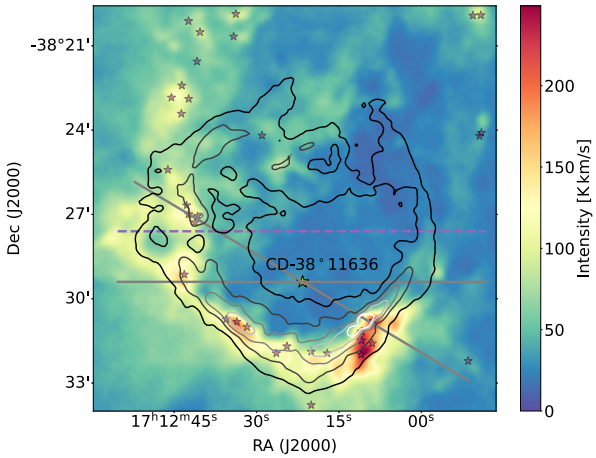

(b) ^{12}CO (3 → 2) emission.

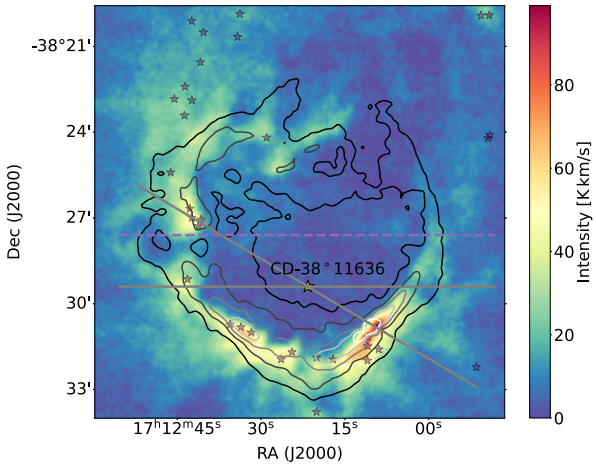

(c) ^{13}CO (3 → 2) emission.

Figure 3.7: Intensity maps of RCW 120 integrated between −20 and 10 kms^{-1}. (a) Line integrated [C II] emission. The colored contours outline the clusters determined by a dendrogram-based approach (Rosolowsky et al., 2008; Robitaille et al., 2019). (b) and (c) show the color coded line integrated ^{12}CO and ^{13}CO (3→2) emission. The [C II] contours range from black to white in intensity levels of 60, 100, 140, 180, 220 K kms^{-1}. The two grey lines indicate the positions used for the position-intensity diagrams shown in Fig. 5.14. The diagonal cut encloses an angle of 25° with the horizontal line. The horizontal purple dashed line through the region's center indicates the location of the position-velocity diagrams shown in Fig. 5.5. The yellow star symbol marks the ionizing O6-8V/III type star CD-38°11636. The magenta stars indicate young stellar objects along RCW 120 (Figueira et al., 2017).

multiple condensations are found (Deharveng et al., 2009), which contain young stellar objects (YSO) indicated by the magenta dots in Fig. 3.7 (Figueira et al., 2017). This suggests that the expanding H II bubble compressed the surrounding molecular cloud, possibly causing new stars to form in the dense clumps. It is actively discussed (Deharveng et al., 2009; Luisi et al., 2021) if these clumps were pre-existing since molecular clouds always show an inhomogeneous cloud structure, or if the gas was compressed in a dense, mostly intact ring/torus that then fragmented into clumps.

3.4.2 The massive star formation region Cygnus X

The Cygnus X region is one of the most massive star-forming giant molecular complexes in the Milky Way. It extends over ∼100-150 pc and has a mass of a few 10^6 $M_\odot$ (Schneider et al., 2006). Figure 3.8 shows a molecular line survey in ^{13}CO (1→0) with the FCRAO (Five College Radio Astronomy Observatory) of Cygnus X (Schneider et al., 2011), where the individual molecular clouds are identified. In the northeastern part, the DR21 and W75N clouds are located, which are the subject of this thesis. The view on the Cygnus X region changed in the last decades. In the 1990's, the complex was considered as a chance alignment of clouds along the line of sight (Wendker et al., 1991). This view was challenged with IR- and CO-surveys, where it was proposed that Cygnus X is a massive concentration of clouds at a common distance of around 1.7 kpc (Schneider et al., 2006; Reipurth and Schneider, 2008). Maser parallax measurements (Rygl et al., 2012) confirmed this scenario and placed objects in the Cygnus X complex at distances between 1.4 and 1.7 kpc. How such a large complex can form, however, remains an unsolved question.

Cygnus X has a rich cluster of 169 OB-type stars, which irradiates the surrounding gas with ionizing radiation. The UV field (see section 4.5 for a detailed description of how the UV field was determined) originating from the massive cluster is shown in Fig. 5.23. The observed [C II] map is indicated by the grey outline in Fig. 3.8, is located well outside the stellar cluster and, therefore, only weakly illuminated at UV field values below $< 30\,G_0$. The observed map contains the two prominent regions DR21 and W75N, which are located within the dense filamentary structures. Southwest of DR21, we find an H II region usually referred to as the diamond ring, see grey subpanel in Fig. 3.8. Cygnus X is particularly interesting because it shows many sequential stages of star formation. Thus, Cygnus X might be ideal for our overall understanding of star formation in the Milky Way and to bridge our understanding of extra-galactic molecular clouds and star formation.

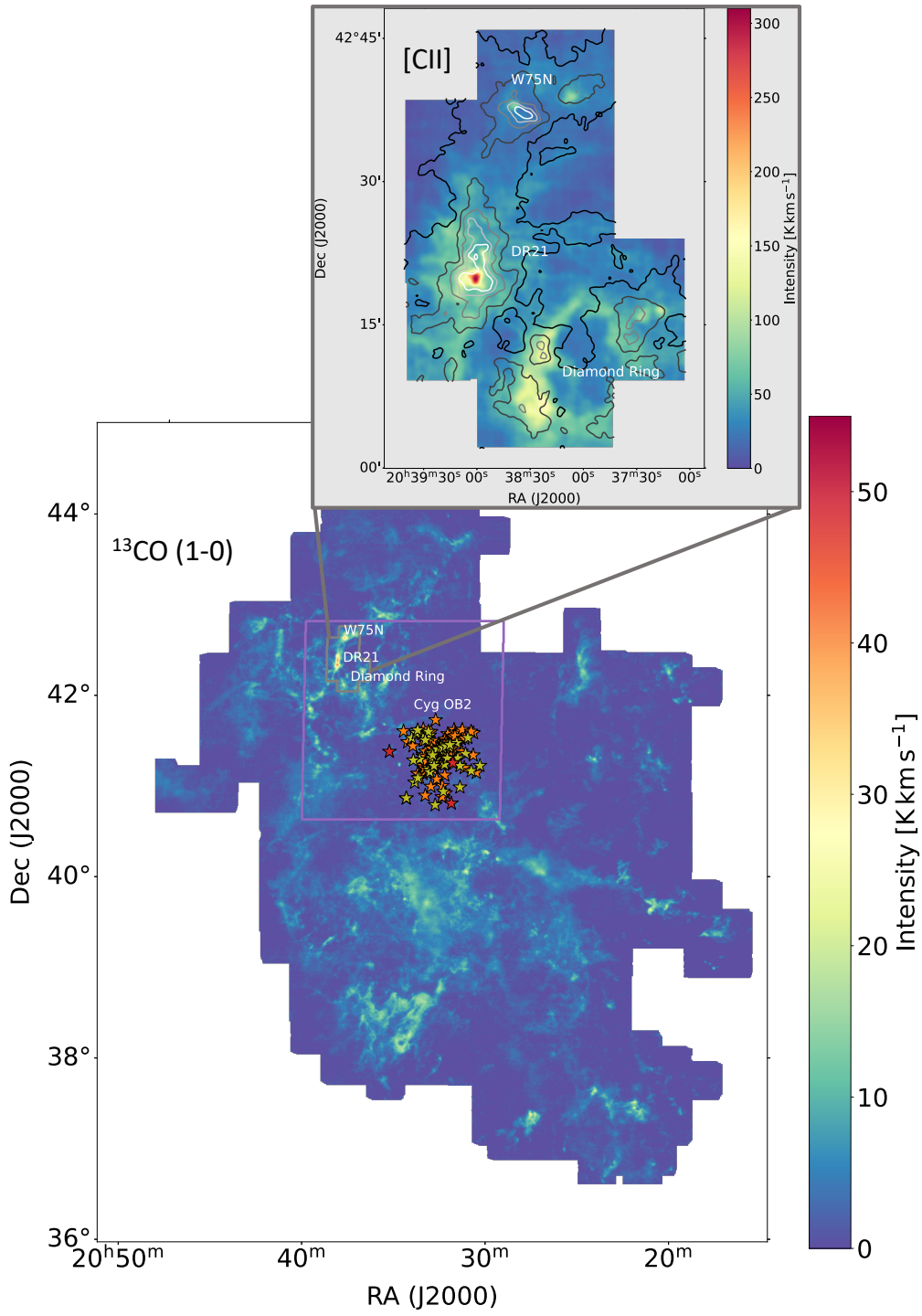

Figure 3.8: ^{13}CO (1→0) line integrated emission (-10 to 20 K km s^{-1}) of the Cygnus X region (Schneider et al., 2011). The Cyg OB2 cluster is indicated by the star symbols which show the position of the O-type stars in yellow, B-type stars in orange and the Wolf-Rayet stars in red. The purple box indicates the area the UV-field is determined in, see Fig. 5.23. The grey outlines show the observed [C II] area. The upper grey subpanel shows the observed integrated [C II] emission (-10 to 20 K km s^{-1}). The contours show the corresponding ^{12}CO (1→0) emission. The contour levels range from black to white in 60, 120, 180, 240, 300 K km s^{-1}.

Methods

~ $ pip install astrokit

In the context of this thesis, I used existing tools for data analysis but also developed a variety of (numerical) methods to reduce, analyze, and model the observed spectral data. In this chapter, I introduce these procedures. I start with an overview of the Python-based open-source library astrokit (section 4.1). In the following section 4.2, I describe two machine learning (ML) based clustering methods suitable for spectral data cubes. In section 4.2.1, I introduce a dendrogram based method (Rosolowsky et al., 2008), which hierarchically clusters the spectral data. In the following section 4.2.2, the Gaussian mixture model is described, a probabilistic approach with a flat cluster hierarchy in contrast to dendrograms. Section 4.3 introduces the two-layer multi-component model based on an approach first introduced by Guevara et al. (2020). I developed a fully automated version of the model, which solves the radiative transfer equation unsupervised for the entire spectral cube. Section 4.4 gives an introduction to the determination of moment maps. In the last section 4.5, I describe the method used to determine the local FUV-field.

4.1 Astrokit

Modern state-of-the-art receivers such as upGREAT on board SOFIA enable observations of square degree size regions, such as the large Orion A map (Higgins et al., 2021) or the FEEDBACK map in Cygnus X (Schneider et al., 2023) observed in [CII]. These spectral data cubes contain millions of velocity-resolved spectra, which makes it infeasible to reduce and analyze every single spectrum manually and by eye inspection. Automatic procedures that first perform a data quality assessment, i.e., determine the rms noise of the spectra and remove bad quality data due to spikes or baseline problems, are required. In a next step, an efficient way to visualize whole spectral cubes in the form of moment maps (see sect. 4.4), channel maps, or position-velocity (PV)

cuts are required (see below). For these purposes, in the framework of this thesis I developed the python-based software package astrokit[1], which includes various functions and methods to reduce, analyze and model spectral data cubes. The python library is open source and, therefore, freely accessible. It would go beyond the scope of this thesis to introduce the entire set of tools included in astrokit, but here I summarize the most important features:

- Functions for the analysis and assessment of the data quality of a spectral data cube are included that determine rms, moment-, channel-, and PV-maps. These tools were applied to perform a first analysis of the observed [CII], CO, and HI data for all publications to which I contributed, in particular in Higgins et al. (2021); Kabanovic et al. (2022), and Schneider et al. (2023).

- Tools to derive physical conditions, such as optical depth, molecular and atomic line column densities, excitation temperature, mass, and luminosity are included and were applied in, e.g., Luisi et al. (2021) and Kabanovic et al. (2022) to derive the physical conditions of the fast-expanding shell and PDR in RCW 120.

- Sophisticated multi-line analysis tools, such as the two-layer multicomponent model, are incorporated in (section 4.3). This new implementation of the two-layer model was used to investigate possible self-absorption effects in the Musca filament (Bonne et al., 2020) and to determine the physical properties of the cold atomic layer embedding RCW 120 by Kabanovic et al. (2022). In addition, an automatized version of the model was used to estimate the spatial distribution of the cold molecular layer in front of RCW 120. Therefore, we cluster the spectral data cube by applying the Gaussian mixture model (GMM) to find an appropriate number of initial input parameter for the two-layer model.

- Functions are included to quantify the amount of cold self-absorbing hydrogen (HISA) and its spatial distribution from spectrally resolved HI observation. The HISA analysis was used by Kabanovic et al. (2022), and Schneider et al. (2023) to determine the physical properties of the cold atomic gas.

- The information on the local FUV field is an important PDR model input parameter. Thus, astrokit includes tools to derive the 3D FUV-field from the local census of stars, described in section 4.5. With this method, I calculated the FUV-field for the Cygnus X region (Schneider et al., 2023) and provided the FUV maps for all FEEDBACK sources for future publications.

[1] https://github.com/skabanovic/astrokit

- Functions to determine high angular resolution column density maps from the FIR flux observed with the Herschel satellite are included. This method is based on the ideas presented in Palmeirim et al. (2013) and increases the angular resolution of the final maps from 36″ to 18″. The maps were used by Schneider et al. (2022) to produce probability distribution functions of column density (N-PDFs) and investigate the physical processes that determine the shape of the N-PDFs.

The above list is by no means a complete representation of the included functions, but should rather give the reader a first impression about the functionality of astrokit.

4.2 Revealing the structures of the ISM

A common approach to get quick access to the spectral structure of the observed region is a simple average of all spectra in the data cube. We here assume that the molecular cloud's physical properties determine the observed spectrum's spectral shape; however, a simple average over the entire spectral data cube goes along with the loss of the spatial information. Thus, to preserve some spatial information in the map, similar spectra which share specific attributes such as intensity, velocity, or width can be gathered into clusters. There are various ways to cluster multidimensional data based on machine learning (Brunton and Kutz, 2019). I here introduce two clustering algorithms used in the framework of this thesis.

4.2.1 Dendrograms

A widely used method to find structures in astronomical data sets are dendrograms (Rosolowsky et al., 2008; Robitaille et al., 2019) that implement a hierarchical way to cluster spectra. The dendrogram algorithm is an unsupervised ML approach that finds a unique solution for a set of initial conditions:

- **Minimum significance**: Determines if an intensity difference has to be considered significant.
- **Minimum value**: A lower threshold, which excludes data points below a certain intensity.
- **Minimum pixel number**: Determines the lower threshold for the number of pixels in a structure for a 2D or 3D data set.

A schematic representation of the algorithm is shown in Fig. 4.1. The dendrograms approach determines local intensity maxima as clusters in a hierarchical fashion. The largest structure enveloping all sub-structures is called the trunk and it is confined by the minimum value given. Structures that do not contain any further sub-structure are

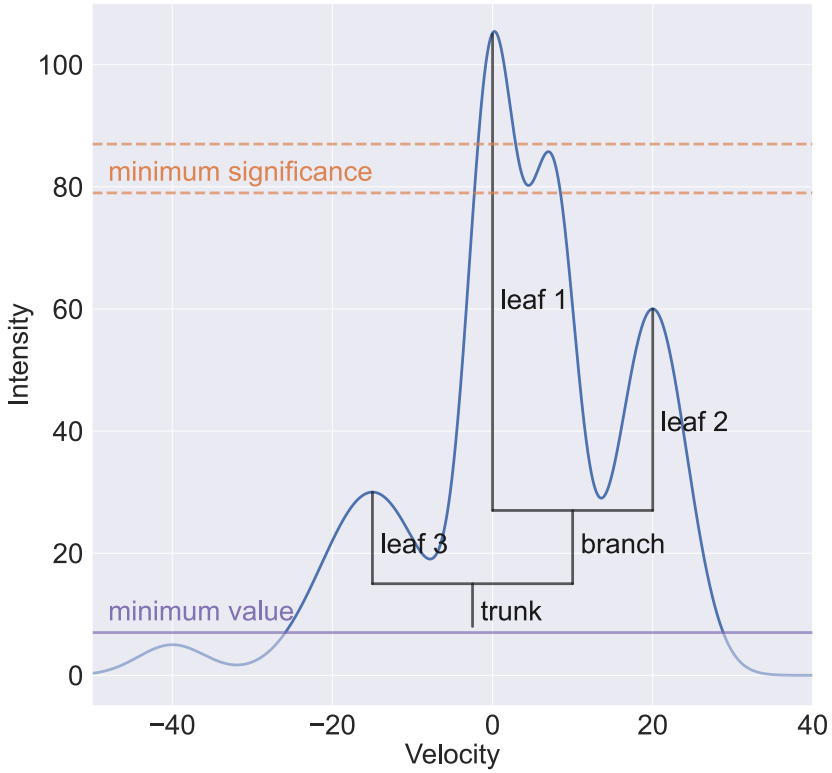

Figure 4.1: Schematic example of the Dendrogram algorithm.

referred to as leaves. The intensity of a leaf needs to be larger than the value of the minimum significance. Two leaves are separated by a local minimum from a branch, which is a sub-structure of the trunk, see Fig. 4.1.

For a spectral data cube, the noise of the spectrum determines the minimum significance. In case the dendrogram approach is used on an integrated spectral 2D map, the corresponding minimum significance ΔI can be derived by error propagation of the integrated rms σ_{rms} over N channels:

$$\begin{aligned}\Delta I &= \sqrt{\sum_{i=1}^{N}\left(\frac{\partial I_i}{\partial T_i}\sigma_{\mathrm{rms}}\right)^2} \\ &= \sqrt{\sum_{i=1}^{N}\left(\frac{\partial T_i}{\partial T_i}\Delta v_{\mathrm{ch}}\sigma_{\mathrm{rms}}\right)^2} \\ &= \sqrt{\Delta v_{\mathrm{ch}}^2\sigma_{\mathrm{rms}}^2 N} \\ &= \Delta v_{\mathrm{ch}}\sigma_{\mathrm{rms}}\sqrt{N}\ ,\end{aligned} \tag{4.1}$$

with the channel width Δv_{ch}.

It is reasonable to set the minimum value to the detection limit of 3σ or higher. In the framework of this thesis, I used the dendrogram approach to extract the bright PDRs from the data cubes. In this case, the chosen minimum value is region-specific. Thus, the values are set high enough so that the faint emission surrounding the PDRs is neglected.

The minimum number of pixels that a cluster should contain to be identified as a structure can be determined by the beam size θ_{mb} and the pixel size $\theta_{\mathrm{RA}}\theta_{\mathrm{Dec}}$. A structure is considered to be significant if it extends over three times the area covered by the main beam. The minimum number of pixels subtending this area can be calculated by:

$$N_{\mathrm{pix,min}} = \frac{3}{4}\pi \frac{\theta_{\mathrm{mb}}^2}{\theta_{\mathrm{RA}}\theta_{\mathrm{Dec}}} \ . \tag{4.2}$$

This approach is especially useful for extracting faint lines hidden in the noise. While simply averaging over large areas decreases the noise N, such an approach might also decrease the signal S if areas of low intensity are included. With the dendrogram approach, it is possible to distinguish regions with strong emission where the resulting averaged spectrum has a high S/N, which allows us to detect weak lines such as the [^{13}C II] hyperfine transition (Kabanovic et al., 2022).

4.2.2 Gaussian Mixture Model

The Gaussian Mixture Model (GMM) is a probabilistic unsupervised ML clustering method that groups data by a linear combination of multidimensional Gaussians (Brunton and Kutz, 2019). GMM is a robust clustering approach that is used in a variety of "Big Data" applications. To utilize GMM for spectral data cubes, I follow the approach introduced by Kabanovic et al. (2022). Each spectrum $\boldsymbol{s}$ of the spectral cube $\boldsymbol{S}$ is defined as a D dimensional vector, where D is the number of spectral channels. The probability distribution function of the data set $P(\boldsymbol{s})$ is described as a weighted superposition of multiple Gaussian distributions $\mathcal{N}(\boldsymbol{s}; \boldsymbol{\mu}_k, \Sigma_k)$:

$$P(\boldsymbol{s}) = \sum_k \boldsymbol{\phi}_k \ \mathcal{N}(\boldsymbol{s}; \boldsymbol{\mu}_k, \Sigma_k) \ , \tag{4.3}$$

in which the multidimensional Gaussian distribution is defined as

$$\mathcal{N}(\boldsymbol{s}; \boldsymbol{\mu}_k, \Sigma_k) = \frac{\exp\left(-\frac{1}{2}(\boldsymbol{s}-\boldsymbol{\mu}_k)^T \Sigma_k^{-1} (\boldsymbol{s}-\boldsymbol{\mu}_k)\right)}{\sqrt{(2\pi)^D |\Sigma_k|}} \ , \tag{4.4}$$

with the mean $\boldsymbol{\mu}_k$, which is here a D-dimensional vector, the covariance matrix Σ_k of size $D \times D$, and the corresponding weight $\boldsymbol{\phi}_k$. The probability of a cluster k is given by $P(k) = \phi_k$, with the normalized weight:

$$\sum_k \boldsymbol{\phi}_k = 1 \ . \tag{4.5}$$

The GMM starts with a predefined or random initial state of K clusters. Subsequently, the two-step Expectation-Maximization (EM) algorithm (Dempster et al., 1977) is used, which converges to an optimal solution. First, the "Expectation step" determines the probability of each spectrum $\boldsymbol{s}_i$, $1 \leqslant i \leqslant N$ belonging in cluster $1 \leqslant k \leqslant K$:

$$\gamma_{ik} = \frac{\boldsymbol{\phi}_k \, \mathcal{N}(\boldsymbol{s}_i; \boldsymbol{\mu}_k, \Sigma_k)}{\sum_j^K \boldsymbol{\phi}_j \, \mathcal{N}(\boldsymbol{s}_i; \boldsymbol{\mu}_j, \Sigma_j)} \; . \tag{4.6}$$

Second, the "Maximization step" updates the model parameter:

$$\boldsymbol{\phi}_k = \sum_i^N \frac{\gamma_{ik}}{N} \; , \tag{4.7}$$

$$\boldsymbol{\mu}_k = \frac{\sum_i^N \gamma_{ik} \boldsymbol{s}_i}{\sum_i^N \gamma_{ik}} \; , \tag{4.8}$$

$$\Sigma_k = \frac{\sum_i^N \gamma_{ik} \left(\boldsymbol{s}_i - \boldsymbol{\mu}_k\right) \left(\boldsymbol{s}_i - \boldsymbol{\mu}_k\right)^T}{\sum_i^N \gamma_{ik}} \; . \tag{4.9}$$

The EM algorithm iteratively updates the weights $\boldsymbol{\phi}_k$, the mean $\boldsymbol{\mu}_k$, and the covariance matrix Σ_k of each cluster k in order to maximize the measure of the log-likelihood, which is defined as follows:

$$\log P(\boldsymbol{S}) = \sum_i^N \log(\sum_k^K \boldsymbol{\phi}_k \, \mathcal{N}(\boldsymbol{s}; \boldsymbol{\mu}_k, \Sigma_k)) \; . \tag{4.10}$$

With the above definition, the EM algorithm always converges toward a *local* optimum.

We can simply provide the spectral data cube to the GMM as an input. However, it is useful to reduce the data set's dimension by removing channels dominated by noise. Further, it might be practical to normalize the data set, which might enhance the separation between clusters or reduce the influence of certain features, such as outliers or small local intensity offsets resulting in stripes seen in the intensity maps.

A schematic example of the GMM is shown in Fig. 4.2 for a two-dimensional data set. The example data set is best represented by five different clusters. While some clusters are clearly separated, such as the blue and purple data points, other clusters merge, as indicated by the yellow and dark green data points. In this case, the probabilistic nature of the algorithm comes in handy since the probability of each D-dimensional data point belonging to a cluster is determined. Subsequently, the data point is sorted into the cluster with the highest probability. In addition, the multidimensional nature of Gaussian functions also allows asymmetric clusters, which permits to capture more complex expansion features.

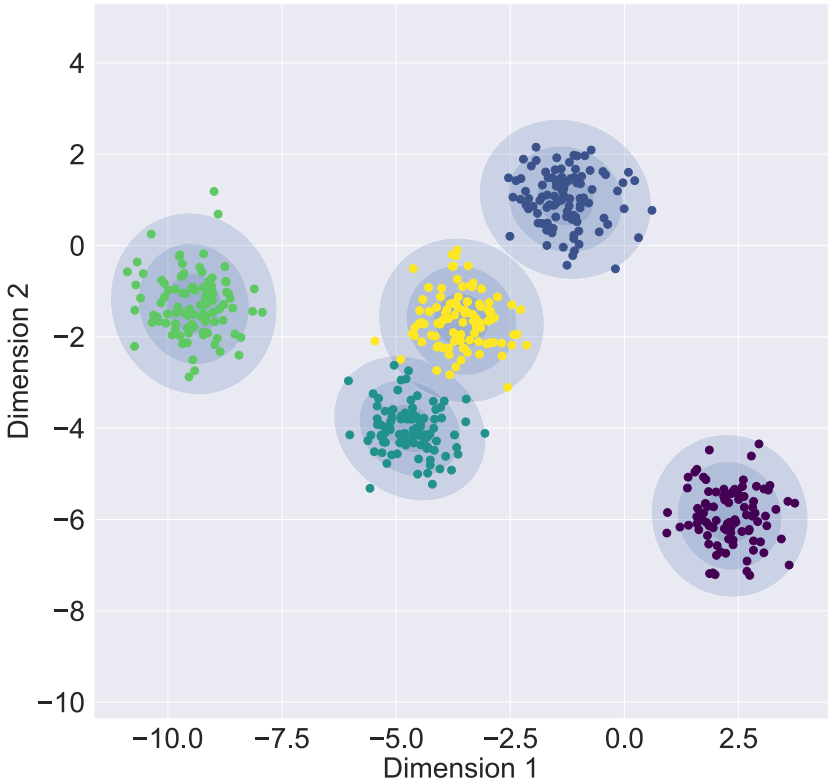

Figure 4.2: Schematic example of the Gaussian mixture model. The colored points show an example 2D distribution. The grey-shaped contours indicate the Gaussian-shaped clusters.

Bayesian information criterion

While the number of clusters is easily determined by eye in our example shown in Fig. 4.2, it is generally not straightforward for multidimensional data sets. Thus, to determine the appropriate number of clusters for a given D-dimensional data set, we employ the Bayesian information criterion (BIC), a common statistical method for model selection (Schwarz, 1978). The BIC for a total number of N spectra and K clusters is given by:

$$\mathrm{BIC}(K) = N_f(K)\log(N) - 2\mathcal{L}(K)\ , \tag{4.11}$$

with the number of independent parameters:

$$N_f(K) = K - 1 + KD + \frac{KD(D-1)}{2}\ , \tag{4.12}$$

and the measure of likelihood $\mathcal{L}$, see equation (4.10).

To determine the (minimum) number of clusters that best describes the spectral cube, we solve the BIC over a range $\boldsymbol{K} = (K_1, K_2; K_3, ...)$ of clusters and choose the

cluster $K = K_i$ which minimizes the BIC. The initial random distribution of clusters can affect the final GMM result. To quantify this effect for a given spectral data cube, we determine the BIC for each number of clusters K_i multiple times: Following the approach of Jones et al. (2019), we perform the calculation a hundred times and subsequently derive the mean BIC and its standard deviation for each number of clusters.

4.3 The two-layer multicomponent model

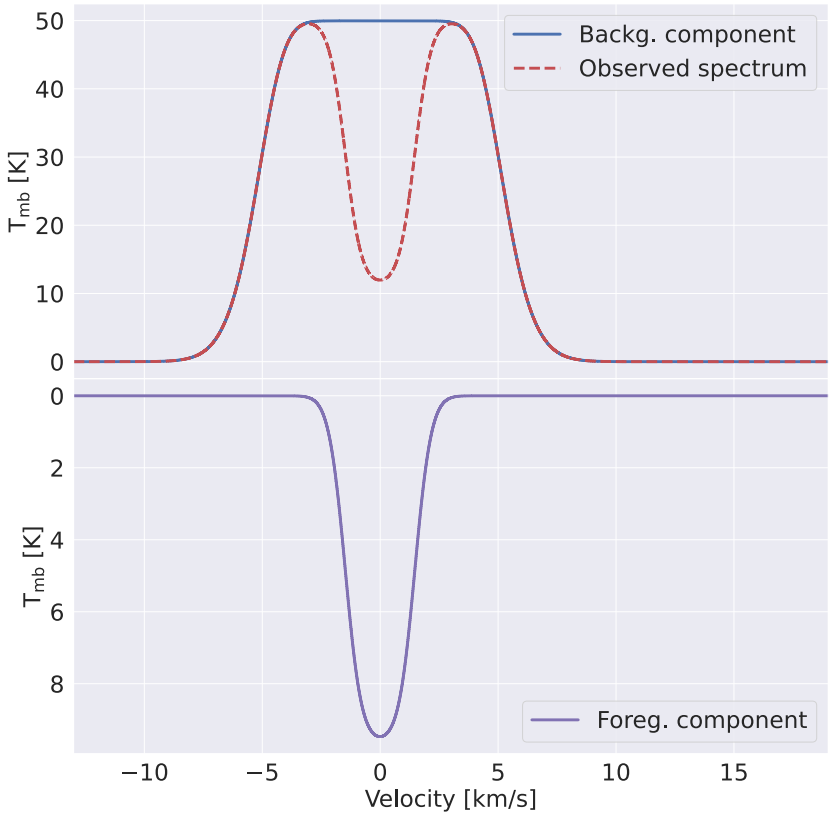

Figure 4.3: Schematic example of an observed H I spectrum. The blue flat-top curve shows an optically thick H I background emission line at an excitation temperature of 50 K. The purple curve shows the emission from the cold 10 K H I foreground. The red dotted curve indicates the observed spectrum after the emission from the warm emitting background is partly absorbed by the foreground along the line of sight.

The two-layer multicomponent model solves the radiative transfer equations for multiple velocity components distributed between two layers. The model was introduced by Guevara et al. (2020) and later adjusted to solve for multiple optically thick overlapping components in velocity space for several transition lines observed in parallel by Kabanovic et al. (2022). Here, I present this advanced version of the two-layer

model based on Kabanovic et al. (2022):

Radiative transfer equation - two-layer multicomponent model

$$
\begin{aligned}
T_{\mathrm{mb}}(v) = \sum_{\nu} \Big\{ & \Big[\mathcal{J}_\nu(T_{\mathrm{ex,bg}}) \left(1 - e^{-\sum_{i_{\mathrm{bg}}} \tau_{i_{\mathrm{bg}}}(v+\Delta v_\nu)} \right) \Big] e^{-\sum_{i_{\mathrm{fg}}} \tau_{i_{\mathrm{fg}}}(v+\Delta v_\nu)} \\
& + \mathcal{J}_\nu(T_{\mathrm{ex,fg}}) \left(1 - e^{-\sum_{i_{\mathrm{fg}}} \tau_{i_{\mathrm{fg}}}(v+\Delta v_\nu)} \right) \\
& + \mathcal{J}_\nu(T_{\mathrm{cont}}) \left(e^{-\left(\sum_{i_{\mathrm{bg}}} \tau_{i_{\mathrm{bg}}}(v+\Delta v_\nu) + \sum_{i_{\mathrm{fg}}} \tau_{i_{\mathrm{fg}}}(v+\Delta v_\nu)\right)} - 1 \right) \Big\} \ . \qquad (4.13)
\end{aligned}
$$

The first sum runs over a set of line transition frequencies which allows to solve the radiative transfer equation for multiple transition lines with transition frequency ν in parallel. However, each line needs to be separated in velocity space, thus the line shift Δv must be significantly larger than the line width w, i.e., $\Delta v \gg w$. This allows to solve the model for two isotopes such as ^{12}CO and ^{13}CO in parallel. In the case of two lines overlapping, as it is the case for [^{12}C II] and [^{13}C II] F(2-1), we can simply address the issue by using a combined line shape approximated with a common transition line frequency $\nu_{[\mathrm{C\,II}]} \approx \nu_{[^{12}\mathrm{C\,II}]} \approx \nu_{[^{13}\mathrm{C\,II}]}$:

$$
\Phi_i(v) = \phi_i(v) + \sum_{\mathrm{F}\rightarrow\mathrm{F}'} s_{\mathrm{F}\rightarrow\mathrm{F}'} \phi_i(v - \Delta v_{\mathrm{F}\rightarrow\mathrm{F}'}) \ , \qquad (4.14)
$$

where $\Delta v_{\mathrm{F}\rightarrow\mathrm{F}'}$ are the line shifts of the three hyperfine transition lines with respect to the primary isotope and $s_{\mathrm{F}\rightarrow\mathrm{F}'}$ are the relative line intensity of the [^{13}C II] lines, see Table 2.1. Each individual line profile $\phi(v)_i$ is described by a normalized Gaussian profile in velocity space:

$$
\phi_i(v) = \frac{2\sqrt{2\ln 2}}{w_i\sqrt{2\pi}} e^{-4\ln 2 \left(\frac{v-v_{0,i}}{w_i}\right)^2} \ , \qquad (4.15)
$$

with $v_{0,i}$ the central (LSR velocity) velocity and w_i the line width of each component i. The factor $2\sqrt{2\ln 2}$ considers that the line width is given as the Full Width at Half Maximum (FWHM) instead of the standard deviation σ_i. For a simultaneous fit of multiple lines, the LSR velocity and width are forced to be common among the lines. However, the excitation temperature is allowed to differ between lines. While the model equation (4.13) has no constraints on the background (bg) and foreground (fg) excitation temperature, we assume, in general, to have a higher background temperature compared to the foreground temperature, $T_{\mathrm{ex,bg}} > T_{\mathrm{ex,fg}}$. This way, most of the bulk emission originates from the warm background, and the cold foreground acts mainly as an absorber. This is a pragmatic assumption since a cold layer behind the warm-emitting cloud does not imprint itself onto the observed spectrum. The cold foreground material can be a separated cloud located between the background region

of interest and the observer. However, it is generally unlikely that an independent foreground cloud is moving with a similar radial velocity as the observed region. The cold foreground generally results from a temperature gradient along the line of sight generated by stars heating the surrounding medium inside the clouds and colder gas with decreasing distance from the stars.

Each model component is characterized by four parameters: excitation temperature, optical depth, line position, and line width. The observed spectrum confines the latter two, which can be determined during the fitting process. The excitation temperature and the optical depth determine the intensity of the observed line and therefore are not independent. In order to get a unique solution from the fit, we must determine one of the two parameters beforehand. For a flat-top, highly optically thick line, the excitation temperature can be determined from the peak line intensity, as shown by the flat-top blue spectrum in Fig. 4.3. However, in general, the information about the optical depth is required to determine the excitation temperature:

$$T_{\mathrm{ex}} = T_0 \ln\left(\frac{T_0}{T_{\mathrm{p,mb}}}\left(1 - e^{-\tau_{\mathrm{p}}}\right) + 1\right)^{-1} . \tag{4.16}$$

Under the assumption that the observed intensity is not obscured by a cold foreground cloud and that the emitting cloud can be characterized by a single excitation temperature, the optical depth can be obtained from the intensity ratio of the primary isotope ^{12}C to the secondary isotope ^{13}C, see equation (2.74). In the case of an absorbing foreground, we can expect the line width of the cold gas to be narrower compared to the warm background, thus we can assume that the background can partly shine through the absorbing foreground (at velocities outside of the systemic velocity of the cloud), as shown by the red dotted spectrum in Fig. 4.3. In this case, we can determine the excitation temperature from the peak intensity and the corresponding optical depth τ_{p}, where we assume the foreground absorption effect to be weak. Since it is not possible to rule out foreground absorption at the intensity peak, we can consider the so-derived excitation temperature as a lower limit.

In case the observed spectrum shows a strong absorption dip, as shown in Fig. 4.3, it is possible to derive an upper limit for the foreground excitation temperature from the temperature at the minimum of the line dip (Guevara et al., 2020). Otherwise, the density and corresponding temperature can be constrained from an independent estimate of the hydrogen column density in front of the observed regions, such as optical absorption measurements. If no additional information is available to constrain the foreground temperature, we can derive a lower limit for the foreground temperature following the energy balance derivation from Kabanovic et al. (2022), which gives a lower temperature limit for [C II] of $T_{\mathrm{ex}} \sim 15\,\mathrm{K}$ (see also section 5.2.2).

With this, we can constrain the excitation temperature of both the background and foreground layers. The optical depth of each component remains as the free parameter.

For a given optical depth and excitation temperature, we determine the corresponding column density. For atomic two-level transitions, as it is the case for [C II] and H I we can use equation (2.63) and for molecular rotation transition lines, we use equation (2.72).

The last term of the radiative transfer model, see equation (4.13), includes the emission from the continuum. For [C II], the continuum emission originates mainly from the cosmic microwave background at $T = 2.7\,\mathrm{K}$, and its contribution is negligible.

The warm emitting background components are derived from the less abundant isotope, such as ^{13}C. In the first step, we solve the radiative transfer equation (4.13) assuming that the foreground has little effect in absorbing photons from the rarer species due to its (by a factor of α) lower abundance. This can be shown without the loss of generality for a single component:

$$
\begin{aligned}
T_{\mathrm{mb}}(v) &= \mathcal{J}_\nu(T_{\mathrm{ex,bg}}) \left(1 - e^{-\tau_{\mathrm{bg}}(v)}\right) e^{-\tau_{\mathrm{fg}}(v)} \\
&\quad + \mathcal{J}_\nu(T_{\mathrm{ex,fg}}) \left(1 - e^{-\tau_{\mathrm{fg}}(v)}\right) && |e^{-\tau_{\mathrm{fg}}(v)} \approx 1 - \tau_{\mathrm{fg}}(v) \\
&\approx \mathcal{J}_\nu(T_{\mathrm{ex,bg}}) \left(1 - e^{-\tau_{\mathrm{bg}}(v)}\right) (1 - \tau_{\mathrm{fg}}(v)) \\
&\quad + \mathcal{J}_\nu(T_{\mathrm{ex,fg}}) \tau_{\mathrm{fg}}(v) && |\tau_{\mathrm{fg}}(v) \ll 1,\ T_{\mathrm{ex,fg}} < T_{\mathrm{ex,bg}} \\
&\approx \mathcal{J}_\nu(T_{\mathrm{ex,bg}}) \left(1 - e^{-\tau_{\mathrm{bg}}(v)}\right) \ .
\end{aligned}
$$

The velocity and line width are assumed to be identical among the two isotopes since the emission originates from the same cloud material and, thus, both isotopes share the same collision partners. The optical depth (or column density) can be converted between the two isotopes by their corresponding local carbon abundance ratio, $\tau_{^{12}\mathrm{C}} = \alpha \tau_{^{13}\mathrm{C}}$. We can simply scale up the background component derived from the secondary carbon isotope to determine the background components of the primary ^{12}C isotope. In a second step, we can now solve the two-layer multicomponent model, eq. (4.13) for the observed spectrum of the primary isotope. In this step, we confine the background parameters of the more abundant isotope using the previously determined parameters of the rare isotope. The background parameters are only allowed to vary in the range determined by the error of the previous fit of the secondary isotope. This way, the background is mostly fixed and the two-layer model tries to find a solution for the foreground. As the primary isotope might have some additional wing components that are buried in the noise for the secondary isotope, we also add background components in the second step, which are only visible in the primary isotope. For additional details see Guevara et al. (2020).

4.3.1 Optimization of the two-layer multicomponent model fit

Finding a solution for the two-layer multicomponent model requires a reasonable initial guess, including the number of background and foreground components, their excitation temperature, velocity, and line width. For a single spectrum, this is a straightforward

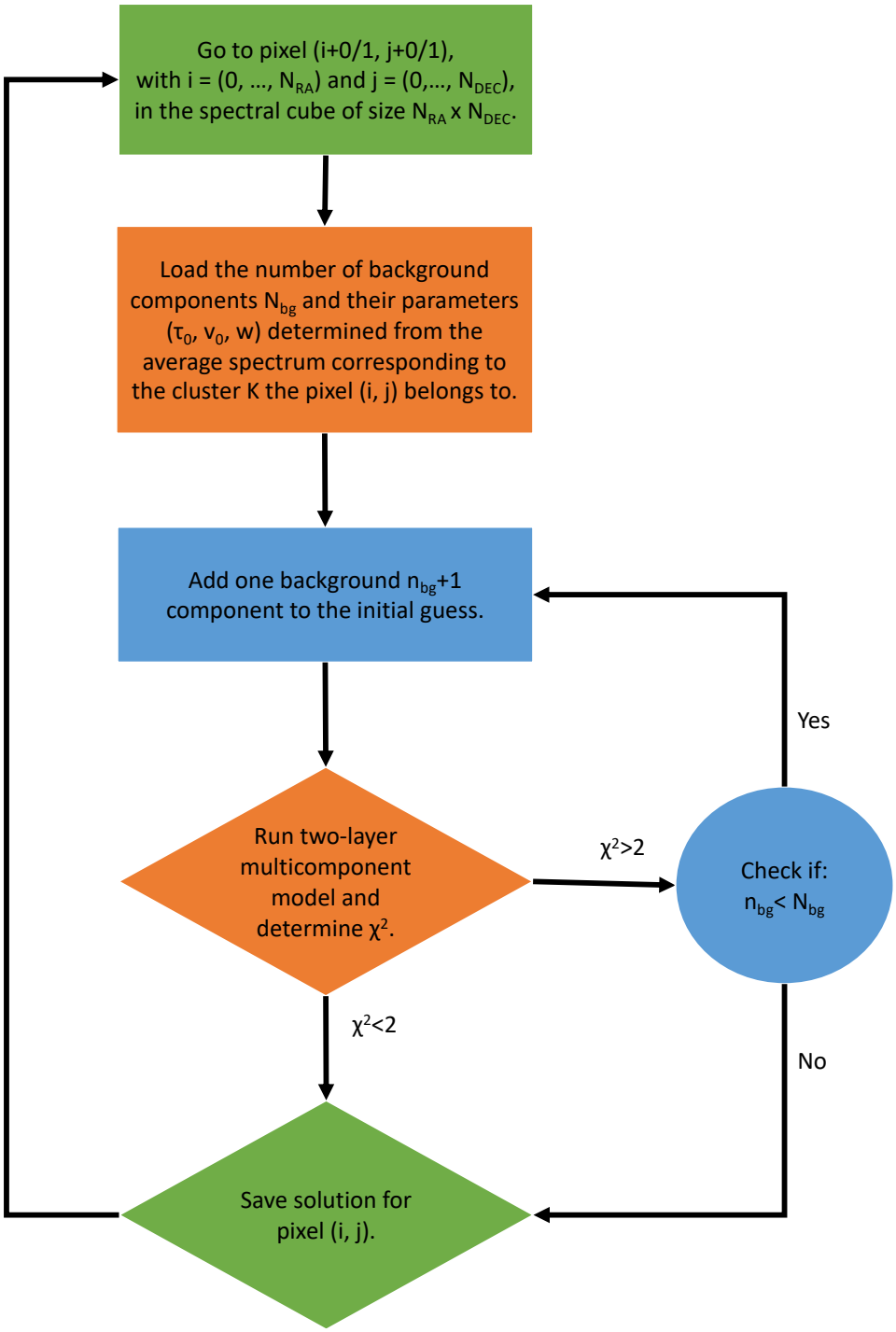

Figure 4.4: Automation of the background component fit. In each iteration, a background component is added until the desired goodness of the fit is achieved or the maximum number of background components is reached.

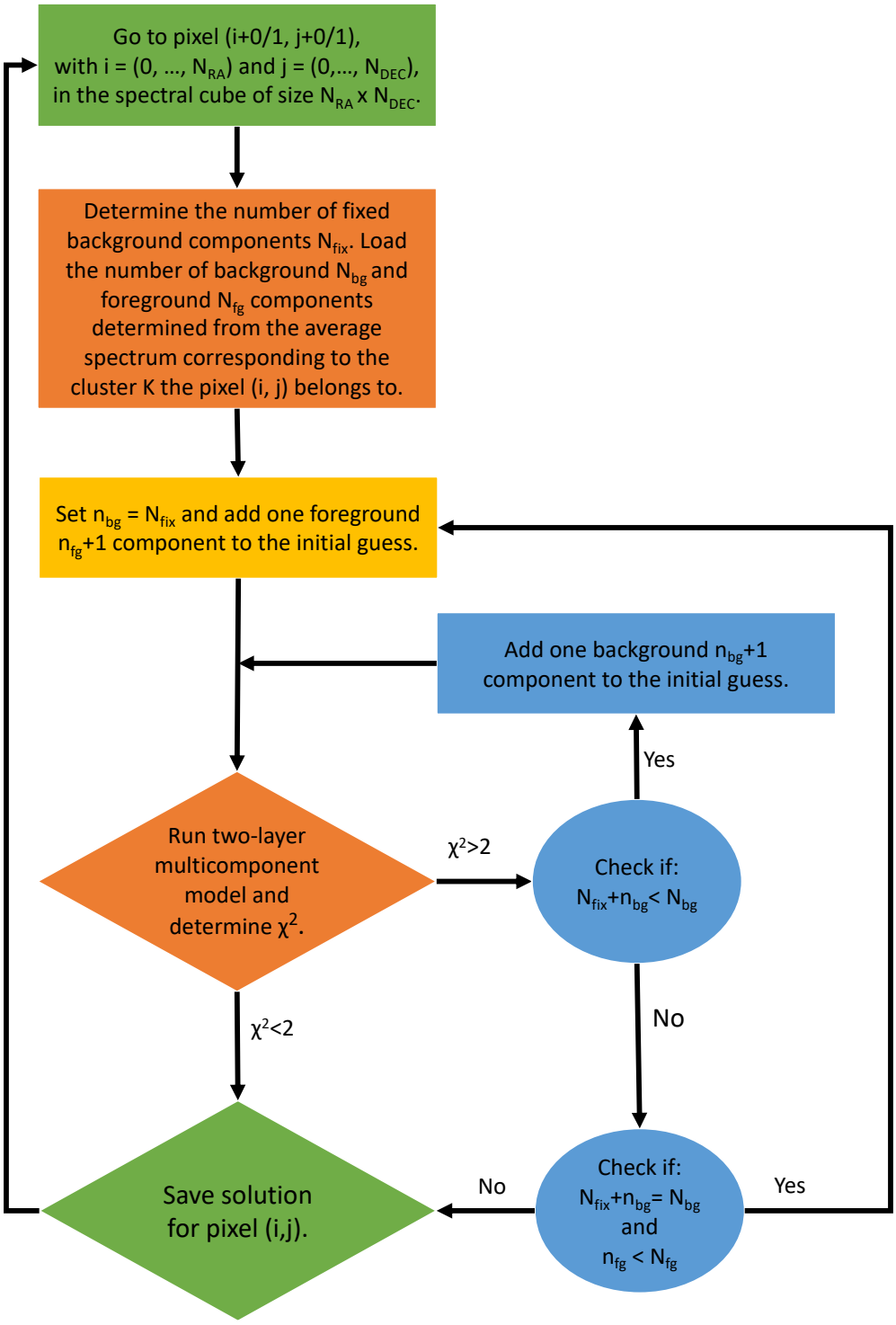

Figure 4.5: Automation of the foreground component fit. Iteratively, additional background wing components and foreground components are added until the desired goodness of the fit or the maximum number of components is reached.

task, however, for an entire data cube that can contain many thousands to millions of spectra, it is not feasible to find proper initial conditions for each spectrum individually in a reasonable amount of time.

To solve this problem, we utilize the fact that the shape of each spectrum in a data cube is not random but confined by the physical conditions of the region. A solution of the radiative transfer equation can be found for spectra originating from regions with similar physical properties with a common initial guess. To find a set of initial conditions which can be used for the entire spectral cube, we first need to sort the spectra into clusters with similar spectral shapes. To do so, we employ the GMM as described in section 4.2.2. First, we determine the necessary number of clusters using the BIC. Subsequently, we cluster the spectral data cube and derive the average spectrum representing each cluster. Finally, we solve the two-layer multicomponent model for each average spectrum of a cluster and use this as an initial guess for all spectra belonging to the cluster.

As described for a single spectrum in section 4.3, we perform two computational steps to determine the single components distributed between the two layers. In the first step, the background emission is determined by fitting each spectrum of the secondary isotope. A schematic description of the automated background layer fit algorithm is shown in Fig. 4.4.

It is essential to take into account that the noise level of the average spectrum might be significantly lower than the noise level of each individual spectrum of the data cube. Therefore, components visible in the averaged spectra might be hidden in the noise floor of the single spectra. Simply using the number of components found from the average rare isotope spectra might result in an over-fitting of the single spectra. Thus, adding components to the model fit not visible in the single spectrum might result in fitting of noise features. Scaling of these noise features by the local abundance ratio between the two observed isotopes will result in artificial background emission. To avoid this, we perform the model fit iteratively, see Fig. 4.4. The fit of each spectral line is started with a single background component. If the reduced χ^2 is close to ~ 1, the algorithm moves to the next spectrum. Otherwise, an additional background component is added until the desired goodness of the fit is achieved or the anticipated number of background components determined from the averaged spectrum is reached.

In the second step, the foreground components are derived fitting the primary isotope affected by the foreground absorption. Therefore, the background components derived from the secondary isotope are scaled up by the local abundance ratio. Similar to the previous step, the fit of the primary isotope is performed iteratively, as shown in Fig. 4.5. In addition, we need to consider here that we observe background components only visible in the stronger primary emission line, which are hidden in the noise of the secondary isotope. To prevent the model from using foreground components to account for emission in the wings of the primary isotope, we first check if the desired

goodness of the fit is reached by including additional background components before including additional foreground components, as shown in Fig. 4.5. The fit is performed in parallel for both isotopes using the relative abundance of the isotopes. This way, we make sure that each component introduced to fit the primary isotope does also fit its corresponding secondary isotope. Again, the model fitting process is performed iteratively until the χ^2 is sufficiently low or the number of background and foreground components determined from the averaged spectrum representing the cluster is reached.

4.4 Moment maps

Spectral data cubes contain two spatial axes spanning the plane of the sky and a third axis containing the radial velocity information. A useful method to analyze spectral data cubes is to determine the momenta along the spectral (velocity) axis.

The 0th order moment is given as the integral over the observed main beam temperature along the velocity axis:

0th moment - integrated intensity

$$M_0 = I = \int T_{\rm mb}(v)\, dv \ , \tag{4.17}$$

which gives the line integrated intensity in units of [K km s^{-1}]. The intensity I can be converted into surface brightness [W m^{-2}sr^{-1}] using equation (2.36):

$$F = 2k_{\rm B} I \left(\frac{\nu}{c}\right)^3 \tag{4.18}$$

The first order moment is determined by calculating the intensity weighted velocity of the spectral line:

1th moment - mean velocity

$$M_1 = \bar{v} = \frac{\int v T_{\rm mb}(v)\, dv}{\int T_{\rm mb}(v)\, dv} = \frac{1}{I} \int v T_{\rm mb}(v)\, dv \ , \tag{4.19}$$

which gives the mean line velocity [km s^{-1}] of the spectrum.

Any moment of higher order ($N \geqslant 2$) can be determined by:

Nth moment

$$M_N = \frac{1}{I} \int T_{\rm mb}\, (v - \bar{v})^N \ dv \ . \tag{4.20}$$

The square root of the 2nd order moment is the variance $\sigma = \sqrt{M_2}$ of the spectrum. Multiplication by the factor $2\sqrt{2\ln 2}$ determines the FWHM of the spectrum. It is important to note that spectra usually contain multiple velocity components, which in addition can originate from multiple (spatially separated) molecular clouds. Thus, moment maps must be calculated in a carefully chosen velocity interval utilizing the velocity information of the spectral data cube. They work best for simple, single Gaussian lines.

4.5 FUV-field

The energetic far ultra-violet (FUV) radiation from massive OB-type stars governs the physical conditions, such as temperature and chemistry of the ISM. Therefore, it is an important input parameter for PDR models to constrain possible solutions. Assuming that the spectral radiance of each star can be approximated by its black-body spectrum, we can derive the radiation field from the temperature and luminosity of the census of stars. To extract the FUV part of the stellar spectrum, the Planck-function, eq (2.17), is integrated between photon energies of 6 eV and 13.6 eV, which corresponds to a wavelength of 910 Å and 2066 Å, respectively:

FUV-Luminosity

$$L_{\mathrm{FUV}} = \frac{\pi \int_{\lambda_{910}}^{\lambda_{2066}} B\left(\lambda, T\right)\, \mathrm{d}\lambda}{\sigma T^4} L \ , \tag{4.21}$$

with the Stefan-Boltzmann constant σ. The UV field is derived in units of the Habing field G_0, which corresponds to $1.6 \cdot 10^{-3}\,\mathrm{erg\,cm^{-2}\,s^{-1}}$. In a second step, the FUV-flux is determined at a chosen position or grid as a superposition of the individual FUV-field contributions of all stars:

$$F_{\mathrm{FUV}} = \sum_{i}^{N_\star} \frac{L_{\mathrm{FUV,i}}}{4\pi R_i^2} \ , \tag{4.22}$$

with R_i the radial distance from the star i and $N_\star$ the number of stars. This approach neglects that some of the FUV-radiation is absorbed or scattered by the surrounding ISM and should therefore be interpreted as an upper limit.

Results

In the following section, the results of a few selected papers, which include the most remarkable results, are presented. I will not present the publications in their entirety but rather focus on my contribution to the publications. To make use of the additional space a thesis format offers, I give additional information or results that were not included in such detail in the published papers.

In section 5.1, I present the results first published by Luisi et al. (2021). Here, I focus on the derivation of the physical properties of the expanding [C II] shell, such as the column density, optical depth, mass, and luminosity. The calculation of these properties was my contribution to the analysis.

In section 5.2, I present my published work as leading author (Kabanovic et al., 2022) in which I performed the data reduction, analysis, and interpretation. In section 5.2.1, I discuss the optical depth effect of ionized and molecular carbon in RCW 120, followed by a more sophisticated analysis using the two-layer model that is described in section 5.2.2. In the next section 5.2.3, the physical conditions of the cold absorbing hydrogen cloud surrounding RCW 120 are determined. Finally, the geometry of RCW 120 is discussed in section 5.2.4.

In the last section 5.3 of this chapter, I present my contribution to the results published by Schneider et al. (2023), discussing [C II] as a tracer of atomic flows, which lead to the formation and mass assembly of molecular clouds in Cygnus X. As co-author, I derived the UV-field of the OB-type cluster in Cygnus, determined the spatial distribution of the [C II]-bright but CO-dark gas, performed an rms analysis to verify the significance of the [C II] tracing the CO-dark gas, and determined the physical properties of the HISA cloud used to characterize the atomic gas.

5.1 RCW 120, a stellar wind-driven bubble

Velocity-resolved spectra allow us to access the gas kinematics and identify the spatial distribution of gas at high velocities as well as at the bulk emission of the cloud. This is illustrated for RCW 120 in the channel maps of the [C II] emission, between -25 and $5\,\mathrm{km\,s^{-1}}$ in steps of $1\,\mathrm{km\,s^{-1}}$, shown in Fig. 5.1. Around the systemic velocity of

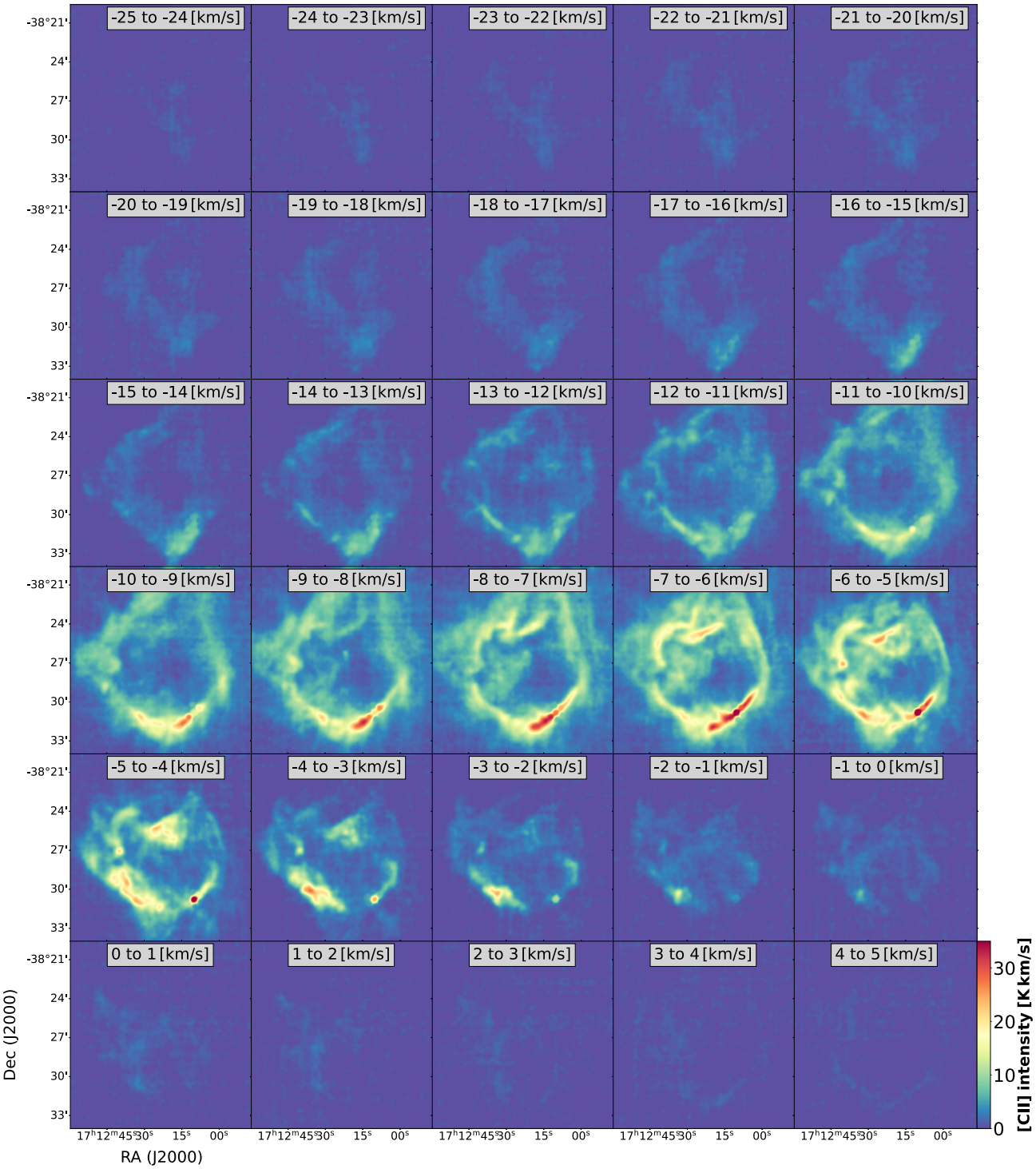

Figure 5.1: Velocity resolved [C II] emission from RCW 120. The channel maps show the velocity range between -25 and 5 $\mathrm{km\,s^{-1}}$ integrated over 1 $\mathrm{km\,s^{-1}}$. The systemic velocity of RCW 120 is $-7.5\,\mathrm{km\,s^{-1}}$.

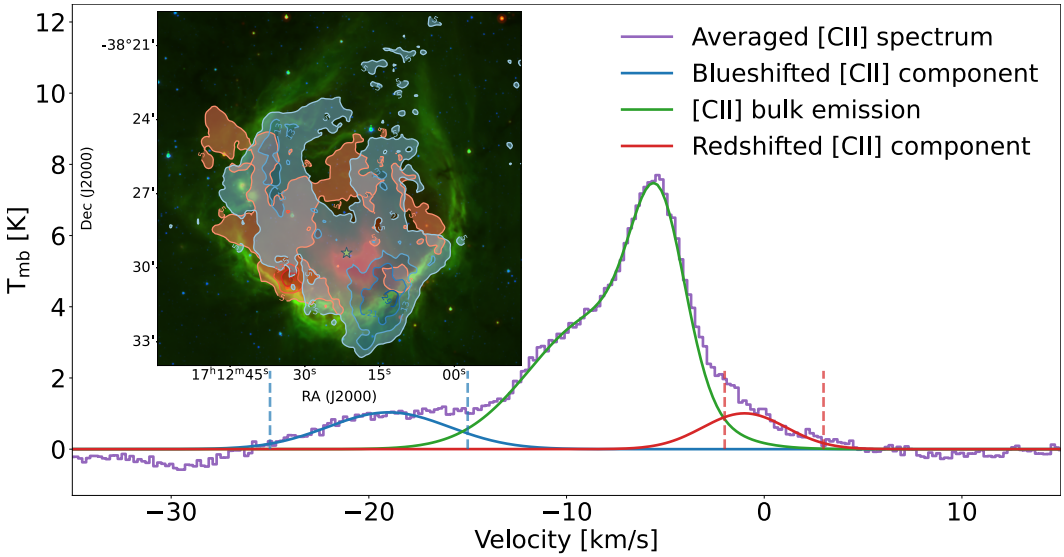

Figure 5.2: [C II] emission averaged over the interior of the ring in RCW 120. The purple data shows the averaged [C II] spectrum. The green component centered at the systemic velocity of RCW 120 indicates the bulk emission from the molecular cloud. The blue and red Gaussian components show the high-velocity emission originating from the two hemispheres of the expanding bubble. The blue and red dashed lines indicate the integral ranges of [-25, -15] km s^{-1} for the blueshifted and [-2, 3] km s^{-1} for the redshifted emission. The upper left corner shows the Spitzer false color image of RCW 120. The hot emitting dust is shown in red, the warm gas is green, and the stars are indicated in blue. The blue- and red-filled contours show the [C II] emission from the blue- and redshifted expanding bubble, respectively.

$-7.5\,\mathrm{km\,s^{-1}}$, we see the characteristic ring-like structure of RCW 120. This emission mainly originates from the PDR surfaces surrounding the H II region. Going to higher velocities, i.e., redshifted with respect to the systemic velocity of RCW 120, the emission moves from the ring towards its interior, as one would expect from an expanding H II region. However, at even higher velocities $> 3\,\mathrm{km\,s^{-1}}$, we observe again emission originating from the ring. This can be attributed to the hyperfine transition of the [^{13}C II] F(2 → 1) line, which is located close to the redshifted wing of the primary isotope. For the blueshifted velocity bins, we observe a similar scenario. The emission also moves toward the center, tracing the hemisphere of the expanding blueshifted bubble.

The three observed components shown in the channel maps in Fig. 5.1 are also seen in the averaged spectrum toward the ring's interior of RCW 120 shown by the purple spectrum in Fig. 5.2. The bulk [C II] emission is shown as the green component centered around the systemic velocity of RCW 120. The blue and red Gaussian components indicate the [C II] emission from the two expanding shell hemispheres. While the blueshifted component is clearly separated from the bulk emission, the redshifted

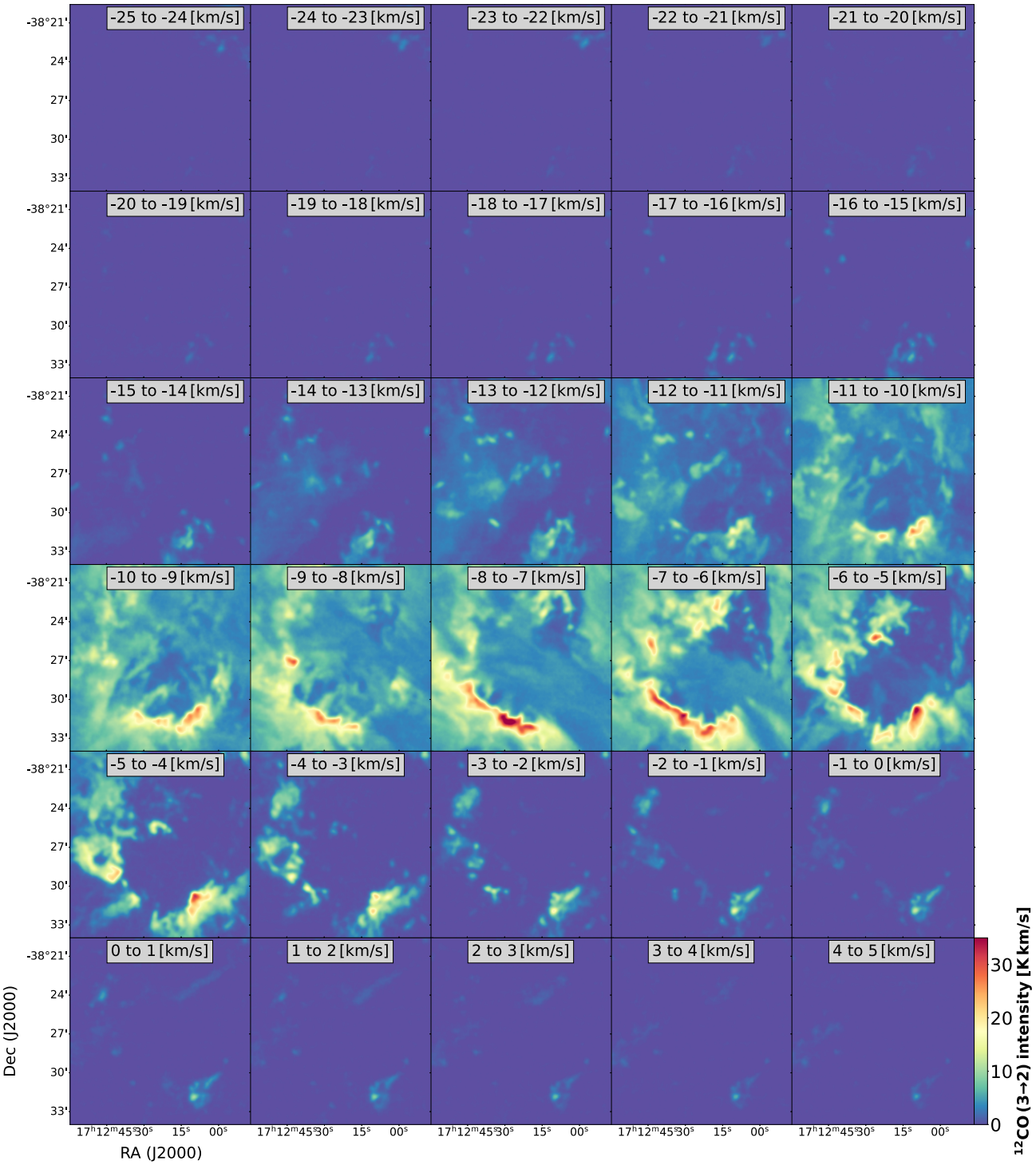

Figure 5.3: Velocity resolved ^{12}CO ($3 \rightarrow 2$) emission from RCW 120. The channel maps show the velocity range between -25 and 5 km s^{-1} integrated over 1 km s^{-1}. The systemic velocity of RCW 120 is -7.5 km s^{-1}.

part is found at lower velocities with respect to the systemic velocity, merging with the bulk emission. The corresponding [C II] shell emission, integrated over [-25, -15] km s^{-1} for the blueshifted component and [-2, 3] km s^{-1} for the redshifted component (integral ranges are also indicated by the dashed vertical lines), are shown in the sub-panel in Fig. 5.2. The emission from the blueshifted shell fills most of the interior, indicated by the blue filled contours. In contrast, the redshifted emission is rather fragmented, as shown by red filled contours. This indicates that the blueshifted shell expands more freely while the redshifted hemisphere is probably slowed down by the surrounding material toward the back of the cavity.

The velocity-resolved emission from the molecular carbon monoxide line ^{12}CO J(3 → 2) is shown in Fig. 5.3. In contrast to the [C II] emission, we do not find the ring-like structure at the systemic velocity but rather a U-shaped clumpy distribution with an opening toward the northwest. We observe strong self-absorption effects around the bulk emission, which extends diagonally from the southwest to the northeast through the center of RCW 120. Going to higher velocities, the CO emission does not shift as observed for the [C II] line toward the center but rather keeps emitting from various locations along the PDR surrounding the bubble. Many of them indicate outflow features originating from the dense clumps. The most prominent outflow is observed toward the southwest clump, referred to as condensation 1 in (Zavagno et al., 2007) and contains a protostellar CO outflow which was analyzed first by Figueira et al. (2020). At lower, blueshifted velocities, we also observe the outflow features and some diffuse CO emission but again no clear sign of an expanding bubble traced by CO.

The velocity-resolved spatial distribution of the ^{13}CO J(3 → 2) isotope is shown in Fig. 5.4. Similar to the primary isotope, we observe the U-shaped dense molecular cloud. Instead of the prominent optical depth effects, we observe two lanes spanning the central region of RCW 120 visible at the systemic velocity −8 to −7 km s^{-1}. These lanes are, in particular, visible in Hα absorption (Zavagno et al., 2007) and thus must be placed in front of the H II region.

To further analyze the kinematics of RCW 120, we utilize the velocity information of our three tracers again and generate position velocity diagrams through the horizontal symmetry axis of the H II region indicated by the dashed purple horizontal line in Fig. 3.7. The spectral data were convolved to a beam of 1 arcmin to increase the S/N. The resulting position-velocity diagrams for the [C II], ^{12}CO, and ^{13}CO (3 → 2) emission are shown in Fig. 5.5. The bulk of the [C II] emission is found at the systemic velocity of RCW 120, see Fig. 5.5a, which is indicated by the dashed horizontal line. However, in addition, we clearly observe an arc-like structure in the blueshifted part of the diagram, which is indicated by the black curve assuming an expansion speed of 15 km s^{-1} (Luisi et al., 2021). This arc-like structure in (radial) velocity space is characteristic of an expanding bubble (Pabst et al., 2019). In the redshifted part of the diagram, we also observe emission at higher velocities. However, no arc-like structure

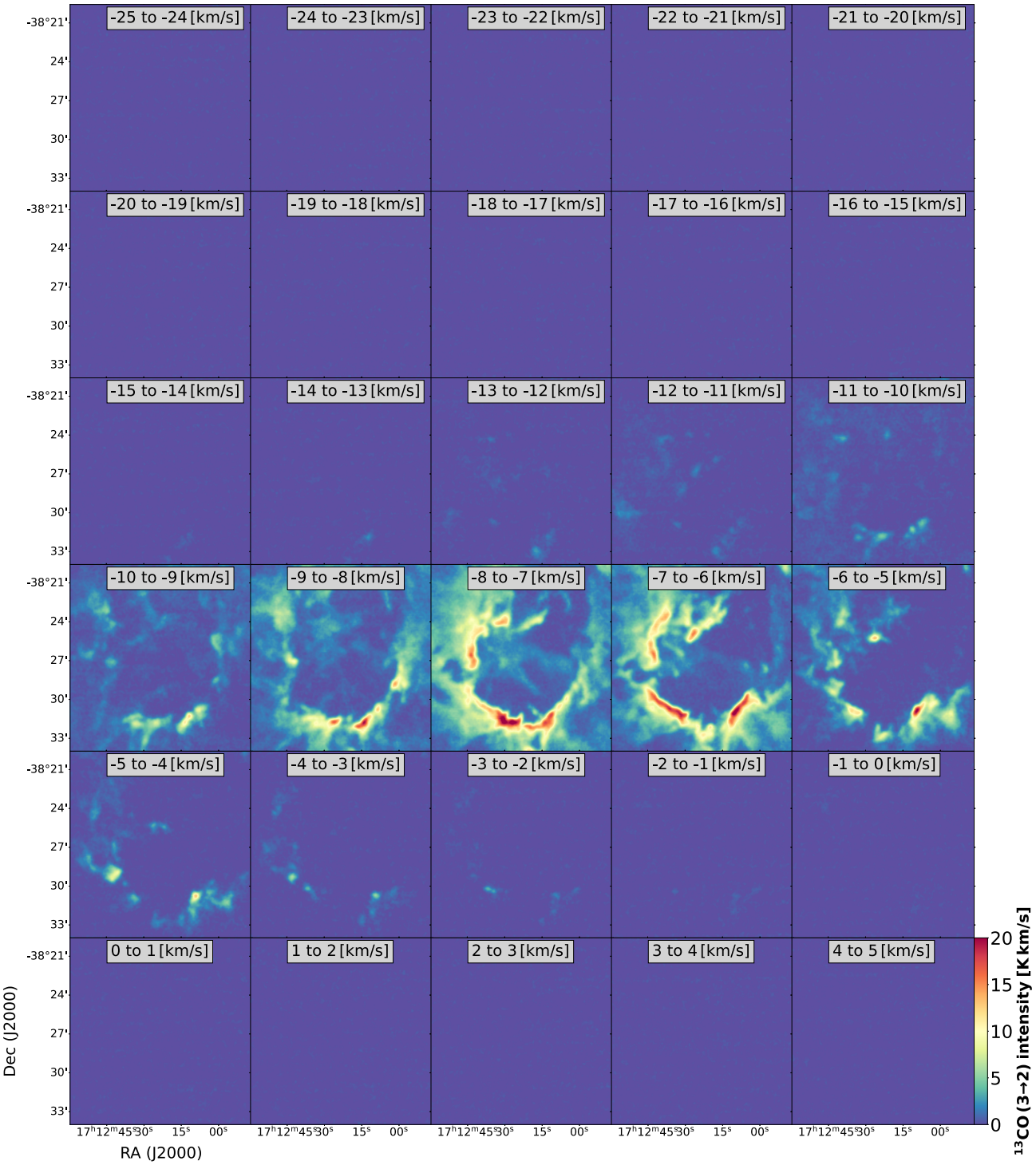

Figure 5.4: Velocity-resolved ^{13}CO ($3 \rightarrow 2$) emission from RCW 120. The channel maps show the velocity range between -25 and 5 km s^{-1} integrated over 1 km s^{-1}. The systemic velocity of RCW 120 is -7.5 km s^{-1}.

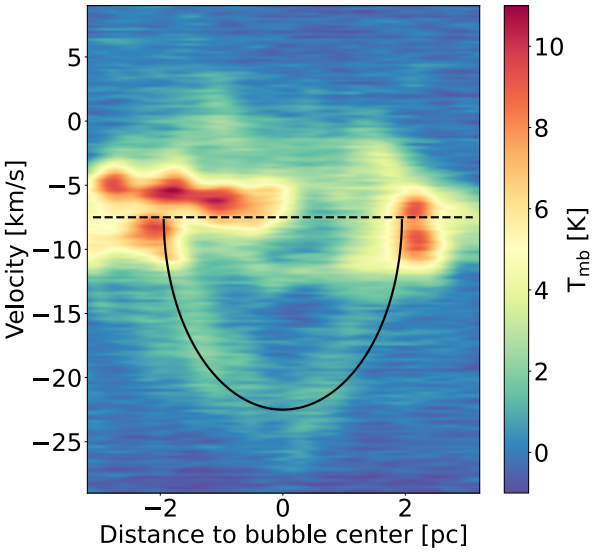

(a) [C II] emission.

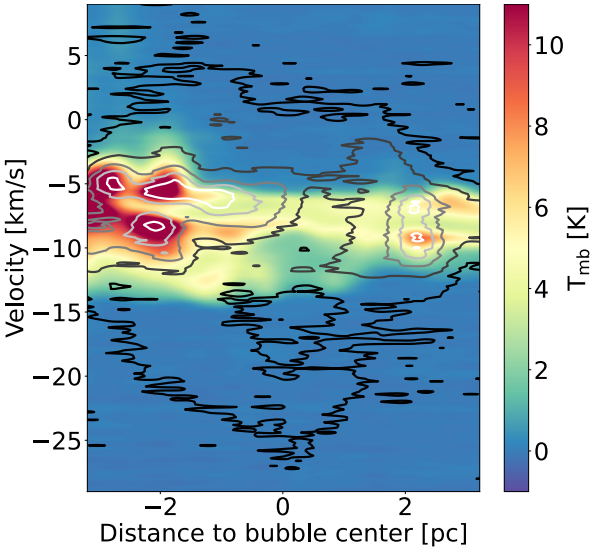

(b) ^{12}CO ($3 \rightarrow 2$) emission.

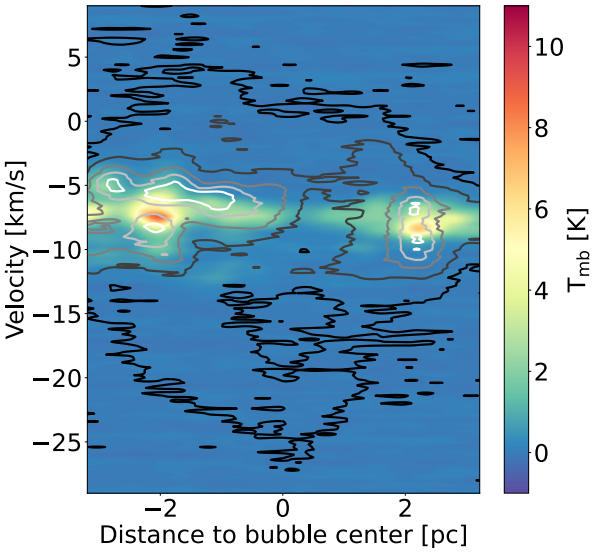

(c) ^{13}CO ($3 \rightarrow 2$) emission.

Figure 5.5: Position-velocity cuts through the bubble center of RCW 120 for [C II], ^{12}CO, and ^{13}CO ($3 \rightarrow 2$) emission. The data were convolved to a beam of $1'$. (a) [C II] PV cut along the horizontal symmetry axis of the H II region. The dashed horizontal line indicates the systemic velocity at $-7.5\,\mathrm{km\,s^{-1}}$. The black solid arc indicates the blueshifted [C II] component, which traces the expanding bubble. (b) and (c) show the ^{12}CO and ^{13}CO ($3 \rightarrow 2$) PV cuts, respectively. The contours indicate the [C II] emission in intensity levels of 0.5, 2.5, 5, 7, $9\,\mathrm{km\,s^{-1}}$ from black to white.

is visible since the redshifted hemisphere is expanding with a somewhat lower velocity of $10\,\mathrm{km\,s^{-1}}$, and its emission is contaminated by the bulk emission of the molecular cloud. The position velocity diagrams of the ^{12}CO and ^{13}CO ($3 \rightarrow 2$) lines are shown in Fig. 5.5b and 5.5c. The [C II] emission is overlaid with contours for comparison. In contrast to the [C II] emission, we only observe CO emission around the systemic velocity. Thus, there is no molecular counterpart found at velocities of the [C II] shell. This implies that the PDR region is indeed located beyond the expanding [C II] shell (Luisi et al., 2021).

Assuming that the expanding [C II] shell is optically thin and has an excitation temperature of $T_{\mathrm{ex}} \sim 100\,\mathrm{K}$, I derive the corresponding C^+ column density from the integrated intensity and subsequently the total hydrogen mass of the expanding shell:

$$m_{\mathrm{H,shell}} = \frac{N_{[\mathrm{C\,II}]}}{1.6 \cdot 10^{-4}} m_{\mathrm{H}} A_{\mathrm{shell}} \ , \tag{5.1}$$

with the hydrogen to carbon ratio of $\mathrm{C/H} = 1.6 \cdot 10^{-4}$ (Sofia et al., 2004), the hydrogen mass m_{H} and the spatial extent of the shell A_{shell}. The radial velocity of the two expanding hemispheres is largest toward the center of the bubble and decreases toward the edges until the radial velocity components merge into the systemic velocity of the cloud. Thus, at the edges of the bubble, it is not possible to disentangle the PDR emission from the emission originating from the expanding shell. I, therefore, determine a mass range for the expanding shell. For the lower limit, I only take the emission from the interior, where I can separate the emission of the expanding bubble from the bulk emission. For the upper limit of the shell mass, I also include the emission from the ring, with some contribution from the PDR surrounding the shell. In this way, the mass of the expanding shell is confined to $40 - 400\,\mathrm{M_\odot}$. Correcting for the optically thick emission in the three PDRs along the ring results in a somewhat higher upper limit of $\sim 520\,\mathrm{M_\odot}$ as derived in Luisi et al. (2021). A more in-depth analysis of the optical depth effects in the PDRs, and the derivation of its physical properties are presented in the following sections 5.2.1-5.2.4. However, I assume that the dense optically thick emission from the PDRs is not part of the expanding shell and, therefore, would lead to an overestimation of the shell mass. Knowing the velocity and mass of the shell, we can now determine its kinetic energy:

$$E_{\mathrm{kin,shell}} = \frac{1}{2} M_{\mathrm{H,shell}} v_{\mathrm{shell}}^2 = [10, 100] \times 10^{46}\,\mathrm{erg} \ , \tag{5.2}$$

and its thermal energy:

$$E_{\mathrm{th,shell}} = \frac{3}{2} k_{\mathrm{B}} T_{\mathrm{H,shell}} \frac{M_{\mathrm{H,shell}}}{m_{\mathrm{H}}} = \ [0.1, 1] \times 10^{46}\,\mathrm{erg}. \tag{5.3}$$

We find that the kinetic energy inside the expanding shell is two orders of magnitude larger than the thermal energy of the shell. Comparing the kinetic energy of the expanding bubble to the mechanical luminosity of the stellar wind over the age of

the bubble ($150 \cdot 10^{46}$ erg, Luisi et al. (2021)) suggests that the stellar wind energy is converted very efficiently into the mechanical energy of the surrounding medium.

5.2 Self-absorption in [CII], CO, and HI

5.2.1 [CII] and CO optical depth in RCW 120

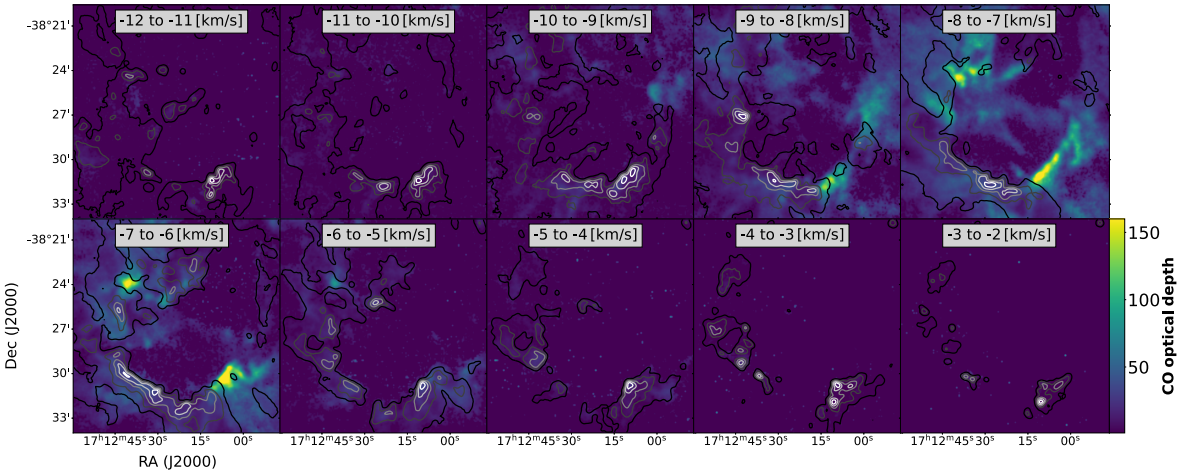

Figure 5.6: Velocity resolved CO optical depth in RCW 120. The contours show the corresponding ^{12}CO(3→2) emission.

As already mentioned in the previous section 5.1, we observe self-absorption features in the ^{12}CO (3→2) at the systemic velocity of RCW 120, as shown in Fig. 5.3. Optical depth effects may obscure the spectral shape and the observed spatial intensity distribution. To quantify the self-absorption in CO, I derive the optical depth with equation (2.74), which compares the intensity of both isotopes to the expected local carbon ratio. I derived the carbon abundance ratio of $\alpha = 59 \pm 10$ using equation (2.81).

The resulting velocity resolved CO optical depth is shown in Fig. 5.6. It is striking that the optical depth effects around the systemic velocity of RCW 120 ($\sim -7.5\,\mathrm{km\,s^{-1}}$) are strongest at the south-western and north-eastern PDRs which are connected by the dark lanes spanning through the center of RCW 120. The optical depth does not correlate well with the observed ^{12}CO emission, as shown by the contours. This already indicates that the derived optical depth is due to foreground absorption. At redshifted velocities, we find a sudden morphological change in the spatial distribution of the optical depth, which reaches high values only close to the U-shaped molecular envelope.

To quantify the optical depth of the [CII] line, we can derive the ratio between the [^{12}CII] line to the average of the three hyperfine [^{13}CII] transition lines. However, the intensity of the [^{13}CII] transition lines is not strong enough to have a pixel-by-pixel

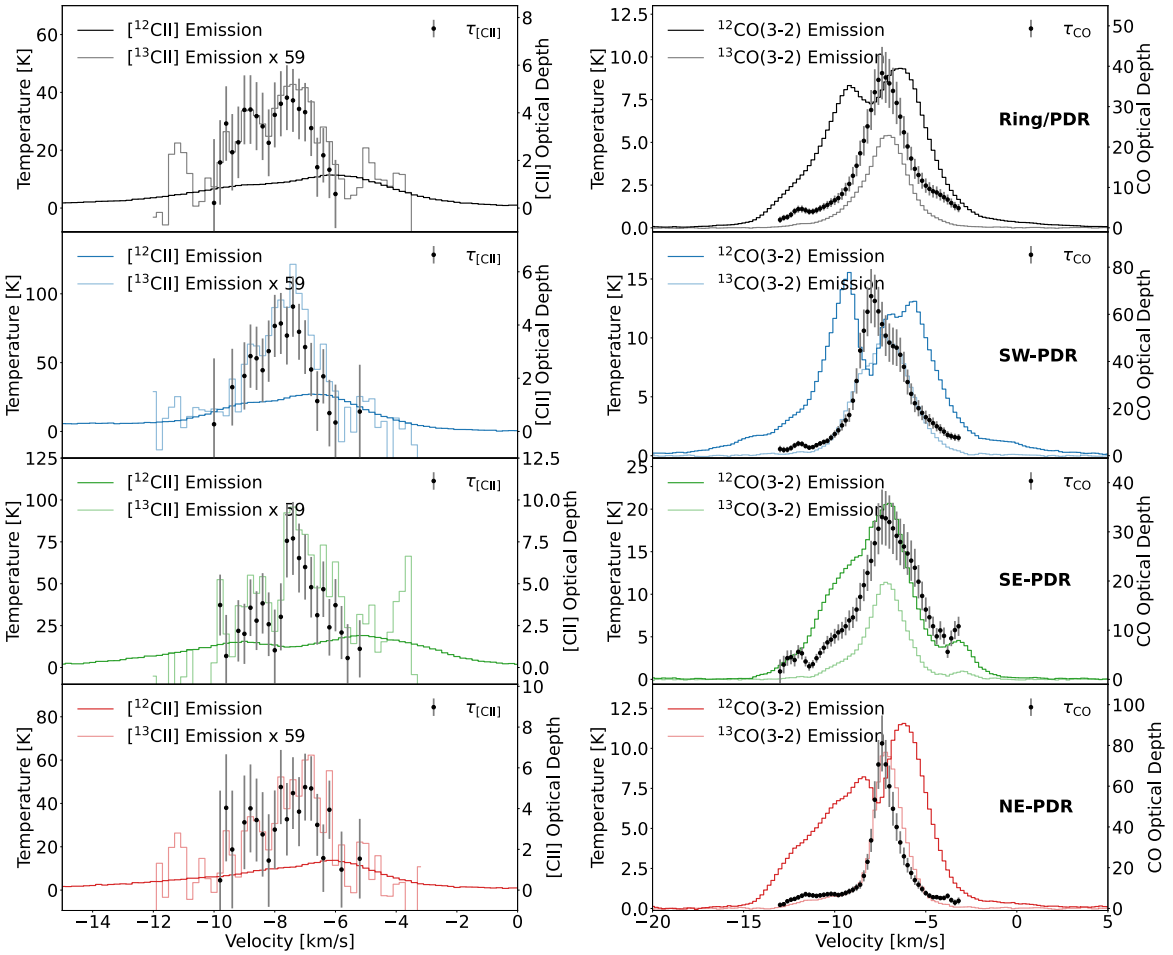

(a) [C II] average spectra. **(b)** CO average spectra.

Figure 5.7: Velocity resolved [C II] and CO ($3 \rightarrow 2$) optical depth (Kabanovic et al., 2022). The spectra are averaged over the entire ring (black), the south-western PDR (blue), the south-eastern PDR (green), and the north-eastern PDR (red). The corresponding regions are indicated by the colored contours in Fig. 3.7a. The light-colored spectra represent the emission from the secondary isotope [^{13}C II] or ^{13}CO. The [^{13}C II] emission, which is shown in the left panels (a), is averaged over all three hyperfine transition lines and scaled up by the local abundance ratio ^{12}C/^{13}C = 59. The black data points with error bars show the optical depth derived from the intensity ratio between the two isotopes.

detection. Thus, to disentangle its emission from the noise floor, I average the observed emission over several arcmin^2 sized regions along the PDR. I use a dendrogram-based approach described in section 4.2.1. The four resulting clusters, which include the entire PDR/ring, the south-western, south-eastern and north-eastern PDR, are represented in Fig. 3.7a by the black, blue, green, and red contours, respectively.

The corresponding averaged spectra along the ring in [C II] and CO (3 → 2) are shown in Fig. 5.7. The spectra shown in the light colors represent the emission from the secondary isotopes [^{13}C II] and ^{13}CO (3 → 2). The three [^{13}C II] hyperfine transition lines are averaged and scaled by the local carbon abundance ratio of $\alpha = 59$. We find that the scaled [^{13}C II] line overshoots its primary isotope [^{12}C II] and peaks where the [^{12}C II] line has a dip in emission, as shown in the left panels in Fig. 5.7. This suggests that the dip, located at the systemic velocity of RCW 120, is due to absorption by a colder [C II] foreground. The black data points with error bars show the optical depth derived from the intensity ratio of the two isotopes. The determined [C II] optical depth around the systemic velocity is always significantly above one.

The calculated intensity difference between ^{12}CO and ^{13}CO also results in high optical depth values. We observe the absorption dip in the primary isotope ^{12}CO to be blueshifted with respect to the emission peak of the ^{13}CO line. This might be due to the bubble expansion, which pushes the cold foreground medium toward the observer, resulting in a blueshifted absorption dip. Moreover, we also observe an asymmetry in the optical depth between the two wings of the CO spectra. Thus, the redshifted wings show significantly higher optical depth values than the blueshifted ones. These higher optical depth values in the redshifted wing and the sudden morphological change in the spatial optical depth distribution shown in Fig. 5.6 might be an indication of gas inflow. We will discuss the possible inflow in more detail later on, see also Kabanovic et al. (2022).

The very large optical depth values and the absorption dips in the observed spectra already apparent from the above relatively simple analysis suggest that we need a more sophisticated model that properly takes absorption effects by a colder foreground into account. Thus, in the following, we will revisit our optical depth analysis utilizing the two-layer multicomponent model (Guevara et al., 2020; Kabanovic et al., 2022).

5.2.2 [C II] self-absorption in RCW 120

The [C II] 158 μm line is one of the most important cooling lines of the ISM (Tielens and Hollenbach, 1985). Therefore, it seems natural that [C II] emission can originate from a variety of physical conditions such as a hot expanding H II region or warm PDR surfaces as discussed in section 5.1 and by Luisi et al. (2021). However, the previous optical depth analysis additionally suggests a cold absorbing [C II] component. To disentangle the warm emitting layer from the cold absorbing layer, I solve the radiative transfer equation allowing multiple components distributed between two layers as described by equation (4.13).

We first need to constrain the background and foreground excitation temperature to solve the two-layer multicomponent model. A lower limit for the background temperature can be derived with equation (4.16) assuming the peak emission of the primary isotope is not strongly affected by foreground absorption and thus can partly shine

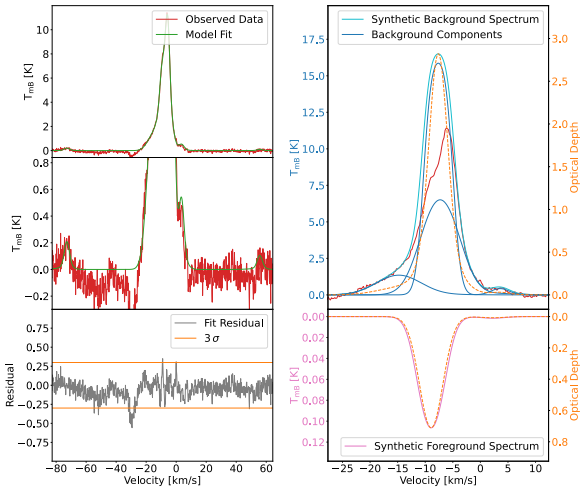

(a) $T_{\mathrm{ex,fg}} = 15\,\mathrm{K}$, RCW 120 PDR/ring.

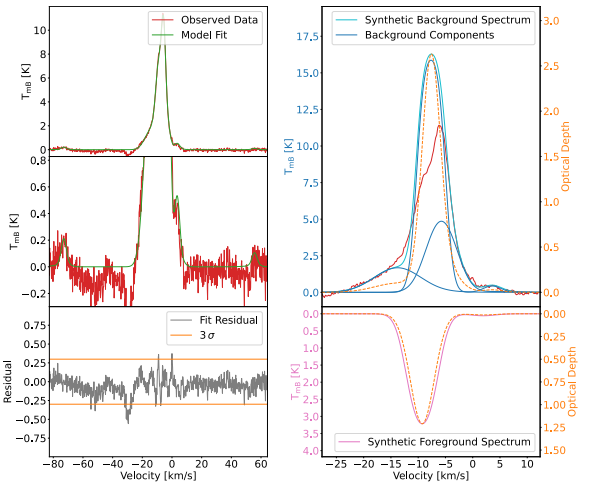

(b) $T_{\mathrm{ex,fg}} = 30\,\mathrm{K}$, RCW 120 PDR/ring.

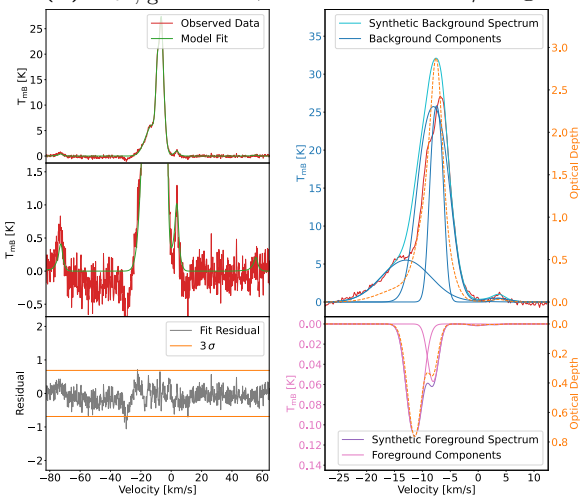

(c) $T_{\mathrm{ex,fg}} = 15\,\mathrm{K}$, Southwestern PDR.

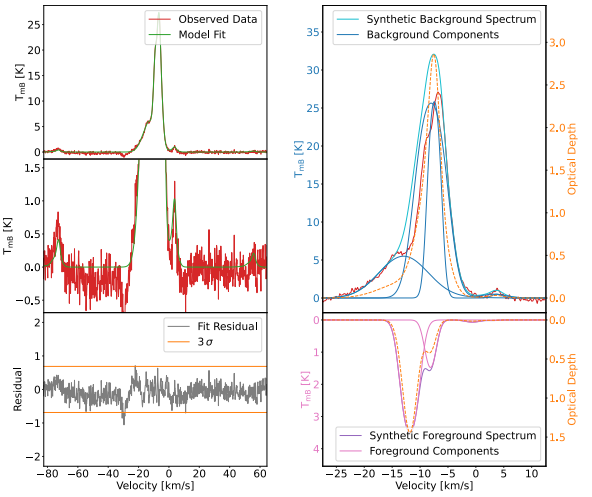

(d) $T_{\mathrm{ex,fg}} = 30\,\mathrm{K}$, Southwestern PDR.

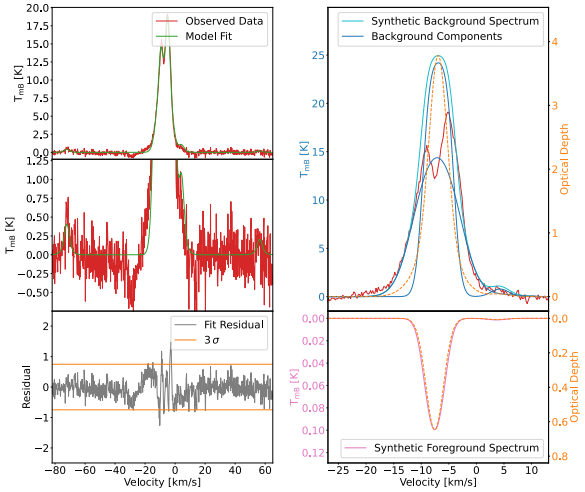

(e) $T_{\mathrm{ex,fg}} = 15\,\mathrm{K}$, Southeastern PDR.

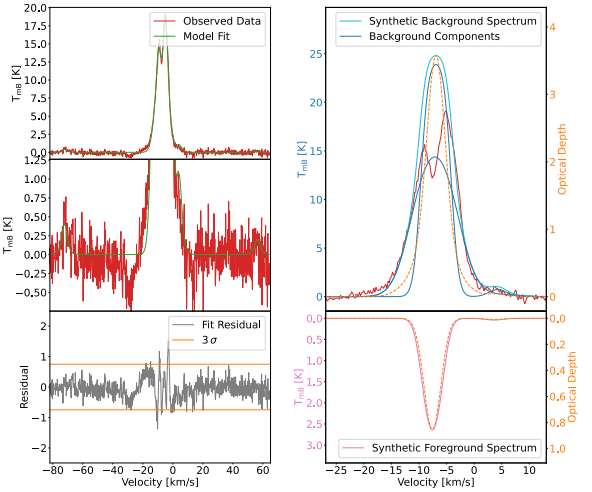

(f) $T_{\mathrm{ex,fg}} = 30\,\mathrm{K}$, Southeastern PDR.

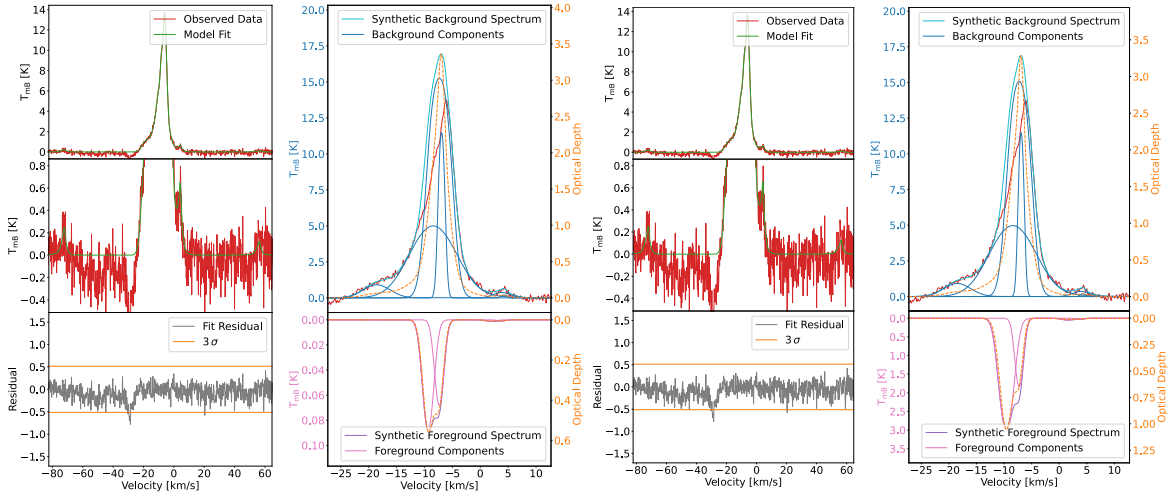

(g) $T_{\mathrm{ex,fg}} = 15\,\mathrm{K}$, Northeastern PDR. **(h)** $T_{\mathrm{ex,fg}} = 30\,\mathrm{K}$, Northeastern PDR.

Figure 5.8: [C II] two-layer multicomponent model solution for (a)-(b) the PDR/ring in RCW 120, (c)-(d) the southwestern PDR, (e)-(f) southeastern PDR, and (g)-(f) the northeastern PDR (Kabanovic et al., 2022). The two-layer model solution for a foreground excitation temperature of $T_{\mathrm{ex,fg}} = 15\,\mathrm{K}$ is shown in the left panels and for $T_{\mathrm{ex,fg}} = 30\,\mathrm{K}$ in the right panels. Left upper sub-panel: The observed data are shown by the red data points, and the green curve shows the model fit. Left middle sub-panel: same as left upper sub-panel but the intensity axis is cut at lower temperatures to better visualize the three hyperfine transition lines. Left lower sub-panel: The grey data points show the fit residuals and the two orange horizontal axes show the 3σ detection level. Right upper sub-panel: the blue Gaussians show the single background components. The cyan curve is the superposition of all the background components. The dashed orange curve shows the velocity resolved background optical depth. Right lower sub-panel: The pink Gaussians show the single foreground components. The purple curve is the superposition of all the foreground components. The dashed orange curve indicates the velocity resolved foreground optical depth.

through to the observer, see Fig. 4.3 for example. We can use the optical depth derived from the intensity ratio between the two isotopes with equation (2.74). This gives us temperatures of 50-70 K along the ring emission in RCW 120, where we find the strongest [C II] lines.

The absence of strong absorption dips in the [^{12}C II] spectra requires us to use an alternate approach to constrain the foreground temperature rather than simply deriving the temperature from the absorption dip minimum. A lower limit for [C II] excitation temperature can be derived from the energy balance between the [C II] cooling and heating by cosmic ray ionization and the standard interstellar radiation field.

Table 5.1: Averaged [C II] physical properties of the emitting and absorbing layers along the ring of RCW 120. A lower limit of 15 K and an upper limit of 30 K was used for the foreground excitation temperature. The table is adapted from Kabanovic et al. (2022).

		Background				
Region	(1) A [pc^2]	(2) $\tau_{[\mathrm{C\,II}]}$	(3) $N_{[\mathrm{C\,II}]}$ [10^{18} cm^{-2}]	(4) N_{H} [10^{21} cm^{-2}]	(5) M_{H} [$M_\odot$]	(6) $L_{[\mathrm{C\,II}]}$ [$L_\odot$]
Ring	12.9	2.8	3.1	19.6	2018	357.3
SW PDR	0.6	2.9	3.9	24.1	118	31.9
SE PDR	0.5	3.8	4.9	30.7	114	21.1
NE PDR	1.5	3.4	2.8	17.7	212	38.1
$T_{ex,fg}$ = 15 K		**Foreground**				
Ring	12.9	0.7	0.5	3.3	344	1.77
SW PDR	0.6	0.8	0.4	2.8	14	0.07
SE PDR	0.5	0.6	0.4	2.3	8	0.04
NE PDR	1.5	0.6	0.3	1.8	21	0.11
		Background				
Ring	12.9	2.6	2.8	17.6	1818	333.2
SW PDR	0.6	2.9	3.8	23.9	118	31.8
SE PDR	0.5	3.6	4.7	29.3	109	20.9
NE PDR	1.5	3.3	2.7	17.0	203	37.5
$T_{ex,fg}$ = 30 K		**Foreground**				
Ring	12.9	1.2	1.1	6.6	685	58.5
SW PDR	0.6	1.4	0.9	5.7	28	2.34
SE PDR	0.5	0.9	0.5	3.3	12	1.16
NE PDR	1.5	1.1	0.6	3.9	47	4.19

(1) The area of the regions, defined by Dendrograms (Rosolowsky et al., 2008; Robitaille et al., 2019).

(2) [C II] peak optical depth.

(3) [C II] column density (eq. 2.63).

(4) Hydrogen column density $\mathrm{N_H} = \mathrm{N_{H\,I}} + 2\mathrm{N_{H_2}}$, using $\mathrm{C/H} = 1.6 \cdot 10^{-4}$ (Sofia et al., 2004).

(5) Mass from hydrogen column density.

(6) Luminosity for the background and foreground layers.

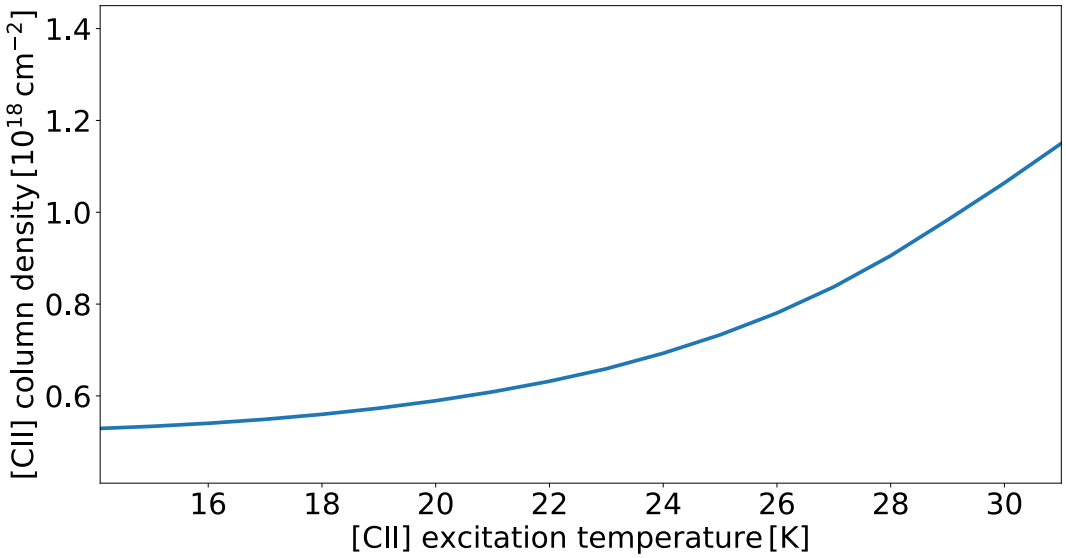

Figure 5.9: Foreground [C II] column density as a function of excitation temperature (Kabanovic et al., 2022). The column density is determined from the averaged [C II] spectrum of the entire PDR/ring in RCW 120 by applying the two-layer multicomponent model for the possible range of foreground excitation temperatures between 15 and 30 K.

The emissivity of diffuse optically thin [C II] gas can be expressed as (Ossenkopf et al., 2013):

$$\begin{aligned}\int \epsilon \,\mathrm{d}v &= \frac{hA_{ul}c^3}{8\pi k_\mathrm{B}\nu^2} \times N_{[\mathrm{C\,II}]} \times \frac{g_u e^{\frac{-T_0}{T_\mathrm{ex}}}}{g_l + g_u e^{\frac{-T_0}{T_\mathrm{ex}}}} \\ &= 2.3 \cdot 10^{-28} \frac{\mathrm{W}}{\mathrm{sr}} \times N_{[\mathrm{C\,II}]} \times E(T_\mathrm{ex}) \ ,\end{aligned} \tag{5.4}$$

with the heating efficiency ϵ and the excitation temperature term expressed as $E(T_\mathrm{ex})$. We can now write the total [C II] cooling as:

$$\Lambda_{[\mathrm{C\,II}]} = \int_{4\pi}\int \epsilon \,\mathrm{d}v \,\mathrm{d}\Omega = 2.9 \cdot 10^{-27}\,\mathrm{W} \times N_{[\mathrm{C\,II}]} \times E(T_\mathrm{ex}) \ . \tag{5.5}$$

We assume that the cold diffuse foreground cloud is heated by the ambient UV-field and through cosmic ray (CR) ionization. The energy density ϱ_UV for a UV field of $\chi = 1$ is $6.8 \cdot 10^{-21}\,\mathrm{J/cm^3}$. The Habing field G_0 can be related to the Draine field χ by $\chi = 1.71\,G_0$, where G_0 is the mean interstellar radiation field from Habing (1968); Draine (1978). The UV radiation is mainly absorbed by interstellar dust, which results in a UV optical depth of $\tau_\mathrm{UV} \sim 3A_\mathrm{v}/1.08$. The heating of the dust and gas in a column of $A_\mathrm{v} = 1$ can be written as:

$$F_\mathrm{UV} = \left(1 - e^{-\tau_{\mathrm{UV}(A_\mathrm{v}=1)}}\right) \varrho_{\mathrm{UV},\chi=1} c = 1.9 \cdot 10^{-6} \frac{\mathrm{W}}{\mathrm{m}^2} \ . \tag{5.6}$$

We assume a typical gas heating efficiency of $\varepsilon = 0.01$ (Okada et al., 2013). The gas column density is $N_{\mathrm{H},A_\mathrm{v}=1} = 1.9 \cdot 10^{21}\,\mathrm{cm}^{-2}$. With this, we can now write the heating rate per hydrogen; and with the carbon to hydrogen ratio C/H $= 1.6 \cdot 10^{-4}$ (Sofia et al., 2004) we obtain a [C II] heating rate of:

$$\Gamma_\mathrm{UV} = \varepsilon \frac{F_\mathrm{UV}}{N_{\mathrm{H},A_\mathrm{v}=1} \times \mathrm{C/H}} \times N_\mathrm{[C\,II]} = 6.3 \cdot 10^{-30}\,\mathrm{W} \times N_\mathrm{[C\,II]}\ . \tag{5.7}$$

The heating rate from the cosmic rays is expressed as the CR heating energy per ionization $Q \sim 10\,\mathrm{eV}$ (Glassgold et al., 2012) times the CR ionization rate of $\eta_\mathrm{H} \approx 2 \cdot 10^{-16}\,\mathrm{s}^{-1}$ (Indriolo et al., 2015). Dividing by the C/H-ratio gives the CR [C II] heating rate:

$$\Gamma_\mathrm{CR} = \frac{Q \times \eta_\mathrm{H}}{\mathrm{C/H}} \times N_\mathrm{[C\,II]} = 2 \cdot 10^{-30}\,\mathrm{W} \times N_\mathrm{[C\,II]}\ . \tag{5.8}$$

The sum of equation (5.7) and (5.8) gives us the total heating rate of the diffuse [C II] gas:

$$\Gamma_\mathrm{[C\,II]} = \Gamma_\mathrm{UV} + \Gamma_\mathrm{CR} = 8.3 \cdot 10^{-30}\mathrm{W} \times N_\mathrm{[C\,II]}\ . \tag{5.9}$$

The energy balance between the total cooling rate, equation 5.5, and the total heating rate, equation 5.9 gives us the lower limit [C II] excitation temperature for a low ambient radiation field:

Lower limit [C II] excitation temperature

$$\begin{aligned} E(T_\mathrm{ex}) = 0.003 &= \frac{g_u e^{\frac{-T_0}{T_\mathrm{ex}}}}{g_l + g_u e^{\frac{-T_0}{T_\mathrm{ex}}}} \\ \Rightarrow T_\mathrm{ex} &= \frac{T_0}{\ln\left(\frac{2}{E} - 2\right)} = 14\,\mathrm{K}\ . \end{aligned} \tag{5.10}$$

Since [C II] is the main cooling line of the diffuse medium, the gas cannot get any colder than the derived $T_\mathrm{ex} = 14\,\mathrm{K}$. We note that the chosen CR ionization rate is solely a lower limit. However, assuming an ionization rate that is an order of magnitude larger increases the [C II] excitation temperature to $T_\mathrm{ex} \sim 17\,\mathrm{K}$, see Fig. 5.10. Thus, for simplicity, we set the lower limit to $T_\mathrm{ex} \sim 15\,\mathrm{K}$.

We can find an upper limit for the foreground excitation temperature using an independent estimate of the hydrogen column density. Zavagno et al. (2007) derived a visual extinction of $\mathrm{A_v} \sim 4.36$ towards the H II region. This results in a hydrogen column density of $8.15 \cdot 10^{21}\,\mathrm{cm}^{-2}$, which translates into a C^+ column density of $1.3 \cdot 10^{18}\,\mathrm{cm}^{-2}$. Fig. 5.9 shows the two-layer multicomponent model results of the cold foreground column density as a function of temperature. The upper limit of the [C II] column density is approximately reached at $T_\mathrm{ex} \sim 30\,\mathrm{K}$.

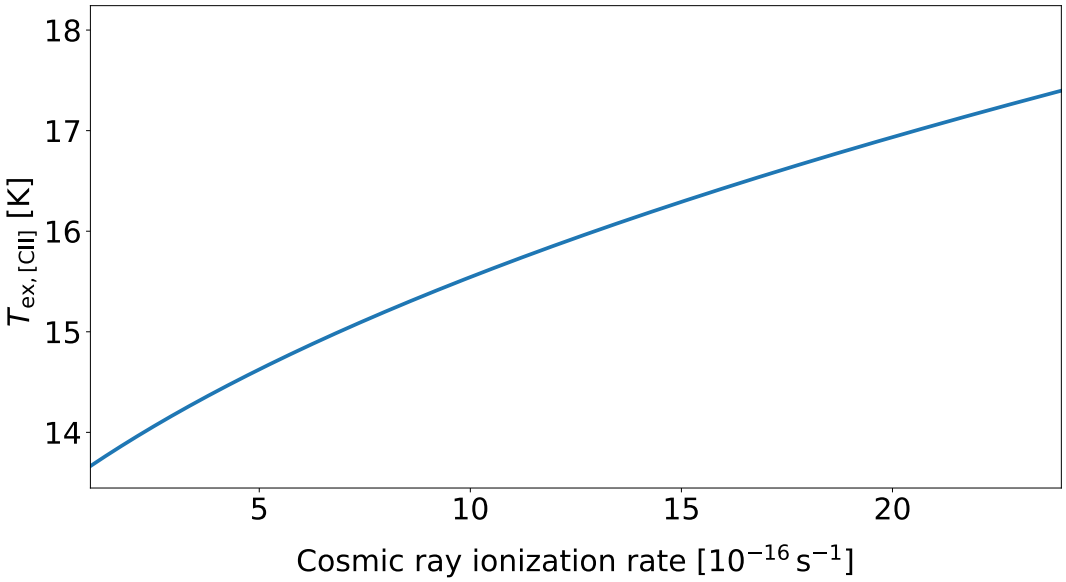

Figure 5.10: [CII] excitation temperature as a function of CR ionization rate.

The two-layer model results for a foreground excitation of $T_{ex,fg} = 15\,K$ and $T_{ex,fg} = 30\,K$ are shown in Fig. 5.8 for the [C II] bright regions along the ring in RCW 120. The corresponding model fit parameters can be found in the appendix, section A.1.1. The model fit is shown as the green spectrum, representing the observed [C II] spectrum in red. The emitting [C II] background is visualized by the blue Gaussians, which have a peak optical depth of approximately $\tau_{[C\,II]} \sim 3$ along the ring. This results in a substantial [C II] column of $\sim 3 \cdot 10^{18}\,cm^{-2}$, which corresponds to $\sim 2000\,M_\odot$ located in the PDR of RCW 120. We also observe a substantial optical depth of $\tau_{[C\,II]} \sim 1$ in the foreground with little variation along the ring. This also results in a high column density for the cold absorbing foreground of $\sim 5{\cdot}10^{17} - 10^{18}\,cm^{-2}$, similar to the findings by Guevara et al. (2020) in various other sources. These high columns in the cold foreground transfer to a substantial mass of $\sim 344 - 685\,M_\odot$. The physical conditions along the PDR in RCW 120 constrained by the temperature range of $T_{ex,fg} = 15 - 30\,K$ are summarized in Table 5.1. The foreground column number density as a function of excitation temperature is also shown in Fig. 5.9 for the cold absorbing layer. The total amount of cold [C II] is probably a factor of two higher since a similar amount of cold material should also be located behind the source. This results in a large amount of material located in a cold layer around the bubble and PDR comparable to the amount of warm emitting gas and not directly accessible through observations.

5.2.3 Atomic hydrogen enveloping RCW 120

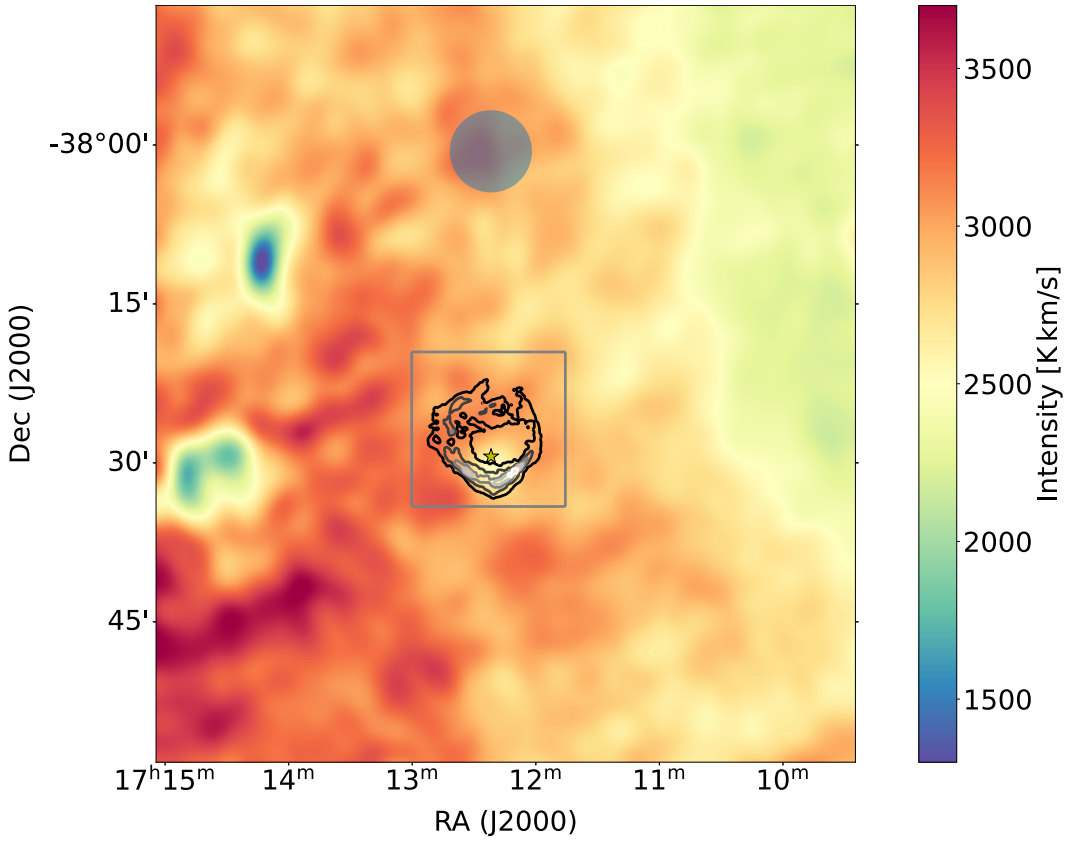

Figure 5.11: H I emission toward RCW 120 integrated from -20 to 10 km s^{-1}. The blue circle shows the area used to obtain the averaged off-position. The diameter is $d_{\rm off} = 3 \cdot \theta_{\rm mb} = 3 \cdot 150''$. The grey box indicates the area observed in [C II]. The [C II] contours range from black to white in intensity levels of 60, 100, 140, 180, 220 K km s^{-1}.

In the previous section 5.2.2, I showed that there is a substantial amount of ionized carbon in a cold absorbing layer similar to the findings of Guevara et al. (2020) for other regions. The question of how this large amount of cold ionized carbon is produced and where it originates from remains open. To find an answer to this question, we will analyze the H I emission towards RCW 120.

The H I emission around the vicinity of RCW 120, shown in Fig. 5.11 for the velocity range relevant for RCW 120, shows little structure compared to the observed [C II] and CO emission. However, the beam size of $\theta_{\rm mb} = 150''$ is much larger than for [C II] and CO. The averaged velocity resolved H I emission from RCW 120, shown by the blue spectrum in Fig. 5.12a, clearly shows an absorption dip at the systemic velocity of RCW 120. To quantify the optical depth and column density of the cold hydrogen responsible for the absorption, I simply determine the intensity difference between the blue spectrum originating from RCW 120 and an off-position mostly free of absorption

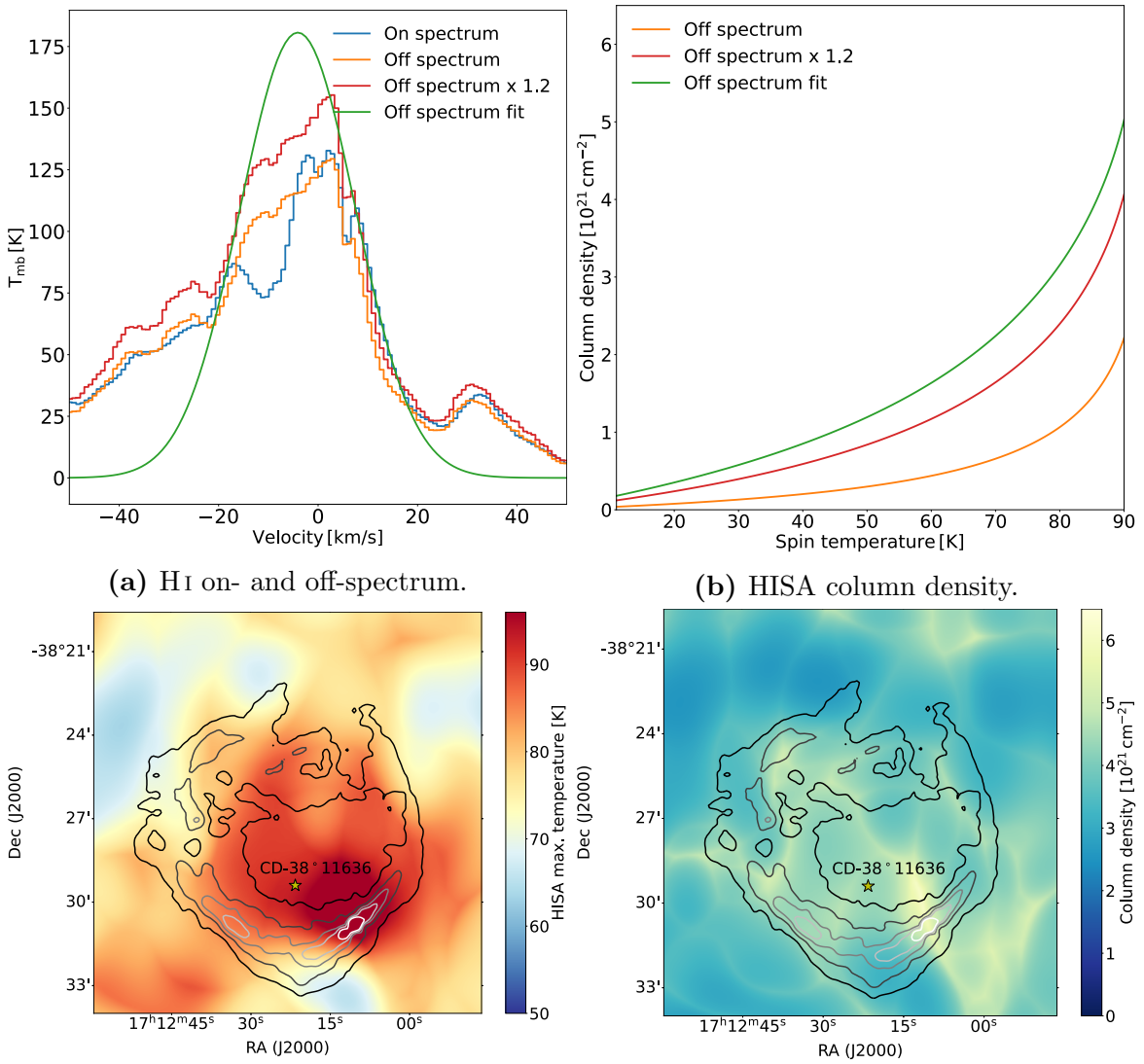

(a) HI on- and off-spectrum.

(b) HISA column density.

(c) HISA temperature.

(d) HISA column density distribution.

Figure 5.12: HISA analysis of RCW 120. (a) The blue spectrum is averaged over RCW 120, and the orange spectrum is observed towards the off-position selected for comparison. The red spectrum is the off-spectrum scaled to match the wing emission of the on-spectrum. The green Gaussian is a fit to the wing emission of the scaled off-spectrum. (b) HISA column density as a function of excitation temperature for the three off-spectra. (c) Max. HISA temperature distribution. (d) HISA column density distribution in RCW 120. Images adapted from Kabanovic et al. (2022).

effects, see section 2.6. The orange spectrum shows the emission towards the selected off-position. The area used to average for the off-position is shown as the blue-shaded circle in Fig. 5.11. It is similar in size to the average on-position. While the off-position shows no absorption dip, it might still be affected by self-absorption effects.

To quantify this uncertainty, I derived the HISA optical depth using three different reference spectra: (i) the spectrum from the off-position, (ii) the off-position scaled so that its wing emission matches the on-position, shown by the red spectrum, and (iii) a Gaussian fit to the wings of the scaled off-position, shown by the green curve. The resulting HISA column number densities for the three reference positions as a function of excitation (spin) temperature are shown in Fig. 5.12b.

I repeat the process and derive the HISA column density for the entire spectral cube using the Gaussian fit as an upper limit for the reference position. The intensity at the absorption dip minimum is a reasonable estimate for the HISA temperature. While this is an upper limit for the HISA temperature, Seifried et al. (2022) showed that this approach best agrees with the simulation results. The derived HISA temperature is shown in Fig. 5.12c, and the corresponding column density distribution is shown next to it in Fig. 5.12d. The HISA distribution shows multiple filament-like structures. While this structure might be real, hinting towards the formation of dense structures in the cold hydrogen envelope, their width is much smaller than the beam size $\theta_{\mathrm{mb}} = 150''$. This makes further analysis of the filamentary structures not feasible.

The derived HISA column densities in RCW 120 match well with the hydrogen column densities derived from the cold absorbing [C II]. This suggests that the possible origin of the large amounts of cold ionized carbon is an atomic hydrogen cloud enveloping the RCW 120. Following Goldsmith et al. (2012), we can write the relation between the [C II] excitation temperature and the hydrogen density n_{H} with the kinetic temperature of the gas T_{kin}:

Collisional excitation of [C II]

$$T_{\mathrm{ex}} = T_0 \ln \left(\frac{R_{ul} n_{\mathrm{H}} + \beta(\tau_0) \left(1 + \frac{\mathcal{J}_\nu(T_{\mathrm{cont}})}{T_0}\right) A_{ul}}{\frac{\mathcal{J}_\nu(T_{\mathrm{cont}})}{T_0} \beta(\tau_0) A_{ul} + R_{ul} n_{\mathrm{H}} e^{-\frac{T_0}{T_{\mathrm{kin}}}}} \right)^{-1} , \tag{5.11}$$

with the escape probability:

$$\beta(\tau_0) = \frac{1 - e^{-\tau_0}}{\tau_0} , \tag{5.12}$$

with $\tau_0 = \tau(v_0)$ the peak optical depth of the transition. The term $\beta(\tau_0) A_{ul}$ can be interpreted as the effective spontaneous decay rate. We assumed that C^+ is only excited through collision with atomic hydrogen. Thus, the de-excitation rate coefficient R_{ul} is given by Barinovs et al. (2005):

$$R_{\mathrm{ul}} = 7.6 \cdot 10^{-10} \mathrm{cm}^3 \mathrm{s}^{-1} (T_{\mathrm{kin}}/100)^{0.14} . \tag{5.13}$$

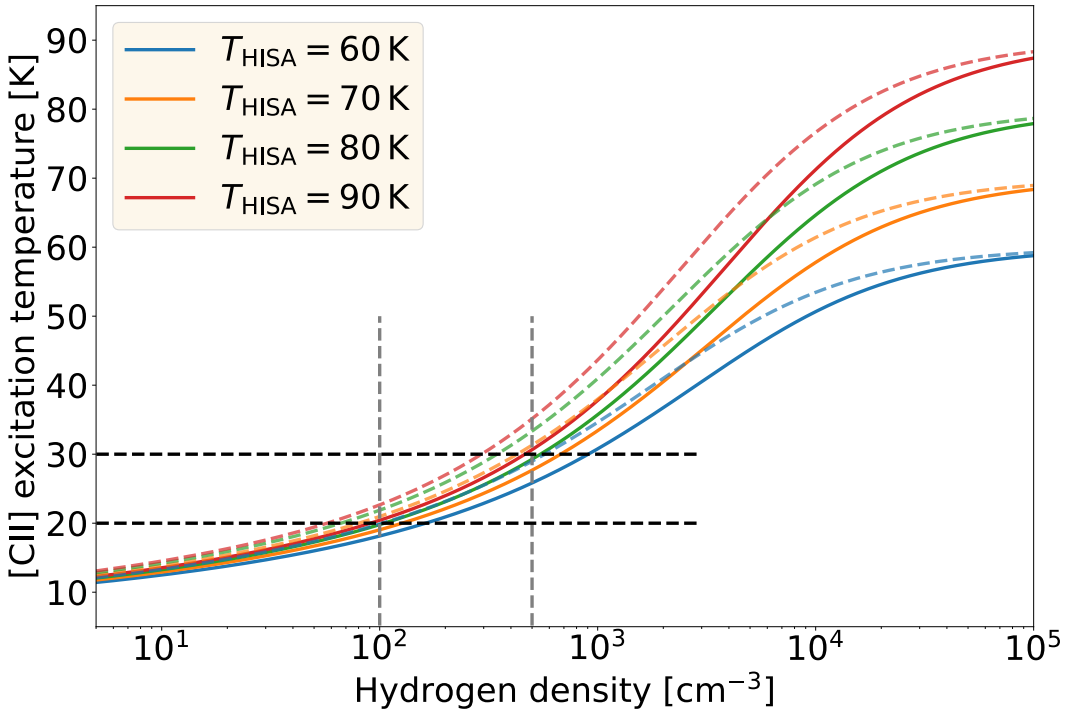

Figure 5.13: C^+ excitation temperature as a function of hydrogen density in the absorbing foreground. The HISA density is derived with four different temperatures (60 K in blue, 70 K in orange, 80 K in green, and 90 K in red), covering the temperature range in RCW 120. The solid lines show the optically thin case while the dashed lines are calculated for a $\tau_0 = 1$. The black dashed lines indicate the [C II] excitation temperatures at 20 K and 30 K. The grey dashed lines indicate the hydrogen densities at 100 cm^{-3} and 500 cm^{-3}.

The excitation temperature approaches the kinetic temperature, $T_{\mathrm{ex}} \rightarrow T_{\mathrm{kin}}$, for increasing hydrogen densities and optical depth:

$$\frac{R_{ul} n_{\mathrm{H}}}{\beta(\tau_0) A_{ul}} \gg 1 \ . \tag{5.14}$$

However, these two temperatures are usually different for the low optical depth values and hydrogen densities found in cold diffuse gas.

Fig. 5.13 shows the cold foreground [C II] excitation temperature as a function of the cold absorbing hydrogen foreground. The calculation was performed for four different HISA temperatures, 60 K, 70 K, 80 K, and 90 K, covering the HISA temperature range in RCW 120. We find that the chosen HISA temperature has little influence on the resulting density. The derived relation allows us to find reasonable physical conditions for the cold atomic envelope. For [C II] excitation temperatures between 20 K and 30 K and a HISA temperature of $\sim$ 80 K, we get hydrogen densities of $\sim 100 - 500\,\mathrm{cm}^{-3}$, assuming the cold diffuse gas is optically thin. These values shift to lower densities for

an increasing optical depth, as shown by the dashed lines in Fig. 5.13 for a $\tau_p = 1$. Thus, the hydrogen density of 500 cm^{-3} derived for the optically thin case can be viewed as an upper limit. The determined hydrogen density range translates into an extent of the HISA cloud of $\sim 5 - 10$ pc. This fits well with the observed size of RCW 120. Lower [C II] excitation temperatures and, therefore, lower hydrogen densities can be excluded since they would require a large extent of the HISA cloud, which would exceed the size of the region. This would make it unlikely for the gas to be associated with RCW 120.

5.2.4 Geometry of RCW 120

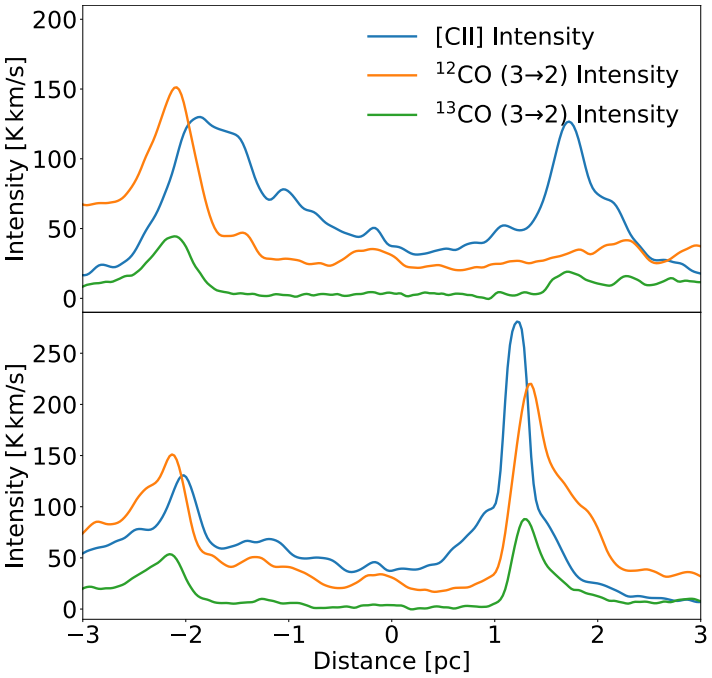

Figure 5.14: [C II], ^{12}CO, and ^{13}CO (3 → 2) intensity along a horizontal cut (upper sub-panel) and diagonal cut (lower sub-panel) through the ionizing star. The two cuts are shown in Fig. 3.7. The blue line shows the [C II] intensity, the orange line the ^{12}CO intensity, and the green line the ^{13}CO intensity. Image adapted from Kabanovic et al. (2022).

The observed symmetric ring-like structure of RCW 120 does indicate a spherical shell, which projected onto the plane of the sky results in the observed ring. This interpretation fits well with the observed expanding [C II] shell. On the other hand, the observed intensities drop steeply towards the region's interior, indicating a significantly smaller column towards the center, see Fig. 3.7. This is especially visible in the molecular tracers ^{12}CO and ^{13}CO. To quantify the intensity ratio between the emission from the ring and the interior, the intensity of the observed ionized carbon and CO lines is plotted along two cuts through the ring, shown in Fig. 5.14. The observed ratio between the ring and the interior for [C II] lies in the range of 3-5, for ^{12}CO 5-10 and for ^{13}CO it reaches values above 10. The large ratio between the ring and the interior suggests a smaller column density towards the interior compared to the ring and the immediate surrounding medium. This is a puzzling result, assuming the bubble expands spherically symmetric into the surrounding parental molecular cloud.

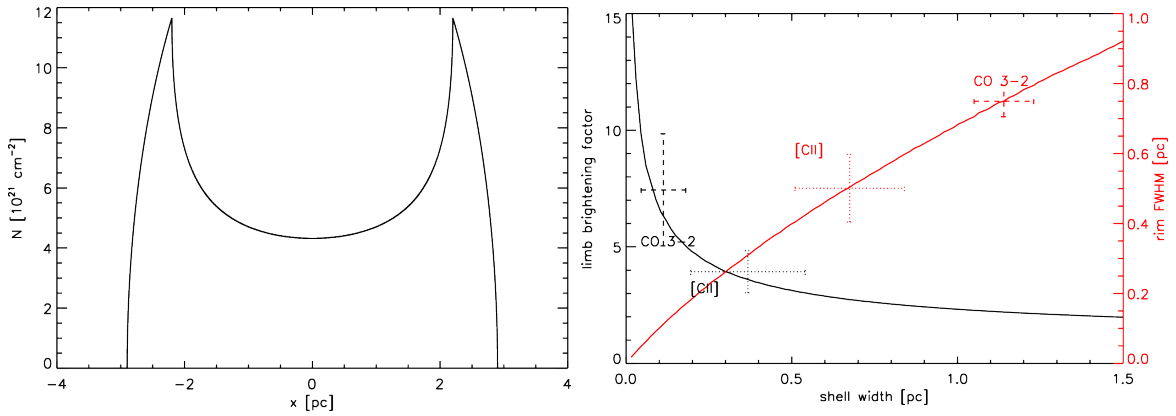

(a) Column density cut. **(b)** Limb brightening.

Figure 5.15: Shell limb brightening of a spherical shell. (a) Column density cut along through the bubble center. (b) Limb brightening factor (in black) and apparent shell width (in red) as a function of geometric shell width. The data points with error bars indicate the observed variations for the limb-brightening factor and shell width for [CII] and CO. Image adapted from Kabanovic et al. (2022).

However, the projection of a spherical shell onto the plane of the sky would increase the intensity of the ring due to the limb-brightening effect. To quantify the limb-brightening effect, Kabanovic et al. (2022) utilized SimLine (Ossenkopf et al., 2001), which solves the radiative transfer equations for spherical symmetry. The calculated limb-brightening factor as a function of shell width is plotted in 5.15 alongside the observed values. The column density along a cut through the center of a spherically symmetric shell for an observed apparent shell width of $\sim 0.7\,\mathrm{pc}$ is shown in Fig. 5.15a. This results in a limb- brightening factor of ~ 3, which is much lower than observed in CO. For a spherical shell, the limb-brightening factor increases with decreasing shell width, as shown by the black curve in Fig. 5.15b, alongside with a decrease in the apparent shell width shown by the red curve. To compare the observed values (see Fig, 5.14) alongside the model parameter space, we show the observed range for CO and [CII], which are indicated by the error bars in Fig. 5.15b. For the [CII] emission, a shell width of $0.6\,\mathrm{pc}$ results in a marginal fit for both model parameters, the rim width and the intensity ratio, while the CO emission shows a large discrepancy between the observed shell width and the limb- brightening factor. Summarizing, we observe an expanding shell in [CII], see Fig. 5.5a, which suggests a spherical geometry of the HII region, but the observed CO intensity ratio between the ring and the interior contradicts the spherical geometry of RCW 120. In section 5.2.1, I discussed that both observed tracers show strong optical depth effects. Especially CO shows high optical depth effects towards the center, as shown in Fig. 5.6, which aligns spatially with the dark lanes in front of the HII region. Thus, possible adsorption by a cold foreground might significantly affect the observed intensity ratio between the interior and the ring.

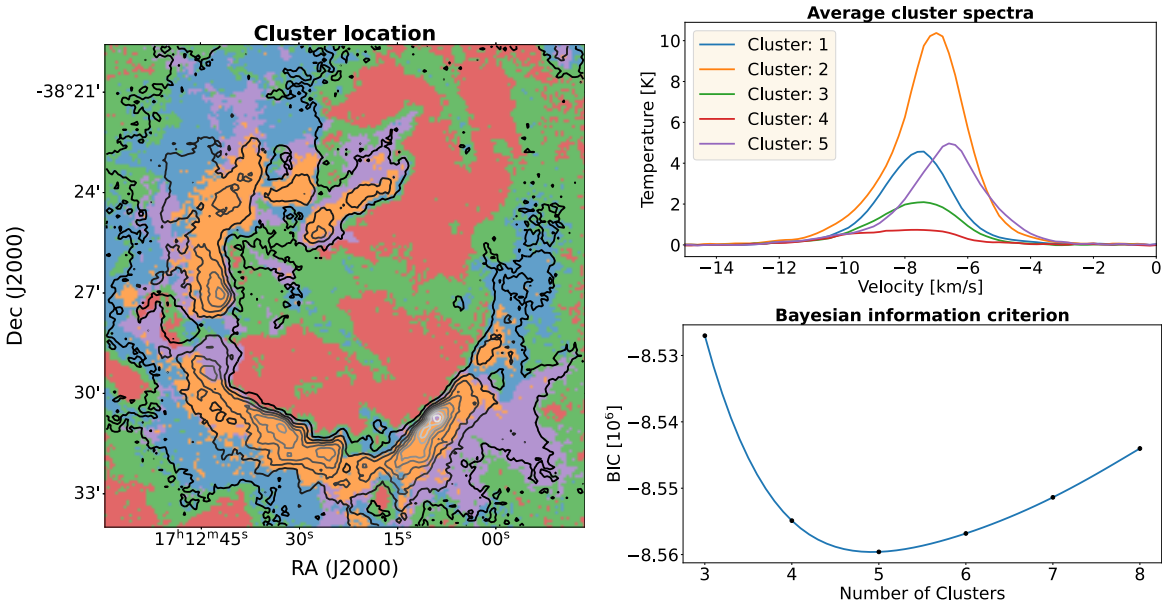

Figure 5.16: Cluster determined with the Gaussian mixture model (Kabanovic et al., 2022). Left panel: The spatial distribution of the five clusters. Upper right panel: The averaged spectra from each cluster. Lower right panel: Bayesian information criterion. The black data points show the BIC value for the number of clusters reaching its minimum at five clusters. The blue curve shows the parabolic fit indicating the trend of the data points.

To disentangle the emitting background from the cold absorbing foreground and therefore determine the region's total spatial column density distribution, we need to apply the two-layer multicomponent model to the entire CO (3→2) spectral cube. This section concentrates on the ^{12}CO and ^{13}CO (3→ 2) data sets as they carry the important information on the bulk of the molecular material and the self-absorption observed in the cold foreground gas.

The two-layer model needs an initial guess to converge toward a physically meaningful solution. This is a straightforward task for a single spectrum. However, it is not possible to find the initial conditions for a spectral cube containing thousands of spectra in a reasonable time (with limited computing power or lifetime). To overcome this problem, we use the fact that the observed spectral shape is not random but confined by the physical conditions in the gas from which the emission is originating. To solve the model for the entire spectral cube, we can use identical initial conditions for a set of spectra with similar shapes. I group the spectra using the Gaussian mixture model described in section 4.2.2. The clustering algorithm is applied to the ^{13}CO data set since it is less affected by foreground absorption effects which significantly alter the shapes and intensities of the ^{12}CO spectra.

First, I used the BIC to determine an appropriate number of clusters that represents

Table 5.2: Averaged CO (3→2) physical properties of the emitting and absorbing layers for the five clusters in RCW 120. The table is adapted from Kabanovic et al. (2022).

		Background				
Region	(1) A [pc^2]	(2) τ_{CO}	(3) N_{CO} [10^{18} cm^{-2}]	(4) N_{H_2} [10^{21} cm^{-2}]	(5) M_{H_2} [$M_\odot$]	(6) L_{CO} [$L_\odot$]
Cluster 1	9.9	9.0	0.4	4.3	685.0	2.5
Cluster 2	6.2	23.4	0.9	10.5	1035.0	2.0
Cluster 3	15.7	4.0	0.2	2.2	561.0	3.5
Cluster 4	11.2	1.4	0.1	0.9	169.0	1.7
Cluster 5	6.3	9.5	0.4	5.0	510.0	1.9
		Foreground				
Cluster 1	9.9	1.7	0.2	1.8	284.0	0.1
Cluster 2	6.2	1.7	0.2	1.8	180.0	0.1
Cluster 3	15.7	1.9	0.2	1.9	491.0	0.2
Cluster 4	11.2	2.4	0.1	1.7	310.0	0.1
Cluster 5	6.3	1.8	0.2	2.0	205.0	0.1

(1) Cluster size of the regions defined by the GMM.

(2,7) CO (3→2) peak optical depth.

(3,8) CO column density, determined using Eq. 2.72.

(4,9) Molecular hydrogen column density, using $CO/H_2 = 8.5 \cdot 10^{-5}$ (Tielens, 2010).

(5,10) Molecular hydrogen mass of the layers.

(6,11) Luminosity for the background and foreground layers.

the ^{13}CO data cube. I performed the calculation a hundred times since the random initial cluster distribution can imprint itself on the final solution. The averaged BIC values are shown in the lower right panel in Fig. 5.16. The error bars, which show the standard deviation, are not visible since the initial cluster distribution has little effect on the solution. The BIC reaches its minimum at five clusters, whose spatial distribution is shown in the left panel of Fig. 5.16. The corresponding average spectra are plotted in the upper right panel. The emission from the dense part of the ring is indicated by cluster 2 (in orange). The two clusters 1 and 5 (shown in blue and purple) surround the dense part of the PDR, but are blueshifted (cluster 1) and redshifted (cluster 5) with respect to the bulk emission of cluster 2. This indicates that even the dense ring surrounding the H II has a complex velocity structure. Cluster 3 (shown in green) traces the two dark lanes, visible in Hα absorption and spanning diagonally across RCW 120. Cluster 4 (represented in red) traces mainly the weak emission originating from the interior of the region.

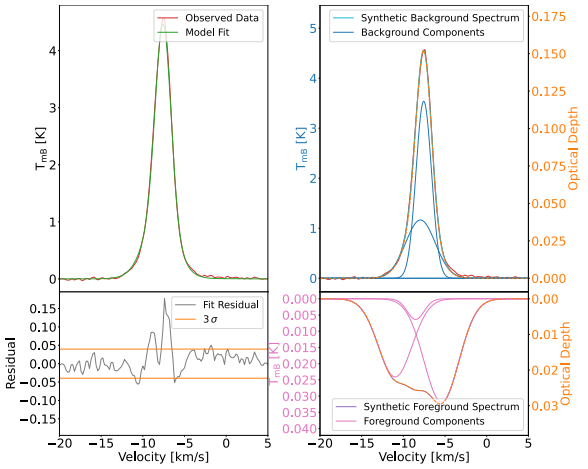

(a) **Cluster 1:** ^{13}CO (3→2)

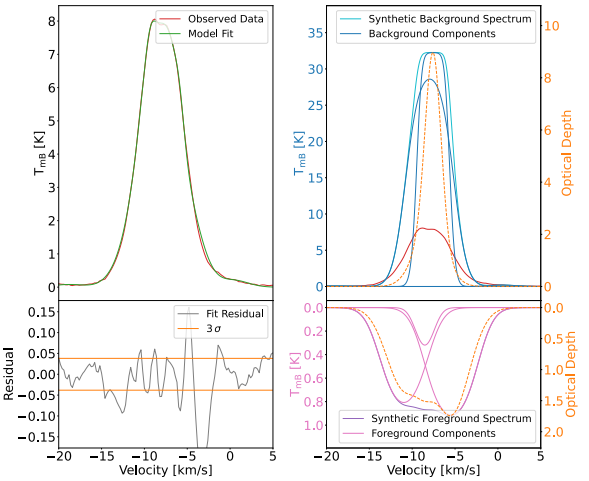

(b) **Cluster 1:** ^{12}CO (3→2)

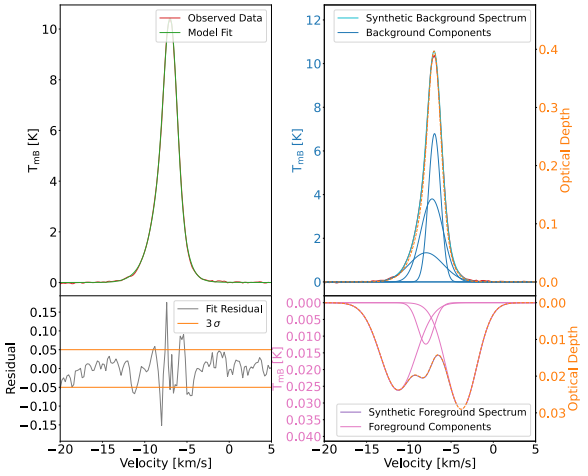

(c) **Cluster 2:** ^{13}CO (3→2)

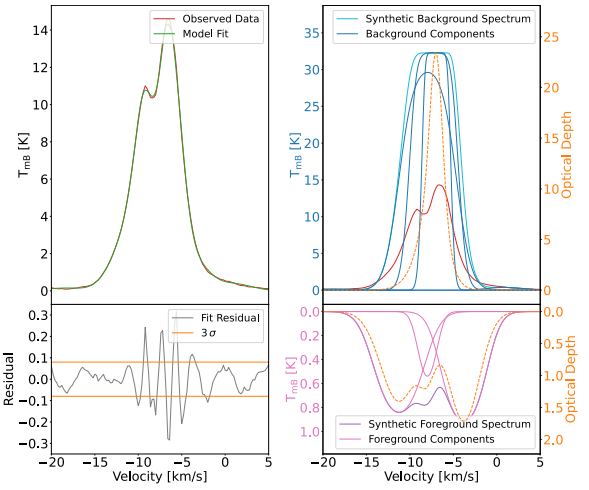

(d) **Cluster 2:** ^{12}CO (3→2)

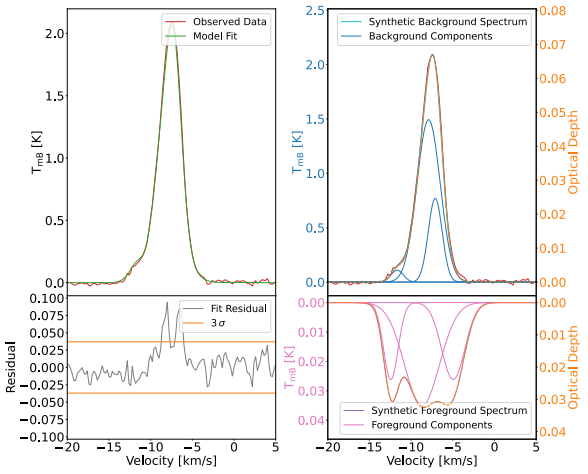

(e) **Cluster 3:** ^{13}CO (3→2)

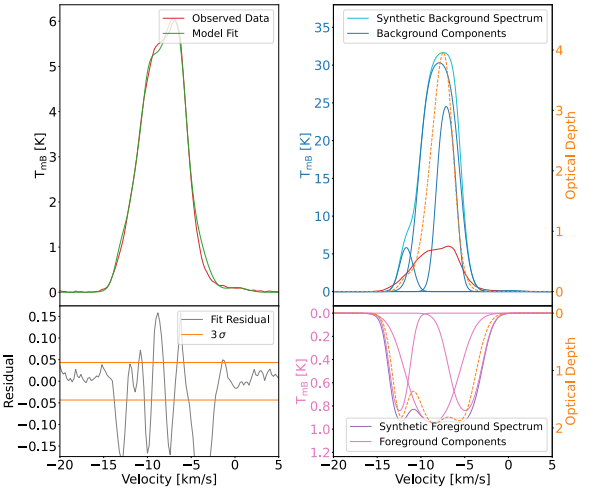

(f) **Cluster 3:** ^{12}CO (3→2)

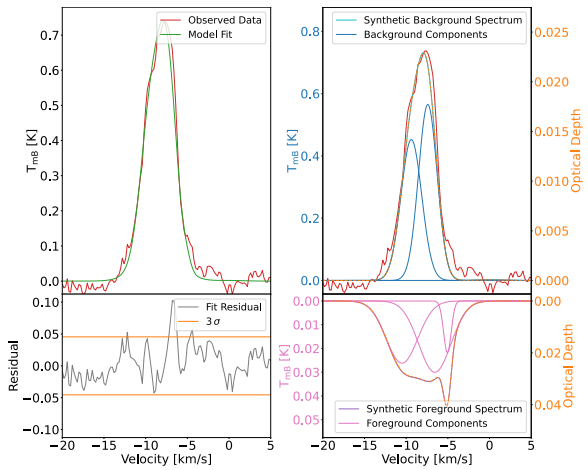

(g) Cluster 4: ^{13}CO (3→2)

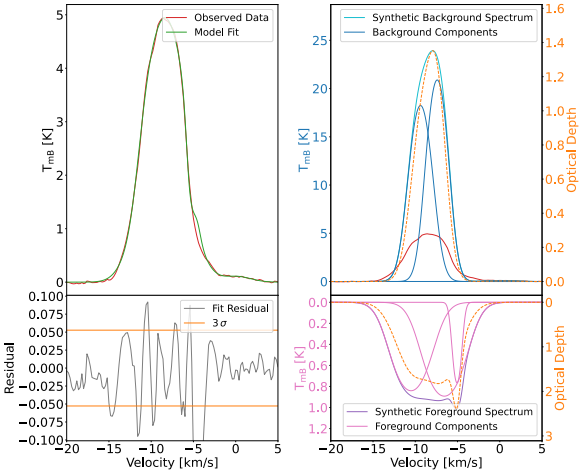

(h) Cluster 4: ^{12}CO (3→2)

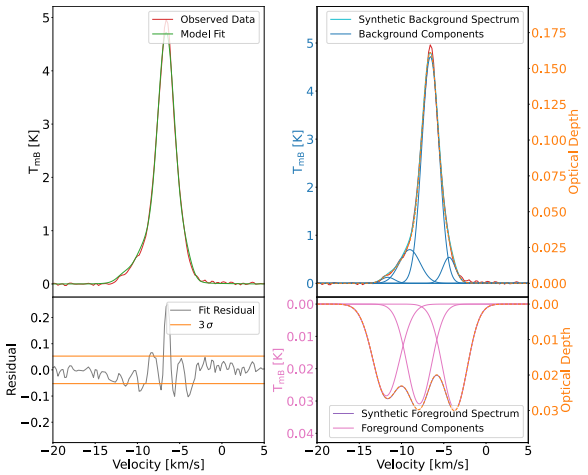

(i) Cluster 5: ^{13}CO (3→2)

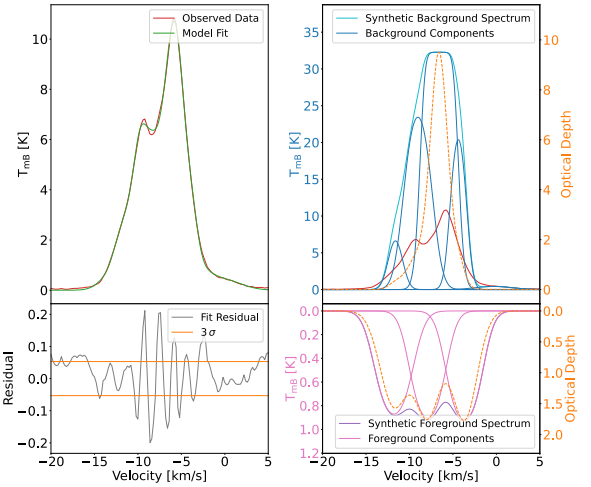

(j) Cluster 5: ^{12}CO (3→2)

Figure 5.17: CO two-layer multicomponent model solution for the five GMM clusters (Kabanovic et al., 2022). The spatial location of each cluster is shown in Fig. 5.16. Left panel ^{13}CO (3→ 2) model fit. Right panel: ^{12}CO (3→ 2) model fit. Left upper sub-panel: The observed data are shown by the red data points, and the green curve shows the model fit. Left lower sub-panel: The grey data points show the fit residual, and the two orange horizontal axes show the 3σ detection level. Right upper sub-panel: the blue Gaussians show the single background components. The cyan curve is the superposition of all the background components. The dashed orange curve shows the velocity resolved background optical depth. Right lower sub-panel: The pink Gaussians show the single foreground components. The purple curve is the superposition of all the foreground components. The dashed orange curve indicates the velocity resolved foreground optical depth.

To find proper initial conditions for each cluster, I solved the two-layer multicomponent model for each averaged spectrum. The model fit for both isotopes is shown in Fig. 5.17, and the corresponding fit model parameter can be found in the appendix, section A.1.2. The derived physical properties are summarized in Table 5.2. I derived a background excitation temperature of $T_{\mathrm{ex,bg}} = 40\,\mathrm{K}$ from the optically thick ^{12}CO line emission using equation (4.16). The foreground excitation temperature was determined more pragmatically to $T_{\mathrm{ex,fg}} = 6\,\mathrm{K}$, which is the highest foreground excitation temperature that resulted in a satisfying model fit for all five clusters. Similar to the [C II] line analysis, the intensity of the background components overshoots the observed ^{12}CO intensity, which requires a cold absorbing layer that absorbs a significant amount of the background emission. The CO optical depth derived this way is high, especially towards the dense parts of the ring where it reaches peak values around $\tau_{\mathrm{CO}} \sim 20$, but it is significantly lower than the values derived using the single-layer model, shown in section 5.2.1. The molecular U-shaped envelope consists of cluster 1, 2, and 5, which add up to a total mass of $\sim 2000\,\mathrm{M}_\odot$ for the emitting warm background material and $\sim 670\,\mathrm{M}_\odot$ for the absorbing foreground. As already mentioned in section 5.2.2, the overall cold molecular mass is likely to be a factor of two higher since the cold material located behind the source is not accessible.

While the amount of background components needed to represent the observed spectrum varies along the region, see Fig. 5.17, the foreground is usually best represented by three components, one at the systemic velocity of RCW 120, a blueshifted, and a redshifted component with respect to the systemic velocity. The component located at the systemic velocity of $\sim -7.5\,\mathrm{km\,s^{-1}}$ originates likely from a temperature gradient along the line of sight. The blueshifted component is probably linked to the mechanical energy input of the expanding bubble into the surrounding medium. The interpretation of the redshifted component is less straightforward since it is visible in absorption and therefore located between the observer and the region. Thus, the redshifted component might indicate a molecular inflow.

We can now use the results from the averaged spectra as an initial guess for the entire spectral cube. Thus, I applied the two-layer model, as described in section 4.3.1, in an automated unsupervised fashion. The resulting velocity-resolved column density maps of the two CO layers are shown in Fig. 5.18. Most of the CO background column density is concentrated in the dense PDR around the systemic velocity. The two dark lanes located in front of the H II region are also visible at the systemic velocity in the background layer since the dark lanes are facing the star and are heated up from the inside of the bubble, leading to subsequent CO cooling via the radiation of the J(3→2) line. Conversely, the velocity-resolved foreground is rather diffuse and does not show an increase in density toward the PDR. However, at the systemic velocity, we observe an increase in column density from the northeast to the southwest through the region's center. This increase in foreground column density correlates well with the absorption

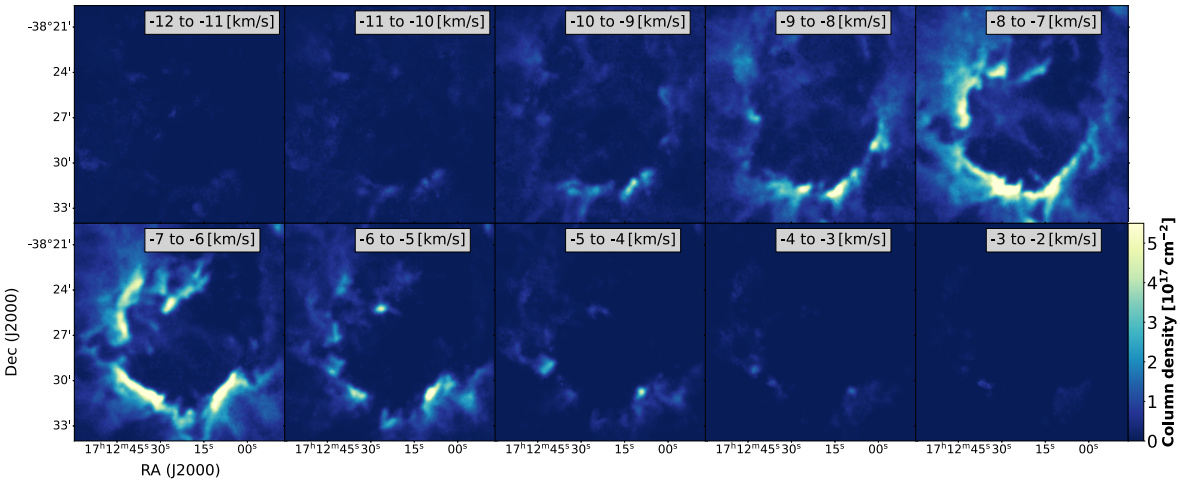

(a) Background CO column density.

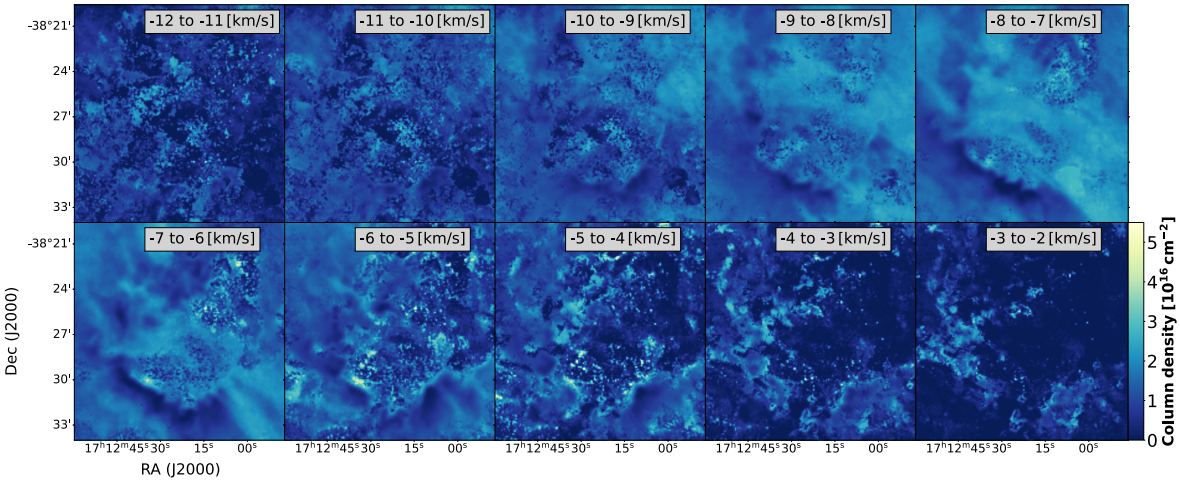

(b) Foreground CO column density.

Figure 5.18: Velocity resolved CO column density maps (Kabanovic et al., 2022). (a) CO column density of the warm emitting background layer (b) CO column density of the cold absorbing foreground layer.

features seen in ^{12}CO around the systemic velocity (Fig. 5.3). Moving toward redshifted velocities, we observe a sudden change in the morphology of the foreground distribution, which now follows the dense PDR structure. This morphological change could suggest that the dense ring in RCW 120 is still accreting mass from the surrounding cold material.

The background and foreground column density along a horizontal and diagonal cut through the star, as indicated by the two grey lines in Fig. 3.7, is shown in Fig. 5.19. While the background column density increases steeply at the dense PDR, the foreground column density stays almost constant throughout the entire region. Thus, the absorption by the foreground material does not explain the column density deficit

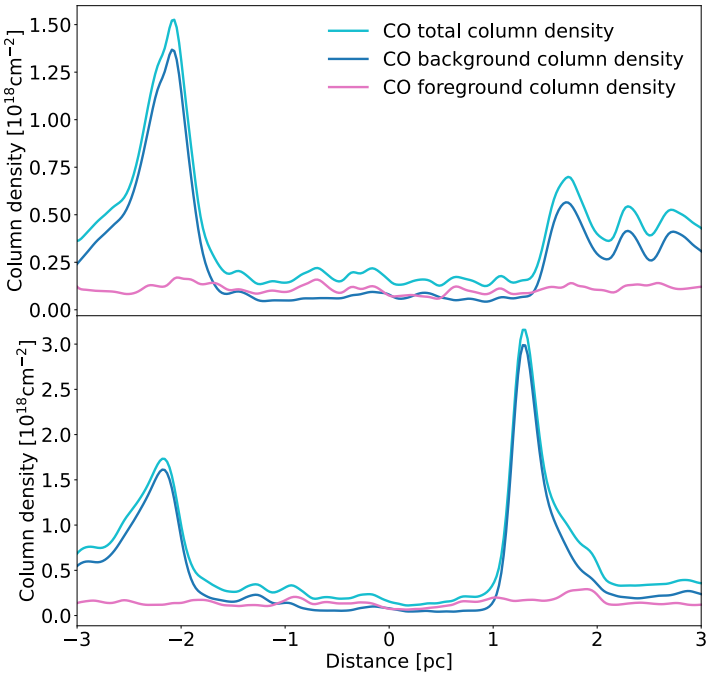

Figure 5.19: CO column density cuts along RCW 120 (Kabanovic et al., 2022). The upper panel shows the CO column density along the horizontal cut and the lower cut diagonally through the star as indicated by the two grey lines in Fig. 3.7. The blue curve shows the background column density, the pink curve shows the foreground column density and the cyan curve shows the total column density.

toward the center with respect to the ring.

To align both observed features, the expanding [CII] bubble and the missing column density toward the bubble's center, we propose that the parental molecular cloud had to be flattened along the line of sight. Thus, the expanding stellar wind-driven bubble is bursting out of the flat parental molecular cloud. The material distributed parallel to the long axis, which aligns approximately with the plane of the sky, is compressed to a torus-like structure by the expanding HII region.

5.3 Assembly of molecular clouds in Cygnus

As shown in the previous sections, CO originates from dense molecular clouds and is, therefore, a good tracer of the H_2 molecule. Since molecular hydrogen is more abundant than CO, its self-shielding from the photodissociating FUV radiation is more efficient. This difference in column density between the two molecules can produce molecular hydrogen gas that is not traced by CO. Such a gas component is usually referred to as "CO-dark" (Wolfire et al., 2010). It can constitute an important part of the gas in galaxies: Madden et al. (2020), for example, showed that 70 to 100% of the total H_2 mass in dwarf galaxies is not traced by CO. However, they found that this gas component is well-traced by the [CII] line. Until recently, there was no large-scale [CII] mapping project that was able to identify CO-dark gas associated with molecular clouds in the Milky Way. It is with the FEEDBACK project that these maps became available, and we used the largest [CII] map in this sample, covering the Cygnus X region, to search for CO-dark gas traced by [CII]. In addition, the spectral resolution

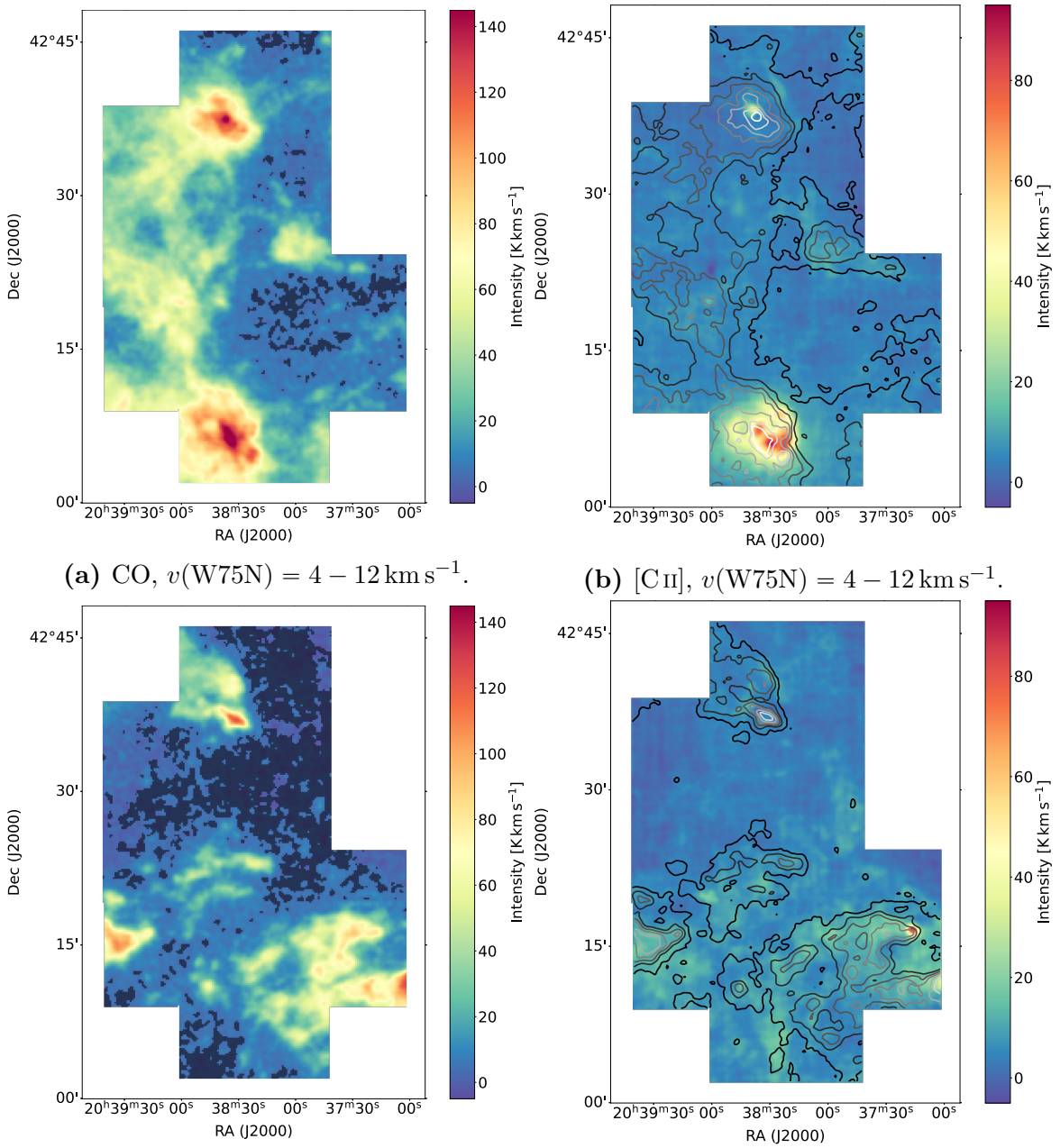

(a) CO, $v(\mathrm{W75N}) = 4 - 12\,\mathrm{km\,s^{-1}}$.

(b) [C II], $v(\mathrm{W75N}) = 4 - 12\,\mathrm{km\,s^{-1}}$.

(c) CO, $v(\mathrm{HV}) = 12 - 20\,\mathrm{km\,s^{-1}}$.

(d) [C II], $v(\mathrm{HV}) = 12 - 20\,\mathrm{km\,s^{-1}}$.

Figure 5.20: [C II] and CO intensity maps from Cygnus X for the W75N (upper panel) and the high-velocity range (lower panel). Left panel: The CO ($1 \rightarrow 0$) emission observed with the Nobeyama telescope (Yamagishi et al., 2018). The dark-shaded area shows the CO-dark and [C II] bright region. Right panel: [C II] emission. The contours show the corresponding CO emission ranging from black to white, corresponding to intensities of $10\,\mathrm{K\,km\,s^{-1}}$ to $110\,\mathrm{K\,km\,s^{-1}}$ in steps of $20\,\mathrm{K\,km\,s^{-1}}$.

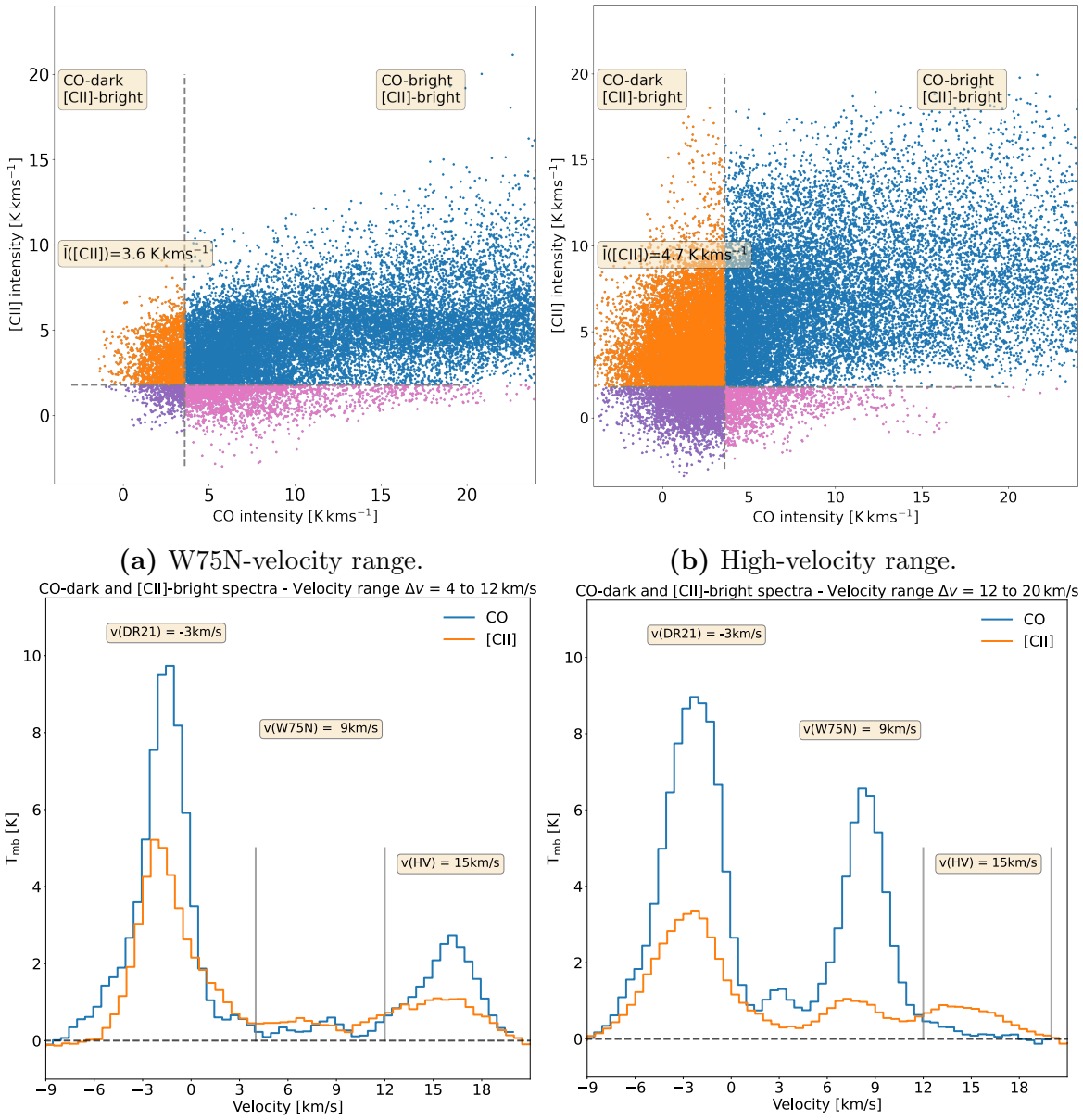

(a) W75N-velocity range.

(b) High-velocity range.

(c) Average Spectra, v(W75N).

(d) Average Spectra, v(HV).

Figure 5.21: CO-dark and [CII] bright emission for the two velocity regimes. Upper panel: [CII] intensity versus CO intensity. The two dashed lines indicate the 3σ detection limit for both lines. The purple data points are located below the detection limit for both lines. Data points above the detection limit are shown in blue for both lines. CO-bright but [CII]-dark data points are shown in pink. CO-dark but [CII]-bright data points are shown in orange. Lower panel: The averaged spectra over the orange data points. The dashed vertical lines indicate the corresponding velocity range. Image adapted from Schneider et al. (2023).

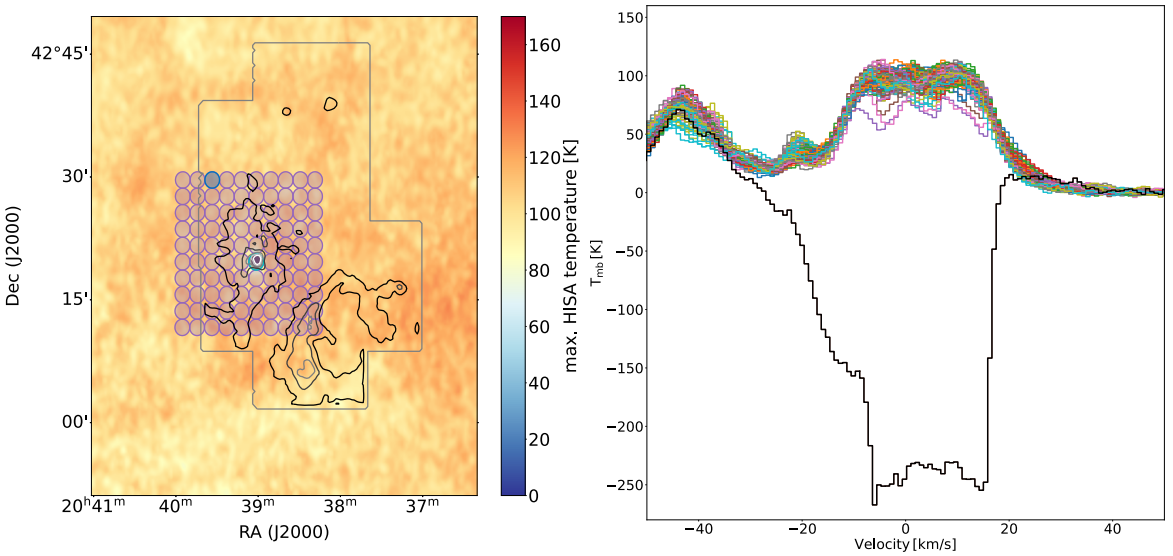

(a) HISA temperature.

(b) HISA off-spectra.

Figure 5.22: HISA temperature in Cygnus X (Schneider et al., 2023). (a) The grey box outlines the observed area in [C II], and the contours indicate [C II] emission corresponding to intensities of 50 K km s^{-1} to 210 K km s^{-1} in steps of 40 K km s^{-1}. The cyan circle indicates the DR21 on-position. The blue-shaded circle shows the chosen off-position free of absorption. (b) 100 averaged H I spectra. The absorption spectrum originates from the on-position DR21. The location of the spectra is indicated by the purple circles shown in (a).

of the data allows us to investigate the velocity distribution of the [C II] emitting gas.

The observed [C II] and CO emission in the Cygnus X region is shown in Fig. 5.20. The upper panel shows the integrated emission over the W75N velocity range (4-12 km s^{-1}), and the lower panel shows the high velocity (HV) range (12-20 km s^{-1}). While most of the emission originates from lower velocities associated with well-known massive star-forming regions, in the following, we are only interested in the high-velocity flows in Cygnus. The right panel of Fig. 5.20 shows the integrated [C II] emission overlaid with contours of the CO integrated intensity. We find that substantial parts of the observed region are devoid of CO emission, while extended [C II] emission is clearly detected.

Fig. 5.21a and 5.21b show the [C II] intensity plotted against the CO intensity for the two velocity ranges to quantify the amount of the CO-dark but [C II] bright component. The two dashed grey lines indicate the 3σ detection threshold of 1.8 K km s^{-1} for [C II] and 3.6 K km s^{-1} for CO. The orange data points show the [C II]-bright but CO-dark components for each velocity range. The corresponding average spectra are shown in Fig. 5.21c and 5.21d. The [C II] spectra display a velocity bridge of emission between the three velocity components DR21, W75N, and HV. The CO emission also shows

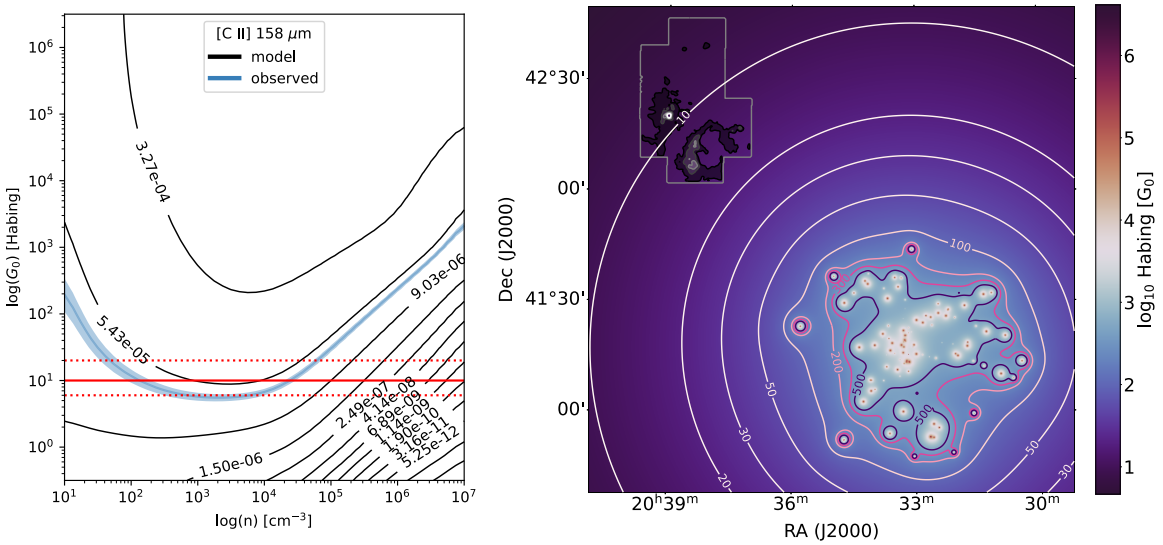

(a) PDR model result. **(b)** UV-field in Cygnux X.

Figure 5.23: UV-field in Cygnus X (Schneider et al., 2023). (a) PDR model FUV field and hydrogen density parameter space. The blue isocontour corresponds to the HV [C II] integrated intensity of $\sim 5\,\mathrm{K\,km\,s^{-1}}$. Its width is determined by the integrated rms of $\sim 0.6\,\mathrm{K\,km\,s^{-1}}$. The determined FUV strength of $10\,\mathrm{G_0}$ is shown by the red horizontal line. The red dashed lines indicate the FUV variation along the observed region. (b) The UV field in Habing [$\mathrm{G_0}$] is plotted on a $\log_{10}$-scale. In addition, UV contours on a linear scale are shown. The grey box outlines the area observed in [C II]. The [C II] emission is indicated by the contours ranging from black to white corresponding to intensities of $50\,\mathrm{K\,km\,s^{-1}}$ to $210\,\mathrm{K\,km\,s^{-1}}$ in steps of $40\,\mathrm{K\,km\,s^{-1}}$.

this bridging effect, but the emission is very weak in the HV range, where we find the largest amount of [C II]-bright gas. The spatial distribution of the CO-dark component is shown by the shaded area in Fig. 5.20c. In total, 29% (6%) of the area in the HV (W75N) range is CO-dark and [C II]-bright. The amount of the [C II] bright but CO-dark material decreases toward lower velocities as visible in Fig. 5.20a. However, these findings strongly depend on the observed area, which is biased toward the bright regions.

To constrain the physical properties of the atomic gas in and around the Cygnus complex, I performed a hydrogen self-absorption (HISA) analysis, similar to the study for RCW 120 (section 5.2.3). First, I determined the HISA temperature in Cygnus X from the absorption dips in the spectra. The resulting HISA temperature distribution is shown in Fig. 5.22a. The temperature is rather homogeneously distributed around $\sim 100\,\mathrm{K}$. I then estimated the hydrogen column number density against the bright continuum source DR21. To find a suitable off-position, I extracted average spectra over a hundred positions close to DR21 indicated by the purple circles in Fig. 5.22a.

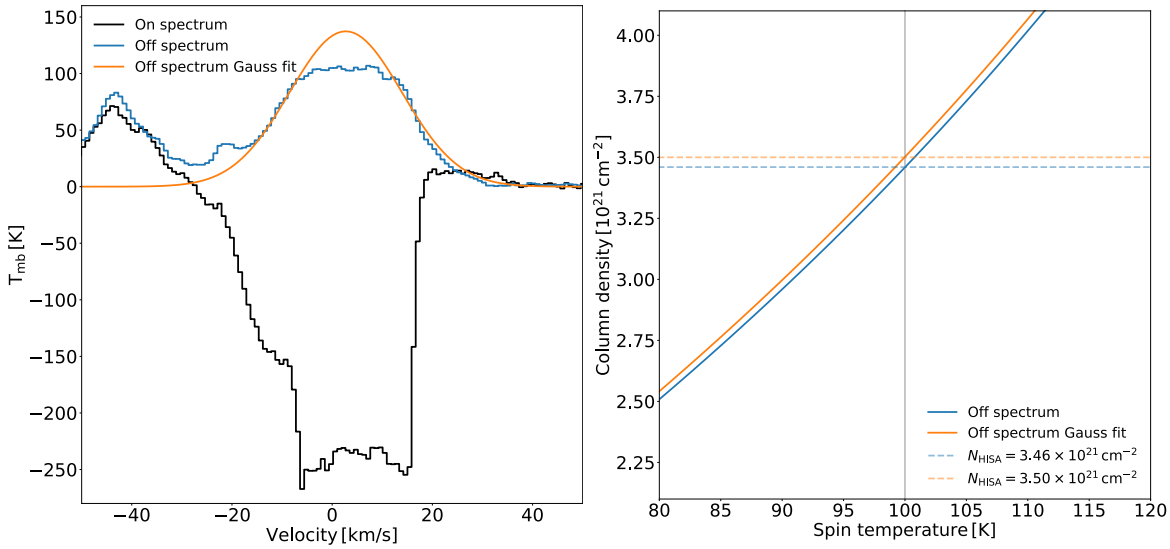

(a) Average H I spectra. **(b)** HISA column density.

Figure 5.24: HISA parameters in Cygnus. (a) Absorption towards DR21 is shown by the black spectrum. The absorption-free off-position H I emission is shown by the blue spectrum. The fit to the off-spectrum is shown by the orange Gaussian. (b) HISA column density as a function of temperature for both reference positions. Image adapted from Schneider et al. (2023).

The off-position spectra alongside the absorption spectrum toward DR21 are shown in Fig. 5.22b. The single spectra display little variation, already suggested by the rather homogeneous temperature map. The chosen off-position spectrum is given by the blue spectrum in Fig 5.24a. Considering that the cold-absorbing hydrogen cloud might also affect the off-position, I performed a Gaussian fit to the wings of the off-spectrum shown by the orange Gaussian. The resulting column number density for both reference spectra is displayed in Fig. 5.24b. The derived column density from the off-spectrum can be considered as a lower limit, while the used Gaussian component represents the upper limit. For the determined spin temperature, a hydrogen column density of $\sim 3.5 \cdot 10^{21}\,\mathrm{cm}^{-2}$ in the velocity range between $4\,\mathrm{km\,s}^{-1}$ to $20\,\mathrm{km\,s}^{-1}$ is reached.

Using equation 5.11, I determined the [C II] excitation temperature of $T_{\mathrm{ex}} = 21\,\mathrm{K}$ from the kinetic temperature of the HISA cloud $T_{\mathrm{kin}} \sim T_{\mathrm{HISA}} \sim 100\,\mathrm{K}$ and its density of $n = 100\,\mathrm{cm}^{-3}$. The hydrogen density was then derived by applying a PDR model using the PDR Toolbox (Pound and Wolfire, 2023), assuming a UV-field of $10\,G_0$ and an integrated [C II] intensity of $\sim 5\,\mathrm{K\,km\,s}^{-1}$ (Schneider et al., 2023). I estimated the UV-field using the method explained in section 4.5. The resukting UV-field is shown together with the PDR modeling results in Fig. 5.23. Using equation (2.65) results in a C^+ column density of $N_{[\mathrm{C\,II}]}(I \sim 5\,\mathrm{K\,km\,s}^{-1}) \sim 6 \cdot 10^{17}\,\mathrm{cm}^{-2}$, which corresponds to a hydrogen column density of $\sim 3.7 \cdot 10^{21}\,\mathrm{cm}^{-2}$, similar to the column density derived

independently using the HISA method. This suggests that the high-velocity CO-dark, [C II]-bright gas originates from the cold atomic gas. The observed [C II] remarkably traces the molecular cloud formation from its initial atomic flow. The interaction of atomic flows leads to the formation of dense molecular clouds in Cygnus X, which are the birthplaces of stars and, in particular, massive stars.

Discussion

Within the last decade, SOFIA performed high angular and spectral resolution line mapping of extended regions in the Milky Way and external galaxies in the [CII] 158 μm line. Valuable discoveries were made that allowed us to progress significantly in our understanding of the physics of the interstellar medium. Observations of the [CII] line, combined with data from CO and HI, revealed the dynamics of the gas in HII region bubbles, emphasized the importance of studying self-absorption effects, and traced CO-dark gas during the molecular cloud assembly process. In the following, I will put these new findings into context of what was known before these discoveries were made and which open questions remain.

6.1 The [CII] line as a tracer for the gas dynamics

Stars still embedded in the parental molecular cloud interact with the surrounding medium through radiation and stellar winds. The injected mechanical and radiative energy compresses the surrounding medium into ring-like structures as shown in Fig. 6.1 over large parts of the Milky Way. These compressed rings can further fragment into dense clumps, the birthplaces of stars. It is therefore essential to understand what the mechanisms are that drive the bubble expansion and compression of the surrounding medium. The mechanical energy carried by the stellar wind is only a small fraction of the radiative luminosity of a star. However, the coupling efficiencies to the ISM of each process are less straightforward to determine, which makes the dominant process uncertain. Nevertheless, theoretical studies predict in general that momentum injection by radiation dominates that of stellar winds (Haid et al., 2018). To verify this theoretical prediction and to investigate the conditions for one or the other to dominate, we can make use of the spectrally resolved [CII] emission, which is an ideal tracer for gas kinematics in massive star-forming regions.

As part of the large Orion A mapping program (Higgins et al., 2021), see also section 3.3, Pabst et al. (2020) observed for the first time expanding [CII] shells in the Orion Veil, M 43, and NGC 1977 directly through velocity resolved [CII] spectra. While M 43 and NGC 1977 are thermally expanding bubbles powered by B-type stars

Figure 6.1: Infrared emission from dust and stars of a part of the Milky Way toward the constellation Scorpius. This segment of the survey spans galactic longitudes from 343.5 to 351.7 degrees and is centered at 0 degrees of galactic latitude. The most striking features are the Cat's Paw Nebula (NGC 6334) at the upper left of the image and the almost perfect spherical shape of RCW 120 towards the center. The emission from polycyclic aromatic hydrocarbons, which is excited by radiation from nearby stars, is shown in green. The thermal emission from warm dust is represented in red. The overlap of both regions is visible in yellow. The stars are visible in blue. Credit: NASA/JPL-Caltech/Univ. of Wisconsin.

(NU Ori in M 43 and 42 Orionis in NGC 1977) with expansion velocities of $\sim 6\,\mathrm{km\,s^{-1}}$ and $\sim 1.5\,\mathrm{km\,s^{-1}}$, respectively, the Orion Veil is expanding fast with $\sim 13\,\mathrm{km\,s^{-1}}$, driven by the stellar wind of the O-type star θ^1 Ori C. The derived kinetic energy of the expanding shell from the velocity resolved [C II] emission indicates that the mechanical energy carried by the stellar wind is efficiently converted into the kinetic energy of the expanding shell.

Subsequent velocity resolved [C II] observations of RCW 120 (Luisi et al., 2021) in the FEEDBACK project, see section 5.1, also revealed a fast expanding [C II] shell with a velocity of $\sim 15\,\mathrm{km\,s^{-1}}$. Similar to the blister bubble in Orion A, the interior of RCW 120 is filled with hot X-ray emitting plasma, characteristic of a stellar wind-driven bubble. The expanding bubble compressed the surrounding medium into a ring-like structure enveloping the H II region. Along the ring-like structure, multiple YSO were detected (Figueira et al., 2017). The massive shell then fragmented into clumps, and in these clumps, cores formed that gravitationally collapsed into stars. This is the well-known 'collect & collapse' scenario of Elmegreen and Lada (1977). It suggests that compression of the surrounding medium by stellar winds can lead to triggered star formation.

The fast expansion of the bubbles indicates a young age of about $\sim 0.15\,\mathrm{Myr}$, which suggests that the new generation of star formation occurred in much shorter time scales than the free-fall time.

These observations were followed by further detections of expanding [C II] shells in some of the FEEDBACK sources, including several expanding bubbles, such as RCW 49 (Tiwari et al., 2021) and NGC 7538 (Beuther et al., 2022), and expansion

features in the bipolar H II region RCW 36 (Bonne et al., 2022), all resulting in complex geometries. These findings indicate that stellar wind-driven bubbles from massive O-type or Wolf Rayet stars might be a common feature. The expanding shells are so far only detected in [C II] emission since no counterparts of these expanding shells were observed in molecular lines or atomic hydrogen.

There are good arguments for why the expanding [C II] shells are driven by stellar winds. The energy terms of the different physical processes showed that the thermal energy of the H II region is lower than the one from the hot X-ray plasma and cannot balance the kinetic energy of the [C II] shells. In addition, the shell velocities are often (but not always) larger than the sound speed in the H II region, which is typically $\sim$10 km s^{-1}. However, the relative importance of radiation and winds is not settled and is vividly discussed among modelers (Lancaster et al., 2021a,b; Pittard et al., 2021; Pittard, 2022; Ebagezio et al., 2022). A more detailed comparison between observations and simulations is needed, but also more observational studies of stellar wind properties. In particular, a precise estimation of the mass loss rates of O- and B-stars using K-band spectroscopy (Martins et al., 2010) is required. Another point that needs further investigation is if stars only form after the fragmentation of the compressed shell or if a pre-existing clumpy cloud structure supports new star formation. Simulations of Walch et al. (2012) showed that the most likely scenario is one in which both processes take place. The clump distribution can be explained by an inhomogeneous, fractal initial cloud structure in which the cores collapse by radiation-driven implosion. However, the models consider that the impact of stellar winds is negligible.

6.2 The ISM hidden behind self-absorption

Velocity-resolved observations of spectral lines give us access to the gas kinematics of the ISM. However, optical depth effects, such as absorption by colder foreground material, do not only result in a lower observed intensity but also modify the line shape. Thus, as shown in Fig. 4.3, the absorption dip at the line peak is indistinguishable from two Gaussian components, as one would observe in an expanding bubble. To disentangle optical depth effects from gas kinematics, it is possible to compare the spectral line with the emission from a less abounded isotope. This is a common approach for the CO molecule where the primary isotope ^{12}CO is often found to be optically thick. In the case of [C II] emission, PDR models predicted the line to be optically thin, and this was assumed in most of the earlier studies of [C II] emission (Stacey et al., 1991a; Meixner et al., 1992). First - but very limited - observations of the [^{13}C II] line by Stacey et al. (1991b) showed indications that the [C II] line could be optically thick. But only the high spectral resolution observations with Herschel/HIFI (Ossenkopf et al., 2013) and later with SOFIA/upGREAT (Guevara et al., 2020) clearly revealed that the [C II] shows substantial optical depth effects.

Similar to the findings by Guevara et al. (2020) for various other sources, we find strong optical depth effects in [C II] along the PDR in RCW 120, see section 5.2.1. The results from the two-layer multicomponent model fit required large hydrogen column densities of $\sim 10^{21}\,\mathrm{cm}^{-2}$ in a cold absorbing layer. To determine the possible origin of this cold absorbing layer, we quantified the amount of cold absorbing hydrogen surrounding RCW 120, see section 5.2.3. The HISA analysis results in a similarly high column density for hydrogen temperatures between 60 K and 90 K. Combining both results, thus assuming that the cold absorbing ionized carbon layer has the same origin as the cold atomic hydrogen cloud, results in a hydrogen density between $\sim 100 - 500\,\mathrm{cm}^3$ and an extent of $\sim 5 - 10\,\mathrm{pc}$. This fits well with the observed size of RCW 120. Thus, it is likely that a substantial amount of the cold absorbing C^+ is located in the cold atomic hydrogen halo ionized potentially by cosmic rays and some leaking UV-emission. The existence of such hydrogen envelopes is well known (Burton et al., 1978; Williams and Maddalena, 1996; Lee et al., 2012; Motte et al., 2014; Imara and Burkhart, 2016; Wang et al., 2020). However, their detection is only possible if there is a substantial amount of cold atomic material surrounding the molecular cloud producing a high opacity $\tau_{\mathrm{H\,I}} > 1$ (Jackson et al., 2002) in front of a sufficiently bright background.

The existence of large column densities of cold [C II] associated with molecular clouds in the foreground (and most likely also in the background) is settled, and Kabanovic et al. (2022) propose that the [C II] originates in a rather homogeneous, low-density atomic layer, it is not clear how carbon is ionized in this gas component. The H I envelope in RCW 120 can be as large as 10 pc so that the FUV field is highly attenuated and is not the main source of ionizing carbon. More likely are cosmic rays (Girichidis et al., 2020; Gaches et al., 2022), i.e., high-energy protons from shocks associated with supernova remnants. Very energetic photons from X-rays, which are produced when the fast stellar wind of OB stars shocks the surrounding medium, can also serve as an excitation source, but they are also strongly diluted with distance from the star(s).

Fig. 6.1 shows ring-like structures wherever the stellar wind or radiation compressed the surrounding material. These ring-like features are usually interpreted as 3D bubbles, which, projected onto the plane of the sky, are visible as 2D rings. This view was challenged by Beaumont and Williams (2010), who observed 43 H II bubbles and found an emission deficit toward the center. This deficit indicates that the parental molecular clouds are flat along the line of sight. Thus, the observed dense rings are compressed to a torus instead of a spherical shell. If the cloud is flat perpendicular to the line of sight (the sheet viewed edge-on), it will look like a filamentary structure as suggested for the Musca filament by Tritsis and Tassis (2018).

CO observations of RCW 120 revealed a lack of material toward the center of the cloud. This is similar to the findings of Beaumont and Williams (2010). They proposed that the missing emission toward the center can be explained by a flat parental

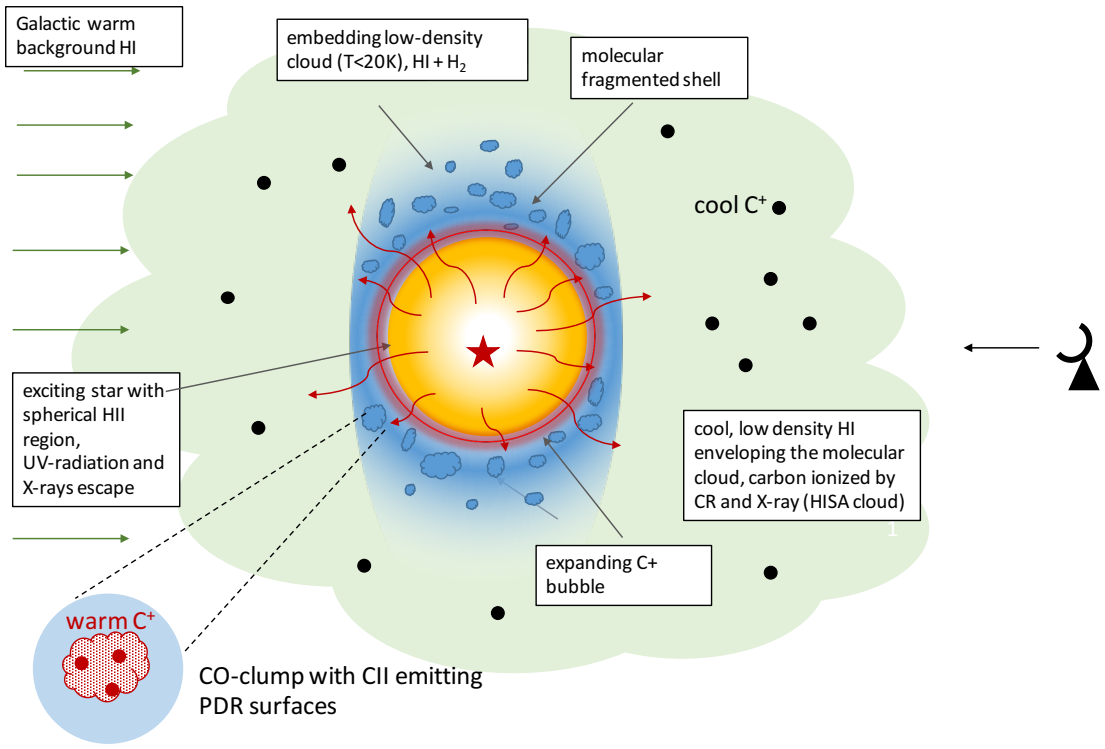

Figure 6.2: Schematic representation of the RCW 120 region to visualize the oblate geometry of the molecular cloud covered by a cold hydrogen cloud. The viewing perspective is perpendicular to the line of sight to the observer. The expanding [C II] shell (red) breaks out of the flat parental molecular cloud (blue), which is embedded in a cold hydrogen envelope (green). The observed CO (3→2) emission arises from the interior of the fragmenting torus, while the [C II] emission originates from the UV-illuminated torus surface and the expanding C^+ shell. The surrounding hydrogen cloud is the HISA gas, where the cold absorbing C^+ originates due to cosmic ray ionization. This image is adapted from Kabanovic et al. (2022).

molecular cloud. However, in the case of RCW 120 we observed a strong self-absorption effect, especially toward the center of the region, which aligns with the dark lanes, observed in absorption in Hα, spanning diagonally along RCW 120. Therefore, we performed the two-layer multicomponent model fit for the entire CO spectral data cube to disentangle the warm-emitting background from the cold-absorbing foreground. The spatial distribution of the cold foreground showed an increase of cold material toward the center of the bubble. But the column number density located in the foreground was not substantial enough to account for the observed missing emission. Thus, to explain the CO intensity distribution in RCW 120, the parental molecular cloud has to be flat. This is supported by the distribution of YSO objects only found along the

ring but not toward the region's center.

Now we need to bring the spherical expanding H II region, observed in [C II], with the flat molecular cloud, observed in CO, into one consistent picture. A schematic representation of the geometry of RCW 120 is shown in Fig. 6.2. The fast-expanding shell compresses the surrounding molecular material. The stellar wind-driven bubble continues its expansion even after breaking out of the flat parental molecular cloud in contrast to a thermal pressure-driven bubble. The swept-up material of the parental molecular cloud is compressed into a torus which is visible as a ring-like structure to the observer. Likely, most of the material emitted in [C II] from the ring originates from the surface of the compressed torus.

It is important to note that the observation might be biased toward bubbles emerging from sheet-like structures because of the enhanced contrast of the emission originating from the compressed torus and the interior, which lacks material. Bubbles fully embedded into the molecular cloud might be more difficult to detect due to optical depth effects, which might obscure the spherical geometry. In addition, the geometry of the bubble can be distorted by the surrounding magnetic field. Thus, the magnetic pressure will act against the expansion perpendicular to the field lines, while parallel to the field, the bubble can expand more freely, which would result in a rather elongated shape of the H II region (Krumholz et al., 2007).

6.3 The [C II] line as a tracer for the assembly of molecular clouds

The [C II] line is an ideal tracer of gas kinematics, and thus, we were able to observe the assembly of molecular clouds through streams of atomic gas. The interaction of these flows is observed as a velocity bridge connecting the three regions DR21, W75N, and HV, which are separated in velocity space. We find strong [C II] emission along all three velocity ranges, while the molecular emission is weak toward the high-velocity range. Thus, only $\sim$ 14% of the HV and $\sim$ 23% of the W75N gas is molecular (Schneider et al., 2023). This is in good agreement with the colliding H I flow scenario commonly used in simulations (Clark et al., 2019).

What is particularly important is the fast formation time scale of the clouds. The time scale for cloud assembly is given by the relative velocity of the different components and their size. The calculated hydrogen column densities of the W75N and the HV cloud (from HISA or from the [C II] observations) translate into a size of 12 pc for a density of 100 cm^{-3}. This leads to an assembly time of 1.3 Myr, based on their separation in velocity space by about 10 km s^{-1}. Such a fast cloud assembly is only possible in a dynamic cloud formation scenario, for example, with colliding H I flow simulations that temporarily create pockets of gas with higher density (Clark et al., 2012).

In a quasi-static scenario, molecular cloud formation would take much longer, about 10 Myr at a density of 100 cm^{-3}, based on the formation rate of molecular H_2 of 3×10^{-17} cm^3 s^{-1} (Jura, 1974).

Summarizing, this unique [C II] data set of Cygnus X is a textbook example of molecular cloud formation and, for the first time, provides strong support for a fast and dynamic cloud formation scenario.

Our findings suggest that the formation and growth of molecular clouds originate from the interaction of mostly atomic flows. After the molecular cloud is formed, parts of the atomic cold gas remain as a cold hydrogen cloud enveloping the molecular cloud, as observed in RCW 120. These atomic hydrogen envelopes can carry a substantial amount of mass. Because of the cold temperatures found in these atomic clouds, their emissivity is weak and, therefore, they are difficult to detect. However, the cold-absorbing nature of the cold atomic envelopes imprints itself through self-absorption effects on the emission from the warm emitting gas. Solving the radiation transfer equation for two layers, we are able to disentangle the warm emitting gas from the cold absorbing layer. This method only gives us access to the cold gas between the observed and the emitting source. However, it is likely that a similar amount of cold material is also located behind the observed source. With this in mind, we can use the absorption effect observed in [C II] and H I to quantify the cold atomic gas envelopes.

Appendix

A.1 Two-layer multicomponent fit parameters

A.1.1 [C II] two-layer model fit parameters

Tables A.1 to A.8 give the resulting fitting parameters of the two-layer multicomponent model fit for the [C II] spectra along the ring/torus in RCW 120. We sort the results by the areas identified with Dendograms, which are basically the brightest PDR regions of the ring. The tables are ordered by region and give the values for the background and foreground velocity components for the foreground [C II] excitation temperatures 15 K and 30 K.

Table A.1: [C II] two-layer multicomponent fit results of the RCW 120 PDR with $T_{\mathrm{ex,fg}} = 15\,\mathrm{K}$

Components	$\tau_{0,[\mathrm{C\,II}]}$	T_{ex} [K]	v_0 [km/s]	w [km/s]
Background Component 1	2.3	50.0	-7.6	3.9
Background Component 2	0.08	50.0	-14.8	9.4
Background Component 3	0.5	50.0	-7.3	7.6
Foreground Component 1	0.7	15.0	-8.9	5.0

Table A.2: [C II] two-layer multicomponent fit results of the southwestern PDR with $T_{\mathrm{ex,fg}} = 15\,\mathrm{K}$

Components	$\tau_{0,[\mathrm{C\,II}]}$	T_{ex} [K]	v_0 [km/s]	w [km/s]
Background Component 1	1.4	70.0	-8.0	5.2
Background Component 2	1.4	70.0	-7.5	2.2
Background Component 3	0.2	70.0	-12.9	10.0
Foreground Component 1	0.3	15.0	-8.1	2.2
Foreground Component 2	0.8	15.0	-11.4	3.0

Table A.3: [C II] two-layer multicomponent fit results of the southeastern PDR with $T_{\mathrm{ex,fg}} = 15\,\mathrm{K}$

Components	$\tau_{0,[\mathrm{C\,II}]}$	T_{ex} [K]	v_0 [km/s]	w [km/s]
Background Component 1	3.0	60.0	-6.9	3.8
Background Component 2	0.8	60.0	-7.1	8.1
Foreground Component 1	0.6	15.0	-7.6	3.8

Table A.4: [C II] two-layer multicomponent fit results of the northeastern PDR with $T_{\mathrm{ex,fg}} = 15\,\mathrm{K}$

Components	$\tau_{0,[\mathrm{C\,II}]}$	T_{ex} [K]	v_0 [km/s]	w [km/s]
Background Component 1	2.0	50.0	-7.3	3.6
Background Component 2	1.1	50.0	-6.9	1.2
Background Component 3	0.05	50.0	-18.6	5.6
Background Component 4	0.3	50.0	-8.4	9.4
Foreground Component 1	0.5	15.0	-9.3	2.2
Foreground Component 2	0.4	15.0	-7.3	1.8

Table A.5: [C II] two-layer multicomponent fit results of the RCW 120 PDR with $T_{\mathrm{ex,fg}} = 30\,\mathrm{K}$

Components	$\tau_{0,[\mathrm{C\,II}]}$	T_{ex} [K]	v_0 [km/s]	w [km/s]
Background Component 1	2.3	50.0	-7.6	3.8
Background Component 2	0.1	50.0	-13.8	9.9
Background Component 3	0.3	50.0	-5.7	6.2
Foreground Component 1	1.2	30.0	-9.3	5.1

Table A.6: [C II] two-layer multicomponent fit results of the southwestern PDR with $T_{\mathrm{ex,fg}} = 30\,\mathrm{K}$

Components	$\tau_{0,[\mathrm{C\,II}]}$	T_{ex} [K]	v_0 [km/s]	w [km/s]
Background Component 1	1.4	70.0	-8.0	5.2
Background Component 2	1.4	70.0	-7.4	2.2
Background Component 3	0.2	70.0	-12.9	10.0
Foreground Component 1	0.4	30.0	-8.1	2.3
Foreground Component 2	1.4	30.0	-11.8	3.1

Table A.7: [C II] two-layer multicomponent fit results of the southeastern PDR with $T_{\mathrm{ex,fg}} = 30\,\mathrm{K}$

Components	$\tau_{0,[\mathrm{C\,II}]}$	T_{ex} [K]	v_0 [km/s]	w [km/s]
Background Component 1	2.7	60.0	-6.9	3.8
Background Component 2	0.8	60.0	-7.1	8.1
Foreground Component 1	0.9	30.0	-7.6	3.6

Table A.8: [C II] two-layer multicomponent fit results of the northeastern PDR with $T_{\mathrm{ex,fg}} = 30\,\mathrm{K}$

Components	$\tau_{0,[\mathrm{C\,II}]}$	T_{ex} [K]	v_0 [km/s]	w [km/s]
Background Component 1	2.0	50.0	-7.3	3.6
Background Component 2	1.1	50.0	-6.9	1.1
Background Component 3	0.05	50.0	-18.5	5.7
Background Component 4	0.3	50.0	-8.4	9.3
Foreground Component 1	0.5	30.0	-7.3	1.7
Foreground Component 2	1.1	30.0	-9.6	2.7

A.1.2 CO two-layer model fit parameters

Tables A.9 to A.13 give the fitting results of the two-layer multicomponent model fit for ^{12}CO average spectra. The tables are ordered by the clusters identified with the GMM method and give the values for the background and foreground velocity components for the CO excitation temperatures 40 K for the background and 6 K for the foreground.

Table A.9: CO two-layer multicomponent fit results of Cluster 1

Components	$\tau_{0,\mathrm{CO}}$	T_{ex} [K]	v_0 [km/s]	w [km/s]
Background Component 1	6.9	40.0	-7.6	2.1
Background Component 2	2.2	40.0	-8.0	4.2
Background Component 3	0.006	40.0	0.6	3.8
Background Component 4	0.002	40.0	-18.8	4.2
Foreground Component 1	1.7	6.0	-5.4	4.9
Foreground Component 2	1.3	6.0	-11.0	4.7
Foreground Component 3	0.3	6.0	-8.5	2.4

Table A.10: CO two-layer multicomponent fit results of Cluster 2

Components	$\tau_{0,\mathrm{CO}}$	T_{ex} [K]	v_0 [km/s]	w [km/s]
Background Component 1	13.9	40.0	-7.0	1.6
Background Component 2	7.4	40.0	-7.2	3.1
Background Component 3	2.5	40.0	-7.9	4.7
Background Component 4	0.01	40.0	0.9	4.9
Background Component 5	0.005	40.0	-18.5	4.9
Foreground Component 1	1.7	6.0	-3.8	4.2
Foreground Component 2	1.4	6.0	-11.3	4.9
Foreground Component 3	0.7	6.0	-8.0	2.2

Table A.11: CO two-layer multicomponent fit results of Cluster 3

Components	$\tau_{0,\mathrm{CO}}$	T_{ex} [K]	v_0 [km/s]	w [km/s]
Background Component 1	2.8	40.0	-7.9	3.3
Background Component 2	1.4	40.0	-7.1	1.9
Background Component 3	0.2	40.0	-11.7	1.7
Background Component 4	0.003	40.0	0.2	2.7
Foreground Component 1	1.9	6.0	-8.7	4.9
Foreground Component 2	1.4	6.0	-12.4	2.0
Foreground Component 3	1.4	6.0	-5.0	3.3

Table A.12: CO two-layer multicomponent fit results of Cluster 4

Components	$\tau_{0,\mathrm{CO}}$	T_{ex} [K]	v_0 [km/s]	w [km/s]
Background Component 1	1.0	40.0	-7.4	2.6
Background Component 2	0.8	40.0	-9.4	2.9
Background Component 3	0.003	40.0	0.07	3.9
Foreground Component 1	1.6	6.0	-6.6	4.5
Foreground Component 2	1.4	6.0	-10.5	4.4
Foreground Component 3	1.2	6.0	-5.1	1.1

Table A.13: CO two-layer multicomponent fit results of Cluster 5

Components	$\tau_{0,\mathrm{CO}}$	T_{ex} [K]	v_0 [km/s]	w [km/s]
Background Component 1	9.3	40.0	-6.6	2.3
Background Component 2	1.3	40.0	-9.0	2.9
Background Component 3	1.0	40.0	-4.4	1.8
Background Component 4	0.2	40.0	-11.6	1.9
Background Component 5	0.01	40.0	-0.3	4.9
Foreground Component 1	1.7	6.0	-3.7	3.4
Foreground Component 2	1.7	6.0	-7.9	3.4
Foreground Component 3	1.5	6.0	-11.8	3.7

Bibliography

Barinovs, Ğ., van Hemert, M. C., Krems, R., and Dalgarno, A. (2005). Fine-Structure Excitation of C^+ and Si^+ by Atomic Hydrogen. *ApJ*, 620(1):537–541.

Beaumont, C. N. and Williams, J. P. (2010). Molecular Rings Around Interstellar Bubbles and the Thickness of Star-Forming Clouds. *ApJ*, 709(2):791–800.

Beuther, H., Schneider, N., Simon, R., Suri, S., Ossenkopf-Okada, V., Kabanovic, S., Röllig, M., Guevara, C., Tielens, A. G. G. M., Sandell, G., Buchbender, C., Ricken, O., and Güsten, R. (2022). FEEDBACK from the NGC 7538 H II region. *A&A*, 659:A77.

Bisbas, T. G., Tanaka, K. E. I., Tan, J. C., Wu, B., and Nakamura, F. (2017). GMC Collisions as Triggers of Star Formation. V. Observational Signatures. *ApJ*, 850(1):23.

Boesgaard, A. M. and Steigman, G. (1985). Big Bang nucleosynthesis: theories and observations. *ARA&A*, 23:319–378.

Bohlin, R. C., Savage, B. D., and Drake, J. F. (1978). A survey of interstellar H I from Lalpha absorption measurements. II. *ApJ*, 224:132–142.

Bonne, L., Schneider, N., Bontemps, S., Clarke, S. D., Gusdorf, A., Lehmann, A., Steinke, M., Csengeri, T., Kabanovic, S., Simon, R., Buchbender, C., and Güsten, R. (2020). Dense gas formation in the Musca filament due to the dissipation of a supersonic converging flow. *A&A*, 641:A17.

Bonne, L., Schneider, N., García, P., Bij, A., Broos, P., Fissel, L., Guesten, R., Jackson, J., Simon, R., Townsley, L., Zavagno, A., Aladro, R., Buchbender, C., Guevara, C., Higgins, R., Jacob, A. M., Kabanovic, S., Karim, R., Soam, A., Stutzki, J., Tiwari, M., Wyrowski, F., and Tielens, A. G. G. M. (2022). The SOFIA FEEDBACK Legacy Survey Dynamics and Mass Ejection in the Bipolar H II Region RCW 36. *ApJ*, 935(2):171.

Bonnell, I. A. and Bate, M. R. (2006). Star formation through gravitational collapse and competitive accretion. *MNRAS*, 370(1):488–494.

Brunton, S. L. and Kutz, J. N. (2019). *Data-Driven Science and Engineering: Machine Learning, Dynamical Systems, and Control*. Cambridge University Press.

Burton, W. B., Liszt, H. S., and Baker, P. L. (1978). Atomic hydrogen in galactic molecular clouds. *ApJ*, 219:L67–L72.

Cantat-Gaudin, T., Jordi, C., Vallenari, A., Bragaglia, A., Balaguer-Núñez, L., Soubiran, C., Bossini, D., Moitinho, A., Castro-Ginard, A., Krone-Martins, A., Casamiquela, L., Sordo, R., and Carrera, R. (2018). A Gaia DR2 view of the open cluster population in the Milky Way. *A&A*, 618:A93.

Chibueze, J. O., Omodaka, T., Handa, T., Imai, H., Kurayama, T., Nagayama, T., Sunada, K., Nakano, M., Hirota, T., and Honma, M. (2014). Astrometry and Spatio-kinematics of H_2O Masers in the Massive Star-forming Region NGC 6334I(North) with VERA. *ApJ*, 784(2):114.

Clark, P. C., Glover, S. C. O., Klessen, R. S., and Bonnell, I. A. (2012). How long does it take to form a molecular cloud? *MNRAS*, 424(4):2599–2613.

Clark, P. C., Glover, S. C. O., Ragan, S. E., and Duarte-Cabral, A. (2019). Tracing the formation of molecular clouds via [C II], [C I], and CO emission. *MNRAS*, 486(4):4622–4637.

Deharveng, L., Zavagno, A., Schuller, F., Caplan, J., Pomarès, M., and De Breuck, C. (2009). Star formation around RCW 120, the perfect bubble. *A&A*, 496(1):177–190.

Dempster, A. P., Laird, N. M., and Rubin, D. B. (1977). Maximum likelihood from incomplete data via the em algorithm. *Journal of the Royal Statistical Society: Series B (Methodological)*, 39(1):1–22.

Dicke, R. H. (1946). The Measurement of Thermal Radiation at Microwave Frequencies. *Review of Scientific Instruments*, 17(7):268–275.

Dobbs, C. L., Liow, K. Y., and Rieder, S. (2020). The formation of young massive clusters by colliding flows. *MNRAS*, 496(1):L1–L5.

Draine, B. T. (1978). Photoelectric heating of interstellar gas. *ApJS*, 36:595–619.

Duran, C. A., Gusten, R., Risacher, C., Gorlitz, A., Klein, B., Reyes, N., Ricken, O., Wunsch, H.-J., Graf, U. U., Jacobs, K., Honingh, C. E., Stutzki, J., de Lange, G., Delorme, Y., Krieg, J.-M., and Lis, D. C. (2021). 4GREAT—A Four-Color Receiver for High-Resolution Airborne Terahertz Spectroscopy. *IEEE Transactions on Terahertz Science and Technology*, 11(2):194–204.

Ebagezio, S., Seifried, D., Walch, S., Nürnberger, P. C., Rathjen, T. E., and Naab, T. (2022). CO and [CII] line emission of molecular clouds – the impact of stellar feedback and non-equilibrium chemistry. *arXiv e-prints*, page arXiv:2206.06393.

Elmegreen, B. G. and Lada, C. J. (1977). Sequential formation of subgroups in OB associations. *ApJ*, 214:725–741.

Figueira, M., Zavagno, A., Bronfman, L., Russeil, D., Finger, R., and Schuller, F. (2020). APEX CO observations towards the photodissociation region of RCW 120. *A&A*, 639:A93.

Figueira, M., Zavagno, A., Deharveng, L., Russeil, D., Anderson, L. D., Men'shchikov, A., Schneider, N., Hill, T., Motte, F., Mège, P., LeLeu, G., Roussel, H., Bernard, J. P., Traficante, A., Paradis, D., Tigé, J., André, P., Bontemps, S., and Abergel, A. (2017). Star formation towards the Galactic H II region RCW 120. Herschel observations of compact sources. *A&A*, 600:A93.

Fukui, Y., Habe, A., Inoue, T., Enokiya, R., and Tachihara, K. (2021). Cloud-cloud collisions and triggered star formation. *PASJ*, 73:S1–S34.

Gaches, B. A. L., Bialy, S., Bisbas, T. G., Padovani, M., Seifried, D., and Walch, S. (2022). Cosmic-ray-induced H_2 line emission. Astrochemical modeling and implications for JWST observations. *A&A*, 664:A150.

Geen, S., Hennebelle, P., Tremblin, P., and Rosdahl, J. (2016). Feedback in Clouds II: UV photoionization and the first supernova in a massive cloud. *MNRAS*, 463(3):3129–3142.

Girichidis, P., Pfrommer, C., Hanasz, M., and Naab, T. (2020). Spectrally resolved cosmic ray hydrodynamics - I. Spectral scheme. *MNRAS*, 491(1):993–1007.

Glassgold, A. E., Galli, D., and Padovani, M. (2012). Cosmic-Ray and X-Ray Heating of Interstellar Clouds and Protoplanetary Disks. *ApJ*, 756(2):157.

Goicoechea, J. R., Pabst, C. H. M., Kabanovic, S., Santa-Maria, M. G., Marcelino, N., Tielens, A. G. G. M., Hacar, A., Berné, O., Buchbender, C., Cuadrado, S., Higgins, R., Kramer, C., Stutzki, J., Suri, S., Teyssier, D., and Wolfire, M. (2020). Molecular globules in the Veil bubble of Orion. IRAM 30 m ^{12}CO, ^{13}CO, and C^{18}O (2-1) expanded maps of Orion A. *A&A*, 639:A1.

Goldsmith, P. F., Langer, W. D., Pineda, J. L., and Velusamy, T. (2012). Collisional Excitation of the [C II] Fine Structure Transition in Interstellar Clouds. *ApJS*, 203(1):13.

Gordy, W. and Cook, R. L. (1984). *Microwave Molecular Spectra*. New York: Interscience Pub.

Gravity Collaboration, Abuter, R., Amorim, A., Bauböck, M., Berger, J. P., Bonnet, H., Brand ner, W., Clénet, Y., Coudé Du Foresto, V., de Zeeuw, P. T., Dexter, J., Duvert, G., Eckart, A., Eisenhauer, F., Förster Schreiber, N. M., Garcia, P., Gao, F., Gendron, E., Genzel, R., Gerhard, O., Gillessen, S., Habibi, M., Haubois, X., Henning, T., Hippler, S., Horrobin, M., Jiménez-Rosales, A., Jocou, L., Kervella, P., Lacour, S., Lapeyrère, V., Le Bouquin, J. B., Léna, P., Ott, T., Paumard, T., Perraut, K., Perrin, G., Pfuhl, O., Rabien, S., Rodriguez Coira, G., Rousset, G., Scheithauer, S., Sternberg, A., Straub, O., Straubmeier, C., Sturm, E., Tacconi, L. J., Vincent, F., von Fellenberg, S., Waisberg, I., Widmann, F., Wieprecht, E., Wiezorrek, E., Woillez, J., and Yazici, S. (2019). A geometric distance measurement to the Galactic center black hole with 0.3% uncertainty. *A&A*, 625:L10.

Grenier, I. A., Casandjian, J.-M., and Terrier, R. (2005). Unveiling Extensive Clouds of Dark Gas in the Solar Neighborhood. *Science*, 307(5713):1292–1295.

Guesten, R., Camara, I., Hartogh, P., Huebers, H.-W., Graf, U. U., Jacobs, K., Kasemann, C., Roeser, H.-P., Schieder, R. T., Schnieder, G., Sievertz, O., Stutzki, J., Villanueva, G., Wagner, A., van der Wal, P., and Wunsch, A. (2003). GREAT: The German Receiver for Astronomy at Terahertz Frequencies. In Melugin, R. K. and Roeser, H.-P., editors, *Airborne Telescope Systems II*, volume 4857 of *Society of Photo-Optical Instrumentation Engineers (SPIE) Conference Series*, pages 56–61.

Guevara, C., Stutzki, J., Ossenkopf-Okada, V., Simon, R., Pérez-Beaupuits, J. P., Beuther, H., Bihr, S., Higgins, R., Graf, U., and Güsten, R. (2020). [C II] 158 μm self-absorption and optical depth effects. *A&A*, 636:A16.

Habing, H. J. (1968). The interstellar radiation density between 912 A and 2400 A. *Bull. Astron. Inst. Netherlands*, 19:421.

Haid, S., Walch, S., Seifried, D., Wünsch, R., Dinnbier, F., and Naab, T. (2018). The relative impact of photoionizing radiation and stellar winds on different environments. *MNRAS*, 478(4):4799–4815.

Haworth, T. J., Tasker, E. J., Fukui, Y., Torii, K., Dale, J. E., Shima, K., Takahira, K., Habe, A., and Hasegawa, K. (2015). Isolating signatures of major cloud-cloud collisions using position-velocity diagrams. *MNRAS*, 450(1):10–20.

Higgins, R., Kabanovic, S., Pabst, C., Teyssier, D., Goicoechea, J. R., Berne, O., Chambers, E., Wolfire, M., Suri, S. T., Buchbender, C., Okada, Y., Mertens, M., Parikka, A., Aladro, R., Richter, H., Güsten, R., Stutzki, J., and Tielens, A. G. G. M.

(2021). Observation and calibration strategies for large-scale multi-beam velocity-resolved mapping of the [CII] emission in the Orion molecular cloud. *A&A*, 652:A77.

Imara, N. and Burkhart, B. (2016). The H I Probability Distribution Function and the Atomic-to-molecular Transition in Molecular Clouds. *ApJ*, 829(2):102.

Indriolo, N., Neufeld, D. A., Gerin, M., Schilke, P., Benz, A. O., Winkel, B., Menten, K. M., Chambers, E. T., Black, J. H., Bruderer, S., Falgarone, E., Godard, B., Goicoechea, J. R., Gupta, H., Lis, D. C., Ossenkopf, V., Persson, C. M., Sonnentrucker, P., van der Tak, F. F. S., van Dishoeck, E. F., Wolfire, M. G., and Wyrowski, F. (2015). Herschel Survey of Galactic OH^+, H_2O^+, and H_3O^+: Probing the Molecular Hydrogen Fraction and Cosmic-Ray Ionization Rate. *ApJ*, 800(1):40.

Jackson, J. M., Bania, T. M., Simon, R., Kolpak, M., Clemens, D. P., and Heyer, M. (2002). H I Self-Absorption and the Kinematic Distance Ambiguity: The Case of the Molecular Cloud GRSMC 45.6+0.3. *ApJ*, 566(2):L81–L84.

Jones, D. C., Holt, H. J., Meijers, A. J. S., and Shuckburgh, E. (2019). Unsupervised Clustering of Southern Ocean Argo Float Temperature Profiles. *Journal of Geophysical Research (Oceans)*, 124(1):390–402.

Jura, M. (1974). Formation and destruction rates of interstellar H_2. *ApJ*, 191:375–379.

Kabanovic, S., Schneider, N., Ossenkopf-Okada, V., Falasca, F., Güsten, R., Stutzki, J., Simon, R., Buchbender, C., Anderson, L., Bonne, L., Guevara, C., Higgins, R., Koribalski, B., Luisi, M., Mertens, M., Okada, Y., Röllig, M., Seifried, D., Tiwari, M., Wyrowski, F., Zavagno, A., and Tielens, A. G. G. M. (2022). Self-absorption in [C II], ^{12}CO, and H I in RCW120. Building up a geometrical and physical model of the region. *A&A*, 659:A36.

Kim, J.-G., Kim, W.-T., and Ostriker, E. C. (2018). Modeling UV Radiation Feedback from Massive Stars. II. Dispersal of Star-forming Giant Molecular Clouds by Photoionization and Radiation Pressure. *ApJ*, 859(1):68.

Krumholz, M. R. and McKee, C. F. (2005). A General Theory of Turbulence-regulated Star Formation, from Spirals to Ultraluminous Infrared Galaxies. *ApJ*, 630(1):250–268.

Krumholz, M. R., Stone, J. M., and Gardiner, T. A. (2007). Magnetohydrodynamic Evolution of H II Regions in Molecular Clouds: Simulation Methodology, Tests, and Uniform Media. *ApJ*, 671(1):518–535.

Kuhn, M. A., Hillenbrand, L. A., Sills, A., Feigelson, E. D., and Getman, K. V. (2019). Kinematics in Young Star Clusters and Associations with Gaia DR2. *ApJ*, 870(1):32.

Kutner, M. L. and Ulich, B. L. (1981). Recommendations for calibration of millimeter-wavelength spectral line data. *ApJ*, 250:341–348.

Lancaster, L., Ostriker, E. C., Kim, J.-G., and Kim, C.-G. (2021a). Efficiently Cooled Stellar Wind Bubbles in Turbulent Clouds. I. Fractal Theory and Application to Star-forming Clouds. *ApJ*, 914(2):89.

Lancaster, L., Ostriker, E. C., Kim, J.-G., and Kim, C.-G. (2021b). Efficiently Cooled Stellar Wind Bubbles in Turbulent Clouds. II. Validation of Theory with Hydrodynamic Simulations. *ApJ*, 914(2):90.

Lee, M.-Y., Stanimirović, S., Douglas, K. A., Knee, L. B. G., Di Francesco, J., Gibson, S. J., Begum, A., Grcevich, J., Heiles, C., Korpela, E. J., Leroy, A. K., Peek, J. E. G., Pingel, N. M., Putman, M. E., and Saul, D. (2012). A High-resolution Study of the H I-H_2 Transition across the Perseus Molecular Cloud. *ApJ*, 748(2):75.

Luisi, M., Anderson, L. D., Schneider, N., Simon, R., Kabanovic, S., Güsten, R., Zavagno, A., Broos, P. S., Buchbender, C., Guevara, C., Jacobs, K., Justen, M., Klein, B., Linville, D., Röllig, M., Russeil, D., Stutzki, J., Tiwari, M., Townsley, L. K., and Tielens, A. G. G. M. (2021). Stellar feedback and triggered star formation in the prototypical bubble RCW 120. *Science Advances*, 7(15):eabe9511.

Madden, S. C., Cormier, D., Hony, S., Lebouteiller, V., Abel, N., Galametz, M., De Looze, I., Chevance, M., Polles, F. L., Lee, M. Y., Galliano, F., Lambert-Huyghe, A., Hu, D., and Ramambason, L. (2020). Tracing the total molecular gas in galaxies: [CII] and the CO-dark gas. *A&A*, 643:A141.

Mangum, J. G. and Shirley, Y. L. (2015). How to Calculate Molecular Column Density. *PASP*, 127(949):266.

Martins, F., Pomarès, M., Deharveng, L., Zavagno, A., and Bouret, J. C. (2010). Near-IR integral field spectroscopy of ionizing stars and young stellar objects on the borders of H II regions. *A&A*, 510:A32.

Massi, F., Weiss, A., Elia, D., Csengeri, T., Schisano, E., Giannini, T., Hill, T., Lorenzetti, D., Menten, K., Olmi, L., Schuller, F., Strafella, F., De Luca, M., Motte, F., and Wyrowski, F. (2019). Dense cores and star formation in the giant molecular cloud Vela C⋆ ⋆ ⋆. *A&A*, 628:A110.

Matzner, C. D. (2002). On the Role of Massive Stars in the Support and Destruction of Giant Molecular Clouds. *ApJ*, 566(1):302–314.

McKee, C. F. and Ostriker, E. C. (2007). Theory of Star Formation. *ARA&A*, 45(1):565–687.

Meixner, M., Haas, M. R., Tielens, A. G. G. M., Erickson, E. F., and Werner, M. (1992). Far-Infrared Observations of M17SW: The Clumpy Structure of the Photodissociation Region. *ApJ*, 390:499.

Menten, K. M., Reid, M. J., Forbrich, J., and Brunthaler, A. (2007). The distance to the Orion Nebula. *A&A*, 474(2):515–520.

Milam, S. N., Savage, C., Brewster, M. A., Ziurys, L. M., and Wyckoff, S. (2005). The $^{12}C/^{13}C$ Isotope Gradient Derived from Millimeter Transitions of CN: The Case for Galactic Chemical Evolution. *ApJ*, 634(2):1126–1132.

Moscadelli, L., Reid, M. J., Menten, K. M., Brunthaler, A., Zheng, X. W., and Xu, Y. (2009). Trigonometric Parallaxes of Massive Star-Forming Regions. II. Cep A and NGC 7538. *ApJ*, 693(1):406–412.

Motte, F., Nguyên Luong, Q., Schneider, N., Heitsch, F., Glover, S., Carlhoff, P., Hill, T., Bontemps, S., Schilke, P., Louvet, F., Hennemann, M., Didelon, P., and Beuther, H. (2014). The formation of the W43 complex: constraining its atomic-to-molecular transition and searching for colliding clouds. *A&A*, 571:A32.

Okada, Y., Pilleri, P., Berné, O., Ossenkopf, V., Fuente, A., Goicoechea, J. R., Joblin, C., Kramer, C., Röllig, M., Teyssier, D., and van der Tak, F. F. (2013). Probing the role of polycyclic aromatic hydrocarbons in the photoelectric heating within photodissociation regions. *A&A*, 553(2011):A2.

Ortiz-León, G. N., Dzib, S. A., Kounkel, M. A., Loinard, L., Mioduszewski, A. J., Rodríguez, L. F., Torres, R. M., Pech, G., Rivera, J. L., Hartmann, L., Boden, A. F., Evans, Neal J., I., Briceño, C., Tobin, J. J., and Galli, P. A. B. (2017). The Gould's Belt Distances Survey (GOBELINS). III. The Distance to the Serpens/Aquila Molecular Complex. *ApJ*, 834(2):143.

Ossenkopf, V., Röllig, M., Neufeld, D. A., Pilleri, P., Lis, D. C., Fuente, A., van der Tak, F. F. S., and Bergin, E. (2013). Herschel/HIFI observations of [C II] and [^{13}C II] in photon-dominated regions. *A&A*, 550:A57.

Ossenkopf, V., Trojan, C., and Stutzki, J. (2001). Massive core parameters from spatially unresolved multi-line observations. *A&A*, 378:608–626.

Pabst, C., Higgins, R., Goicoechea, J. R., Teyssier, D., Berne, O., Chambers, E., Wolfire, M., Suri, S. T., Guesten, R., Stutzki, J., Graf, U. U., Risacher, C., and Tielens, A. G. G. M. (2019). Disruption of the Orion molecular core 1 by wind from the massive star θ^1 Orionis C. *Nature*, 565(7741):618–621.

Pabst, C. H. M., Goicoechea, J. R., Hacar, A., Teyssier, D., Berné, O., Wolfire, M. G., Higgins, R. D., Chambers, E. T., Kabanovic, S., Güsten, R., Stutzki, J., Kramer, C., and Tielens, A. G. G. M. (2022). [C II] 158 μm line emission from Orion A. II. Photodissociation region physics. *A&A*, 658:A98.

Pabst, C. H. M., Goicoechea, J. R., Teyssier, D., Berné, O., Higgins, R. D., Chambers, E. T., Kabanovic, S., Güsten, R., Stutzki, J., and Tielens, A. G. G. M. (2020). Expanding bubbles in Orion A: [C II] observations of M 42, M 43, and NGC 1977. *A&A*, 639:A2.

Pabst, C. H. M., Hacar, A., Goicoechea, J. R., Teyssier, D., Berné, O., Wolfire, M. G., Higgins, R. D., Chambers, E. T., Kabanovic, S., Güsten, R., Stutzki, J., Kramer, C., and Tielens, A. G. G. M. (2021). [C II] 158 μm line emission from Orion A I. A template for extragalactic studies? *A&A*, 651:A111.

Palmeirim, P., André, P., Kirk, J., Ward-Thompson, D., Arzoumanian, D., Könyves, V., Didelon, P., Schneider, N., Benedettini, M., Bontemps, S., Di Francesco, J., Elia, D., Griffin, M., Hennemann, M., Hill, T., Martin, P. G., Men'shchikov, A., Molinari, S., Motte, F., Nguyen Luong, Q., Nutter, D., Peretto, N., Pezzuto, S., Roy, A., Rygl, K. L. J., Spinoglio, L., and White, G. L. (2013). Herschel view of the Taurus B211/3 filament and striations: evidence of filamentary growth? *A&A*, 550:A38.

Pineda, J. E., Arzoumanian, D., André, P., Friesen, R. K., Zavagno, A., Clarke, S. D., Inoue, T., Chen, C.-Y., Lee, Y.-N., Soler, J. D., and Kuffmeier, M. (2022). From Bubbles and Filaments to Cores and Disks: Gas Gathering and Growth of Structure Leading to the Formation of Stellar Systems. *arXiv e-prints*, page arXiv:2205.03935.

Pittard, J. M. (2022). Momentum and energy injection by a wind-blown bubble into an inhomogeneous interstellar medium. *MNRAS*, 515(2):1815–1829.

Pittard, J. M., Wareing, C. J., and Kupilas, M. M. (2021). How to inflate a wind-blown bubble. *MNRAS*, 508(2):1768–1776.

Pound, M. W. and Wolfire, M. G. (2023). The PhotoDissociation Region Toolbox: Software and Models for Astrophysical Analysis. *AJ*, 165(1):25.

Reipurth, B. and Schneider, N. (2008). Star Formation and Young Clusters in Cygnus. In Reipurth, B., editor, *Handbook of Star Forming Regions, Volume I*, volume 4, page 36.

Risacher, C., Güsten, R., Stutzki, J., Hübers, H. W., Aladro, R., Bell, A., Buchbender, C., Büchel, D., Csengeri, T., Duran, C., Graf, U. U., Higgins, R. D., Honingh, C. E., Jacobs, K., Justen, M., Klein, B., Mertens, M., Okada, Y., Parikka, A., Pütz, P., Reyes, N., Richter, H., Ricken, O., Riquelme, D., Rothbart, N., Schneider, N., Simon,

R., Wienold, M., Wiesemeyer, H., Ziebart, M., Fusco, P., Rosner, S., and Wohler, B. (2018). The upGREAT Dual Frequency Heterodyne Arrays for SOFIA. *Journal of Astronomical Instrumentation*, 7(4):1840014.

Robitaille, T., Rice, T., Beaumont, C., Ginsburg, A., MacDonald, B., and Rosolowsky, E. (2019). astrodendro: Astronomical data dendrogram creator.

Röllig, M. and Ossenkopf, V. (2013). Carbon fractionation in photo-dissociation regions. *A&A*, 550:A56.

Rosolowsky, E. W., Pineda, J. E., Kauffmann, J., and Goodman, A. A. (2008). Structural Analysis of Molecular Clouds: Dendrograms. *ApJ*, 679(2):1338–1351.

Russeil, D., Georgelin, Y. M., Amram, P., Gach, J. L., Georgelin, Y. P., and Marcelin, M. (1998). Deep Hα survey of the Milky Way. IV. The L = 301° to L = 324° area. *A&AS*, 130:119–132.

Rygl, K. L. J., Brunthaler, A., Sanna, A., Menten, K. M., Reid, M. J., van Langevelde, H. J., Honma, M., Torstensson, K. J. E., and Fujisawa, K. (2012). Parallaxes and proper motions of interstellar masers toward the Cygnus X star-forming complex. I. Membership of the Cygnus X region. *A&A*, 539:A79.

Schneider, N., Bonne, L., Bontemps, S., Kabanovic, S., Simon, R., Ossenkopf-Okada, V., Buchbender, C., Stutzki, J., Mertens, M., Ricken, O., Csengeri, T., and Tielens, A. G. G. M. (2023). Ionized carbon as a tracer of the assembly of interstellar clouds. *Nature Astronomy*.

Schneider, N., Bontemps, S., Motte, F., Blazere, A., André, P., Anderson, L. D., Arzoumanian, D., Comerón, F., Didelon, P., Di Francesco, J., Duarte-Cabral, A., Guarcello, M. G., Hennemann, M., Hill, T., Könyves, V., Marston, A., Minier, V., Rygl, K. L. J., Röllig, M., Roy, A., Spinoglio, L., Tremblin, P., White, G. J., and Wright, N. J. (2016). Globules and pillars in Cygnus X. I. Herschel far-infrared imaging of the Cygnus OB2 environment. *A&A*, 591:A40.

Schneider, N., Bontemps, S., Simon, R., Jakob, H., Motte, F., Miller, M., Kramer, C., and Stutzki, J. (2006). A new view of the Cygnus X region. KOSMA ^{13}CO 2 to 1, 3 to 2, and ^{12}CO 3 to 2 imaging. *A&A*, 458(3):855–871.

Schneider, N., Bontemps, S., Simon, R., Ossenkopf, V., Federrath, C., Klessen, R. S., Motte, F., André, P., Stutzki, J., and Brunt, C. (2011). The link between molecular cloud structure and turbulence. *A&A*, 529:A1.

Schneider, N., Ossenkopf-Okada, V., Clarke, S., Klessen, R. S., Kabanovic, S., Veltchev, T., Bontemps, S., Dib, S., Csengeri, T., Federrath, C., Di Francesco, J., Motte,

F., André, P., Arzoumanian, D., Beattie, J. R., Bonne, L., Didelon, P., Elia, D., Könyves, V., Kritsuk, A., Ladjelate, B., Myers, P., Pezzuto, S., Robitaille, J. F., Roy, A., Seifried, D., Simon, R., Soler, J., and Ward-Thompson, D. (2022). Understanding star formation in molecular clouds. IV. Column density PDFs from quiescent to massive molecular clouds. *A&A*, 666:A165.

Schneider, N., Simon, R., Guevara, C., Buchbender, C., Higgins, R. D., Okada, Y., Stutzki, J., Güsten, R., Anderson, L. D., Bally, J., Beuther, H., Bonne, L., Bontemps, S., Chambers, E., Csengeri, T., Graf, U. U., Gusdorf, A., Jacobs, K., Justen, M., Kabanovic, S., Karim, R., Luisi, M., Menten, K., Mertens, M., Mookerjea, B., Ossenkopf-Okada, V., Pabst, C., Pound, M. W., Richter, H., Reyes, N., Ricken, O., Röllig, M., Russeil, D., Sánchez-Monge, Á., Sandell, G., Tiwari, M., Wiesemeyer, H., Wolfire, M., Wyrowski, F., Zavagno, A., and Tielens, A. G. G. M. (2020). FEEDBACK: a SOFIA Legacy Program to Study Stellar Feedback in Regions of Massive Star Formation. *PASP*, 132(1016):104301.

Schwarz, G. (1978). Estimating the Dimension of a Model. *Annals of Statistics*, 6(2):461–464.

Seifried, D., Beuther, H., Walch, S., Syed, J., Soler, J. D., Girichidis, P., and Wünsch, R. (2022). On the accuracy of H I observations in molecular clouds - More cold H I than thought? *MNRAS*, 512(4):4765–4784.

Sofia, U. J., Lauroesch, J. T., Meyer, D. M., and Cartledge, S. I. B. (2004). Interstellar Carbon in Translucent Sight Lines. *ApJ*, 605(1):272–277.

Stacey, G. J., Geis, N., Genzel, R., Lugten, J. B., Poglitsch, A., Sternberg, A., and Townes, C. H. (1991a). The 158 Micron [C ii] Line: A Measure of Global Star Formation Activity in Galaxies. *ApJ*, 373:423.

Stacey, G. J., Townes, C. H., Poglitsch, A., Madden, S. C., Jackson, J. M., Herrmann, F., Genzel, R., and Geis, N. (1991b). The Optical Depth of the 158 Micron [12C ii] Line: Detection of the F = 1 0 [13C ii] Hyperfine-Structure Component. *ApJ*, 382:L37.

Sternberg, A. and Dalgarno, A. (1995). Chemistry in Dense Photon-dominated Regions. *ApJS*, 99:565.

Tielens, A. G. G. M. (2010). *The Physics and Chemistry of the Interstellar Medium*.

Tielens, A. G. G. M. and Hollenbach, D. (1985). Photodissociation regions. I. Basic model. *ApJ*, 291:722–746.

Tiwari, M., Karim, R., Pound, M. W., Wolfire, M., Jacob, A., Buchbender, C., Gsten, R., Guevara, C., Higgins, R. D., Kabanovic, S., Pabst, C., Ricken, O., Schneider, N., Simon, R., Stutzki, J., and Tielens, A. G. G. M. (2021). SOFIA FEEDBACK Survey: Exploring the Dynamics of the Stellar WindDriven Shell of RCW 49. *ApJ*, 914(2):117.

Tiwari, M., Wolfire, M., Pound, M. W., Tarantino, E., Karim, R., Bonne, L., Buchbender, C., Güsten, R., Guevara, C., Kabanovic, S., Kavak, Ü., Mertens, M., Schneider, N., Simon, R., Stutzki, J., and Tielens, A. G. G. M. (2022). SOFIA FEEDBACK Survey: PDR Diagnostics of Stellar Feedback in Different Regions of RCW 49. *AJ*, 164(4):150.

Tritsis, A. and Tassis, K. (2018). Magnetic seismology of interstellar gas clouds: Unveiling a hidden dimension. *Science*, 360(6389):635–638.

Walch, S. K., Whitworth, A. P., Bisbas, T., Wünsch, R., and Hubber, D. (2012). Dispersal of molecular clouds by ionizing radiation. *MNRAS*, 427(1):625–636.

Wang, Y., Bihr, S., Beuther, H., Rugel, M. R., Soler, J. D., Ott, J., Kainulainen, J., Schneider, N., Klessen, R. S., Glover, S. C. O., McClure-Griffiths, N. M., Goldsmith, P. F., Johnston, K. G., Menten, K. M., Ragan, S., Anderson, L. D., Urquhart, J. S., Linz, H., Roy, N., Smith, R. J., Bigiel, F., Henning, T., and Longmore, S. N. (2020). Cloud formation in the atomic and molecular phase: H I self absorption (HISA) towards a giant molecular filament. *A&A*, 634:A139.

Wendker, H. J., Higgs, L. A., and Landecker, T. L. (1991). The Cygnus X region. XVIII. A detailed investigation of radio-continuum structure on large and small scales. *A&A*, 241:551.

Williams, J. P. and Maddalena, R. J. (1996). A Large Photodissociation Region around the Cold, Unusual Cloud G216-2.5. *ApJ*, 464:247.

Wilson, T. L. (1999). Isotopes in the interstellar medium and circumstellar envelopes. *Reports on Progress in Physics*, 62(2):143–185.

Wilson, T. L. and Matteucci, F. (1992). Abundances in the interstellar medium. *A&A Rev.*, 4(1):1–33.

Wilson, T. L., Rohlfs, K., and Hüttemeister, S. (2009). *Tools of Radio Astronomy*.

Wolfire, M. G., Hollenbach, D., and McKee, C. F. (2010). The Dark Molecular Gas. *ApJ*, 716(2):1191–1207.

Wolfire, M. G., Vallini, L., and Chevance, M. (2022). Photodissociation and X-Ray Dominated Regions. *arXiv e-prints*, page arXiv:2202.05867.

Woods, P. M. and Willacy, K. (2009). Carbon Isotope Fractionation in Protoplanetary Disks. *ApJ*, 693(2):1360–1378.

Wu, Y. W., Reid, M. J., Sakai, N., Dame, T. M., Menten, K. M., Brunthaler, A., Xu, Y., Li, J. J., Ho, B., Zhang, B., Rygl, K. L. J., and Zheng, X. W. (2019). Trigonometric Parallaxes of Star-forming Regions beyond the Tangent Point of the Sagittarius Spiral Arm. *ApJ*, 874(1):94.

Yamagishi, M., Nishimura, A., Fujita, S., Takekoshi, T., Matsuo, M., Minamidani, T., Taniguchi, K., Tokuda, K., and Shimajiri, Y. (2018). Nobeyama 45 m Cygnus-X CO Survey. I. Photodissociation of Molecules Revealed by the Unbiased Large-scale CN and $C^{18}O$ Maps. *ApJS*, 235(1):9.

Zavagno, A., Pomarès, M., Deharveng, L., Hosokawa, T., Russeil, D., and Caplan, J. (2007). Triggered star formation on the borders of the Galactic H ii region RCW 120. *A&A*, 472(3):835–846.

Zhang, B., Moscadelli, L., Sato, M., Reid, M. J., Menten, K. M., Zheng, X. W., Brunthaler, A., Dame, T. M., Xu, Y., and Immer, K. (2014). The Parallax of W43: a Massive Star-forming Complex near the Galactic Bar. *ApJ*, 781(2):89.

Acknowledgments

First, I would like to thank my principal supervisor, Prof. Dr. Jürgen Stutzki, who guided me throughout my PhD. I am very grateful for all of the opportunities he has given me, especially for being part of the GREAT-team as an observer on board SOFIA. On the numerous observation flights, I had the unique opportunity to learn from his seemingly infinite knowledge of astrophysics and instrumentation. I especially learned from him to do good and precise scientific work. In addition, he always gave me sufficient freedom to pursue the questions I had in mind. Enabling me to think independently, encouraging me from the start to think about possible new exciting scientific questions and embedding them into new observational proposals.

I would like to express my very special thanks to Dr. Nicola Schneider. As one of my co-supervisors, she gave me the unique opportunity to be part of the SOFIA Legacy program: FEEDBACK. As part of the FEEDBACK program, I could work on various topics under her guidance. This way, I learned a great deal about the analysis and interpretation of various physical processes. With her extraordinary knowledge and experience, she guided me through various physical questions we addressed together, resulting in various publications written during my PhD.

Next, I would like to thank Dr. Ronan Higgins, one of my co-supervisors. At the start of my PhD, he equipped me with all the numerical tools needed for data reductions and analysis. He gave me the opportunity to be part of the C^+ Squad team, which performed the observations and analysis of the large [CII] mapping program in Orion A. Thus, through his engagement, I was part of a big international team working on an exciting scientific program right from the start. Therefore, I could not have had a better start in my PhD.

Furthermore, I would like to express my gratitude to Prof. Dr. Frank Bertoldi, a member of my graduate school thesis committee. His productive feedback on my progress during the supervision meetings was always very helpful.

I would like to use the opportunity to also thank Prof. Dr. Jan Jolie, my second thesis reviewer and examiner, and Prof. Dr. Susanne Crewell, who is the chair of my thesis defense committee. I am grateful that both agreed to be part of my final endeavor of my PhD.

In the following, I would like to extend my thanks, especially to Dr. Robert Simon.

During the many observational flights we spent together on board SOFIA he taught me everything there is to know in order to prepare and perform observations with SOFIA. His calm and helpful character even made the most stressful situations on board manageable. Thus, I always enjoyed his company and took every opportunity to learn from his great experience.

Next, I would like to thank Dr. Volker Ossenkopf-Okada. There is seemingly nothing that he does not know. Therefore, I was fortunate to have my office next to his. I used every opportunity to discuss even the seemingly most complicated topics with him. No matter the question, he always had a good answer to think about.

I would like to thank Dr. Fabrizio Falasca who has become a great friend of mine over time. I always look forward to having the next vivid discussion with him. His enthusiasm for science makes every possible topic more interesting to me. He is always full of great ideas and scientific questions I am eager to hear about. See you at Argonne Ave and 5th!

A very big thanks goes to the GREAT-team: (PIs Prof. Dr. Jürgen Stutzki and Dr. Rolf Güsten), for the many great flights we had together. I especially want to thank Dr. Christof Buchbender, who helped me a lot with his IT wisdom and always picked up the phone whenever I needed his advice, day and night. I also would like to thank Dr. Carlos Duran for all the beautiful pictures he took. Furthermore, I would like to thank Dr. Marc Mertens, who also did his PhD as part of the GREAT-team. I am happy to call him my friend since our undergraduate times and I also really enjoyed working with him on board SOFIA. In addition, I would like to thank the dream team, Dr. Urs Graf and Dr. Karl Jacobs, for sharing their enormous knowledge about instrumentation and the physics behind it.

I would like to express my gratitude to Dr. Cristian Guevara, with whom I shared my office all these years, which resulted in a flourishing scientific co-working. Together, we came up with numerous scientific ideas and submitted various observational proposals.

I also would like to thank Dr. Markus Röllig, Dr. Yoko Okada, Dr. Matthias Justen, Ignacio Barrueto, Craig Yanitski, Aleena Baby and Xiaodong Ren for all the vivid talks during the 'Kaffeeklatsch'. I always looked forward to the many scientific discussions over a cup of coffee.

I would like to thank the research group of Prof. Dr. Dominik Riechers (former Prof. Dr. Jürgen Stutzki) for the nice working atmosphere, which made me always enjoy going to work.

I was very fortunate to have so many great people accompanying me through this time. It was an amazing journey I will never forget. I would like to use this opportunity to thank all the people who are a part of my life but are not mentioned here. Thank you for all your support during my studies! Thank you for always being there for me and believing in me!

Erklärung

Hiermit versichere ich an Eides statt, dass ich die vorliegende Dissertation selbstständig und ohne die Benutzung anderer als der angegebenen Hilfsmittel und Literatur angefertigt habe. Alle Stellen, die wörtlich oder sinngemäß aus veröffentlichten und nicht veröffentlichten Werken dem Wortlaut oder dem Sinn nach entnommen wurden, sind als solche kenntlich gemacht. Ich versichere an Eides statt, dass diese Dissertation noch keiner anderen Fakultät oder Universität zur Prüfung vorgelegen hat; dass sie - abgesehen von unten angegebenen Teilpublikationen und eingebundenen Artikeln und Manuskripten - noch nicht veröffentlicht worden ist sowie, dass ich eine Veröffentlichung der Dissertation vor Abschluss der Promotion nicht ohne Genehmigung des Promotionsausschusses vornehmen werde. Die Bestimmungen dieser Ordnung sind mir bekannt. Darüber hinaus erkläre ich hiermit, dass ich die Ordnung zur Sicherung guter wissenschaftlicher Praxis und zum Umgang mit wissenschaftlichem Fehlverhalten der Universität zu Köln gelesen und sie bei der Durchführung der Dissertation zugrundeliegenden Arbeiten und der schriftlich verfassten Dissertation beachtet habe und verpflichte mich hiermit, die dort genannten Vorgaben bei allen wissenschaftlichen Tätigkeiten zu beachten und umzusetzen. Ich versichere, dass die eingereichte elektronische Fassung der eingereichten Druckfassung vollständig entspricht.

Teilpublikationen

Beuther, H., Schneider, N., Simon, R., et al. 2022, A&A, 659, A77.
Bonne, L., Schneider, N., Bontemps, S., et al. 2020, A&A, 641, A17.
Bonne, L., Schneider, N., García, P., et al. 2022, ApJ, 935, 171.
Goicoechea, J. R., Pabst, C. H. M., Kabanovic, S., et al. 2020, A&A, 639, A1.
Higgins, R., Kabanovic, S., Pabst, C., et al. 2021, A&A, 652, A77.
Kabanovic, S., Schneider, N., Ossenkopf-Okada, V., et al. 2022, A&A, 659, A36.
Luisi, M., Anderson, L. D., Schneider, N., et al. 2021, Science Advances, 7, eabe9511.
Pabst, C. H. M., Goicoechea, J. R., Hacar, A., et al. 2022, A&A, 658, A98.
Pabst, C. H. M., Goicoechea, J. R., Teyssier, D., et al. 2020, A&A, 639, A2.
Pabst, C. H. M., Hacar, A., Goicoechea, J. R., et al. 2021, A&A, 651, A111.
Schneider, N., Bonne, L., Bontemps, S., et al. 2023, Nature Astronomy.
Schneider, N., Ossenkopf-Okada, V., Clarke, S., et al. 2022, A&A, 666, A165.
Schneider, N., Simon, R., Guevara, C., et al. 2020, PASP, 132, 104301.
Tiwari, M., Karim, R., Pound, M. W., et al. 2021, ApJ, 914, 117.
Tiwari, M., Wolfire, M., Pound, M. W., et al. 2022, AJ, 164, 150.

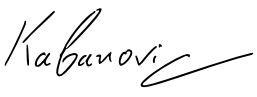

Köln, den 17.10.2023, Slawa Kabanovic